
Faculty of Electrical Engineering
Department of Radioelectronics

Doctoral thesis

# Simulation and application of advanced nanolayers and optical elements for space X-ray imaging

Ing. Veronika Stieglitz

**Ph.D Programme:**
Electrical Engineering and Information Technology (P2612)

**Specialization:**
Radioelectronics (2601V010)

**Supervisor:**
Prof. RNDr. Rene Hudec, CSc.

**Supervisor specialist:**
Ing. Ladislav Sieger, CSc.

Prague, March 2023

## ABSTRACT

This doctoral thesis describes the development, application and testing of reflective layers for X-ray optics. These layers are designed to overcome some of the limitations of state-of-the art materials, like reflectivity fluctuations at certain energies, and aim on usage on board of future space-born telescopes. Manufactured samples were subjected to a series of tests, studying various properties as well as the environmental and time stability necessary for space application.

As the result of development, a demonstrator was built to proof the capability of this new solution in comparison with classic materials.



## KEYWORDS

Multiple layers, X-ray optics, Thin Metal Layers, Materials, Chromium, Iridium, Gold



## ANOTACE

Tato doktorská práce popisuje vývoj, výrobu a testování odrazivých vrstev pro rentgenové teleskopy. Popisované vrstvy jsou navrženy tak, aby obešly některá omezení, kterým čelí materiály používané v současnosti, například pokles odrazivosti v okolí absorpčních hran. Cílem je, aby mohly být použity při stavbě budoucích kosmických teleskopů. Vrstvy byly nasimulovány, vyrobeny a následně prošly řadou testů, zkoumajících jejich vlastnosti a stabilitu v závislosti na prostředí a čase, nezbytných pro použití ve vesmíru.

Výsledkem tohoto vývoje je předváděcí optika, postavená tak, aby bylo přímým porovnáním možno zhodnotit, kterak si nové vrstvy vedou v porovnání s klasickými materiály.



## KLÍČOVÁ SLOVA

Multivrstvy, Rentgenové optiky, Tenké kovové vrstvy, Materiály, Chrom, Iridium, Zlato

## ACKNOWLEDGEMENT

I would like to thank to my colleagues, friends, and family, who were supporting me in my professional and personal life during the doctoral studies.
Namely - to Mates, a friend of mine, whose rule of 'Each normal person has a PhD.' and shared life experiences often helped me, when I wanted to give up.
My group leader Peter, whose professional experiences and personal kindness are exceptional.
Vadim, who enabled all my X-ray tests at the PANTER facility.
My husband Dirk, who kept helping me to disentangle my thoughts and patiently suffered speeches about topics of mine, although being out of his own scientific field.
My official and unofficial Doktorväter, Rene, Ladislav, Standa and Thorsten, for their lead, cooperation and having time when it was needed.
My supportive parents, especially my father, who was always happy for each small step and success of mine, encouraging, and curious about my deeds. You are the best parent I could have ever wished for.


## DECLARATION

I declare that I have written my doctoral thesis on the theme of "Simulation and application
of advanced nanolayers and optical elements for space X-ray imaging
" independently, under the guidance of the doctoral thesis supervisor and using the technical literature and other sources of information which are all quoted in the thesis and detailed in the list of literature at the end of the thesis.

As the author of the doctoral thesis I furthermore declare that, as regards the creation of this doctoral thesis, I have not infringed any copyright. In particular, I have not unlawfully encroached on anyone's personal and/or ownership rights and I am fully aware of the consequences in the case of breaking Regulation § 11 and the following of the Copyright Act No 121/2000 Sb., and of the rights related to intellectual property right and changes in some Acts (Intellectual Property Act) and formulated in later regulations, inclusive of the possible consequences resulting from the provisions of Criminal Act No 40/2009 Sb., Section 2, Head VI, Part 4.

In Prague, March 30, 2023

.....
author's signature

# Contents

# List of Acronyms

**CCD**
Charge-coupled device

**FOV**
Field of view

**FWHM**
Full-width half-maximum

**GCM**
Gold coated module

**ICM**
Iridium coated module

**lEBc**
Low energy band continuum

**mEBc**
Middle energy band continuum

**MPE**
Max Planck Institute for Extraterrestrial Physics

**PSF**
Point-spread function

**RMS**
Root mean square

**SLR**
Single lens reflex

**TEM**
Transmission electron microscopy

**UHV**
Ultra-high vacuum

**WFC**
Wide field camera

**XMA**
X-ray mirror assembly

**XUV**
Extreme ultra-violet

# 1 Introduction and motivation

Astronomical objects and phenomena are studied since the ancient times. The very first observations were performed in visible light, with the naked eye and later using telescopes with refractive or reflective optics. With scientific progress, the fact that space objects are radiating in the whole electromagnetic spectrum was discovered and the research interests moved into more exotic wavelengths. Some of these spectral ranges, for example radio waves or infrared radiation, are observable from the Earth's surface with various limitations. Other types of radiation, like X-rays and gamma rays, are absorbed by the atmosphere and for observation, space-born telescopes are needed to be build. For illustration, stratospheric balloons flying at approximately 35 km altitude can be used for observation of X-rays harder than 30 keV, sounding rockets can capture the rays beyond 3 keV. However, an altitude of at least 200 km is necessary, to capture photons with energies below 1 keV.

This work focuses on the X-ray part of the spectrum, on building X-ray optics, which could be in the future comparable and competitive with the optical systems being common currently, or suitable for filling-in the weaknesses current systems suffer from. One of these weaknesses is a small field of view, an inherent property of the most common optics type, the Wolter I [1–3]. Other improvements can be achieved by melioration of technological procedures and materials.

The wide-field optics will be represented by several different optical arrangements. Lobster eye optics, in Schmidt's arrangement or as independent modules, which is based on usage of flat mirrors adjusted into a fan-like shape. Kirkpatrick-Baez arrangement, which has a similar configuration of modules as the lobster eye, but differs in the fact that individual mirrors are not flat, but elliptically or parabolicaly curved. A hybrid design, which combines both approaches simulating the curvature effect by approximation from flat mirror segments. And the final design, a nested, multi-module optics, which combines all these optical possibilities to get the best results.

The first chapter brings a brief introduction into the current state-of-the-art of technology. First, important missions are presented together with the used technology, as well as examples of observations, with emphasis on the materials of the mirror modules in *Historical missions*. The chapter *X-ray optics* discusses different types of X-ray optics and the basic principles they are working with. In *Reflective layers*, the ways of preparation and coating of reflective optical surfaces for X-ray mirrors are introduced. During working on the topic, the importance of high quality reflective layers and the interest in new materials for both substrates and layers increased. For that reason, a large part of the work done moved from simple geometrical design of a possible small X-ray telescope towards studying of the coating layer behaviour and

understanding processes, which could improve the reflectivity of an X-ray mirror.

From this new approach, a design for a multiple-layer coating with nanometric overlays emerged, which was subsequently exposed to environmental conditions and was subject to physical investigations as well as X-ray optical tests, as described in the chapters *Reflective layers for X-ray mirrors, Manufacturing experimental samples, X-ray testing* and *TEM test*.

# 2 Past and current X-ray missions

So called "soft X-rays" from celestial sources - that can be measured with imaging optics discussed in this thesis - are less energetic when compared to the "harder" X-rays discovered by Wilhelm Conrad Röntgen that are used today for medical diagnostics. Most cosmic sources have been detected in the soft X-ray band from 0.5 keV to 5 keV [4, 5]. This radiation is already absorbed by a thin layer of atmosphere, so that it is preferably observed with space-born telescopes. In comparison, an observation from a balloon in 40 km altitude allows observations of harder X-rays. For 30 keV X-rays, e.g., the transmission is approximately 60% in vertical observing direction, but drops to 36% at 60° from vertical direction and to zero at 90° [1].

The requirements for the device depend mainly on the energy of interest. The atmospheric absorption explained above sets the lower threshold of the energy range that can still be reasonably detected as a function of altitude. Stratospheric balloon missions reaching altitudes up to 40 km are sufficient vehicles for instruments to observe sources at 30 keV and above. Sounding rockets reaching altitudes above 150 km are capable of carrying detectors for energies of 3 keV [2]. Instruments must be adapted for operation in near-vacuum environments.

In case of orbiting satellites, there is a possibility to detect very low energies, under 1 keV. These energies could be detected above 200 km as well, but the satellites have to avoid the drag of the upper atmosphere layers, which would lead to re-entry and burn. A preferred orbit is at 600 km altitude, just below the Van Allen belts, but some satellites are orbiting in highly-eccentric orbits. This allows them to spend most of the time out of Van Allen belts and also the South Atlantic Anomaly, which has to be considered. In such regions, charged particles, especially electrons, are trapped. They are not only increasing the radiation background, but can induce a damage of sensitive satellite's parts as well. For this reason, sensitive parts like the detectors are usually switched off when trespassing problematic areas [4].

[1] This corresponds almost to the horizon, while for higher altitudes the actual horizon will be lower.

[2] This was the case of the very first usage of Wolter I optics for solar observation. In 1965, an Aerobee Rocket,NAS 4.63 G S carried an electroformed nickel single shell telescope with focal length 83.6 cm and collecting area of 1.6 $cm^2$ paired with several cameras equipped with filters. Using exposure times 5 s - 99 s, the experiment returned to Earth with several X-ray images of Sun surface in X-ray and visible spectrum [6].

## 2.1 First observations

The very first carriers able to reach necessary altitudes were modified V2 rockets, remaining after the World War II [7]. These missions were purposed to observe the Sun in UV and X-ray light, because it was believed, this is the only source bright enough. Calculations showed, that if other stars were radiating comparably with the Sun, available detectors were not able to detect any signal from them.

After the first UV observations in 1946, the first X-ray detection from the Sun followed in 1948. Later, in 1962, an Aerobee rocket experiment with three Geiger X-ray counters on board. This experiment, coded as AS&E, was designed to detect X-ray reflection of solar wind particles on the Moon's surface and perhaps some fluorescence. That information was possibly valuable for getting a better idea about the character of the Lunar surface, useful for planned manned missions in the same decade (ended with landing of Apollo 11 in 1969). AS&E was launched on June 18, 1962 and during the flight, two of three detectors on board functioned well. The expected observation of X-rays from the Moon failed, but the secondary part of the mission, scanning the sky searching for possible deep-space X-ray sources, brought the detection of Scorpius X–1. This object, which was in visible spectrum observed four years later, is a close-type binary system consisting of a neutron star and a bluish hot star and it is the strongest known X-ray source except the Sun. The neutron star draws the material of its hot counterpart into its accretion disc and when this stellar matter is accelerated by the neutron stars gravity, X-rays are emitted. [8]

## 2.2 Significant missions

This chapter is a brief synopsis of several missions, which present a breakthrough in the X-ray astronomy. Basic information is given with respect to the topic of the thesis, with emphasis on the materials and coating layers of the optics and type and technology of the detectors.

Because my thesis focuses on the imaging telescopes for X-ray observations, only missions carrying this type of telescope are described (with an honourable exception of the very first X-ray satellite, Uhuru), although many other missions, approaches and technologies were and are being used for studying this spectral range.

### 2.2.1 Uhuru

The first X-ray satellite was launched in 1970 from a platform off the coast of Kenya and was orbiting in near-Earth equatorial orbit. It was carrying two proportional counters, instead of an optics it was equipped only with a honeycomb collimator. One proportional counter had a field of view 1 °, the other one 10 °. With a 12 minute period stabilised rotation, a source could be up to 2 s / 20 s in the field of view. The search for weak sources was supported by multi-time scanning, over 60 scans per a sky region. This stacking of pictures in combination with higher altitude than was reached during rocket flights enabled to detect ten times fainter objects.

The lifetime of the mission was two and a half years and 95% of the sky was mapped. Although the mission faced technical issues and the efficiency was not optimal, the compiled catalogue 4U contains 339 objects. Strong sources were located with 2' accuracy and the obtained light curves of them proved the binary system character in several cases, determining the orbital periods and spins. Faint sources were located with accuracy of several square degrees [4].

### 2.2.2 HEAO-B – EINSTEIN

HEAO-2, after successfully reaching orbit and connecting with the base station renamed to EINSTEIN, was launched in 1978 by NASA and was the first fully imaging X-ray orbital telescope [9]. It accomplished 5600 observations, examined structure of supernova remnants, of clusters of galaxies and the distribution of sources in normal galaxies. The lifetime of EINSTEIN was limited by on-board cryogenic supply to eleven months.

The satellite carried a 4-shells nested, quartz glass (fused silica) Wolter I telescope with 3.45 m focal length and on-axis resolution 4 arcsec. The mirrors were coated by nickel, grazing angles ranged from 40 arcmin to 70 arcmin and maximum observable energy was 4 keV, while the effective area at 1 keV was 100 $cm^2$. The telescope was equipped by a turntable with four different instruments, which could be placed one at the time into the focal plane of the optics.

Because the main goal of the mission was X-ray imaging, there was the High Resolution Imager (HRI) with good spatial resolution (2 arcsec), but quite poor energy resolution. On the other hand, the Imaging Proportional Counter (IPC) was able to detect the energy of each event, but its spatial resolution was 40 arcesc in the best case. The Solid State Spectrometer provided very good energy resolution, but no spatial information at all, because it was just recording all events in a 6 arcmin field of view. And finally, the fourth detector was a proportional counter, monitoring variability of bright sources.

There were also two high-resolution spectrometers housed aboard the EINSTEIN satellite. One of them was a set of golden diffraction gratings and it was possible to

insert it between the Wolter I telescope and one of the detectors listed above. The spectrometer was able to give an energy resolution of 50. Last instrument was a focal-plane crystal spectrometer, a curved Bragg spectrometer. Both of them had effective area smaller than a square centimetre, so only the brightest sources were observable. [10, 11]

### 2.2.3 EXOSAT

This mission was a result of cooperation among Germany, Italy, Great Britain and the Netherlands under the patronage of European Space Agency (ESA). It was designed as a lunar occultations observer, but by the launch time (1986) brighter sources were already well located and this type of observations was no longer needed. In the end, the major accomplishment of EXOSAT were measurements of high quality, long-duration light curves from accretion-powered sources.

This feature was an implication of highly elliptical orbit, which enabled up to 76 hours of observation for most objects. The satellite was equipped with two imaging telescopes of Wolter I type, each consisting of two nested shells. The grazing incidence angle of the telescope was relatively large, 1.8 ° for outer and 1.5 ° for the inner shell; this corresponds with low energies, up to 2 keV, the instrument was designed for. On-axis angular resolution was 5 arcsec, the focal length was limited to 1 m by the parameters of the spacecraft.

The nested shells were machined out of beryllium with microns accuracy, were 3.5 nm thick and plated by golden reflective layer. Both telescopes were equipped with two detectors on the changing mechanism and a set of filters. The position sensitive proportional counter (PSD) had a polypropylene entrance window and 4.5 nm deep absorption region filled with argon and methane mixture. Emphasis was placed on good energy resolution to permit multi-colour mapping of diffuse sources and to determine spectra, which were out of EINSTEIN's imaging proportional counter abilities.

The channel multiplier array consisted of two microchannel plates in chevron arrangement. The plates had a diameter of 50 mm, individual channels 25 µm and the front one was coated with magnesium fluoride to improve the quantum efficiency.

The detector was equipped with a filter–wheel to provide a broad-band spectroscopic capability. Because of possible UV contamination, the detector had to be used always with the filter. [12]

### 2.2.4 ASCA (ASTRO-D)

ASCA (The Advanced Satellite for Cosmology and Astrophysics) was brought up to the orbit on 20th February 1993 and was build as a result of cooperation between Japanese space agency JAXA and NASA. This satellite was the first using CCD detectors for X-ray astronomical observations. During over seven active years, orbiting between 520 and 620 km above the Earth, the satellite focused on X-ray spectroscopy

of astrophysical plasma, especially the analysis of discrete features such as emission lines and absorption edges. Due to it's energy range coverage, it was able to detect K-lines and absorption edges at various ionisation stages from oxygen to iron. Also the motion of plasma was possible to measure, using the Doppler shift of the line energies.

The telescope with 3.5 m focal length had an extendable optical bench and was unfolded in orbit. X-ray telescope consisted of four mirror modules, each of them made of 120 shells. Single shells were made of replicated aluminium foils and coated with 10 - 20 µm of acrylic and 60 nm of gold. Compared to e.g. quartz glass shells, it was not possible to polish the aluminium foils and therefore the sharpness of the image was reduced; this technology provides angular resolution in order of few arcmins. On the other hand, it enables good performance in terms of the ratio of mass to the geometric area and broad detectable energy range, accordingly is applicable for spectroscopy or polarimetry missions, where large effective area of a telescope is more important than high angular resolution.

The whole set of four mirror modules was providing effective area of 1,300 $cm^2$ with field of view 24 arcmin at 1 keV and on-axes angular resolution of 2.9 arcmin. The telescope was able to observe sources with energy up to 12 keV.

The detectors, coupled with the mirror modules, were two gas scintillation imaging proportional counters and two CCD cameras. This very first space used CCD had resolving power of 50 FWHM at 6 keV and 20 at 1.5 keV, and was able to detect energies from 0.5 keV. It's field of view was 20' x 20' [13, 14].

### 2.2.5 ROSAT

ROSAT, a German, USA and UK joint mission (1990-1999), carried out the first all-sky survey using an imaging X-ray telescope. The satellite was in a circular geocentric orbit at an altitude of 580 km.

On board of the ROSAT were two co-aligned instruments - the X-ray Mirror Assembly (XMA) as the main telescope for soft X-rays, and smaller Wide Field Camera (WFC) for the extreme UV range (XUV). XMA was a Wolter I mirror assembly, consisting of four nested mirrors. The mirrors were made of Zerodur (glass ceramics) and coated with a golden reflective layer. Grazing incidence angles were between 1° and 2°, in dependence on the diameter of the shell. Total focal length of the mirror assembly was 2.4 m, the aperture 83.5 cm, and reached an so far unprecedented angular resolution of 3".

The mirror assembly was possible to couple with a multiwire proportional counter (PSPC), which had a high spatial resolution of about 25 arcsec at 1 keV and was equipped with a boron filter, or with a high resolution imager, comprised of two cascaded microchannel plates (MCPs) with a crossed grid position readout system, which provided a 38 arcmin FOV and had about 2 arcsec FWHM. The energy range of observation laid between 0.1 and 2.4 keV.

The Wide Field Camera consisted of 3 Wolter-Schwarzschild Type I mirrors, made from nickel plated aluminium with golden reflective layer. Focusing on the much softer XUV radiation up to 0.21 keV, the reflective angle was about 7.5 ° and FOV 5 °. The received rays were filtered by 8 different types of filters to define the passing wavelength and lower the background radiation. This XUV telescope was paired with two channel plate detectors and the observable energy range laid between 0.06 and 0.2 keV.

Thanks to the main telescope's excellent imaging performance and extremely low noise level of the PSPC, ROSAT was able to discover during its lifetime over 125,000 X-ray sources, while the WFC detected 479 sources in the XUV band. It also mapped the diffuse galactic X-ray emission, with origin in the supernova remnants or clusters of galaxies, with high angular resolution - better than 1 arcmin. Based on ROSAT observations, they were spectroscopically analysed for the first time. Most of the time, the telescope was performing pointed observations of selected targets. Phenomena like supernovas, lensing clusters or neutron stars were observed. One of the most famous images is an X-ray portrait of the Moon, proving that our satellite not only reflects the X-rays from the Sun, but also emits its own soft radiation [15, 16].

### 2.2.6 XMM-Newton

ESA's largest scientific satellite ever launched was carried to orbit on 10 December 1999 by an Ariane 5 rocket. Planned mission-time of this 10 m long and approximately 4 tons heavy telescope was ten years, but due to the good health conditions of the instruments, the mission was prolonged and still runs.

XMM Newton's X-ray telescope consists of three Wolter I mirror sets. Each of them is composed of 58 mirrors, nested in confocal and coaxial configuration. The biggest shell has 70 cm diameter and the focal length is 7.5 m. With its aperture ratio of approximately f/10 and thus small grazing angles, the optics is able to image X-rays up to 10 keV - a new break through in X-ray astronomy. Each telescope is equipped with X-ray and visible light baffles, which serve as suppressive elements of the stray-radiation, and an electron deflector. The deflector creates a circumferential magnetic field and prevents low energy electrons to reach the detector. The focal planes are equipped with two different types of cameras: one pn-CCD camera and two MOS-CCD cameras. Two of the telescopes are equipped with reflecting gratings, which disperse about half of the incident radiation onto a CCD strip at secondary focus to bring spectroscopic information. This makes about 40% of incoming energy while the remaining 44% falls on CCD camera at prime focus, while the rest of light is absorbed in the grating array's support structure. [17]

The mirrors were made from nickel using the electroforming method. Thickness of the mirrors linearly rises from 0.47 mm for the innermost shell to 1.07 mm for the largest mirror to provide satisfactory stiffness of the shells. The coating material is 100 nm thick layer of gold. [11]

### 2.2.7 Chandra

The telescope with the best resolution so far was brought up to high eccentric orbit in 1999. The position enabled up to 160 ks observations and useful scanning for 70% of time, with a few days gap caused by the solar activity per year. With its 0.5" resolution but relative small collecting area, Chandra is the ideal complement to XMM-Newton in the 0.5-10 keV range. Combination of sensitive detectors, high resolution and collecting area of 1500 square centimetres made it possible to study even faint sources in dense fields. To the most important observations belong the first seen emission of a supermassive black hole (Sagittarius A*), first images of a supernova shock wave, evidence of dark matter existence by observing a cluster collision, or cannibalisation between two galaxies.

Originally, Chandra spacecraft should carry a 6–shell Wolter I telescope, but due to a budget cut, the number has been reduced to four shells. They are machined of 2 cm thick quartz glass and coated by 33 nm layer of iridium. The grazing angle ranges from 27' to 51' and the focal length is 10 m. The telescope can focus rays with energy up to 10 keV and its on-axis angular resolution is 0.5 arcsec [18].

One of two different detectors can be placed in the focal plane at a time. The Advanced CCD Imaging Spectrometer (ACIS) which includes 10 CCD detectors - four forming the imaging array with 16' to 16' field of view, six in a line serving for spectroscopy. In energy range, it can catch photons 0.2–10 keV. High Resolution Camera (HRC) compounds of two micro-channel plates and images over the range of 0.07–10 keV with time resolution of 16 µs.

The detectors can also be combined with diffraction gratings to get a spectral image. The High Energy Transmission Grating Spectrometer (HETGS) ranges from 0.4 keV to 10 keV and has a spectral resolution of 60–1000 nm. The Low Energy Transmission Grating Spectrometer (LETGS) ranges between 0.09 keV and 3 keV and has a resolution of 40–2000 nm. These combinations of telescope and gratings are sensitive enough to get high-resolution spectra from many types of moderately strong X-ray sources.

### 2.2.8 eROSITA

The eROSITA telescope, aboard the Russian-German Spektr-RG space observatory, was brought to orbit in 2019. The telescope is able to observe X-ray sources in the 0.2-10 keV range. The mission planning foresees a 4 year long all-sky survey, followed by pointed observations. The spacecraft, orbiting around the L2 Lagrangian point of Sun/Earth is spinning with a period of 4 hours and such creates an all-sky map every half a year.

eROSITA X-ray optics consists of seven identical Wolter I mirror modules. Their optical axes are co-aligned, ensuring an identical field of view of all seven telescopes, with focal length of 1.6 m. Each mirror module consists of 54 nested shells. For each

shell, a super-polished aluminium mandrel with a surface layer of nickel alloy was prepared. A reflective golden layer of 100 nm thickness was evaporated on the surface of the mandrel, copying from its surface the required optical quality.

The mirror shell substrate is - like XMM-Newton - from electroformed nickel with wall thicknesses from 0.2 to 0.54 mm from inner to outer shells, while their grazing angles are between 20' and 93'.

Each of the optical modules is focusing on its own camera. Cameras are the next generation of pn-CCD cameras used at XMM-Newton telescope. The pixel size was reduced to 75 µm to adapt to eROSITA's resolution. Second important change is, the CCD array was extended for a frame store area. This enables fast shift from the image area to reduce the out-of-time events, photons which are recorded and lost during the charge-transfer. The pn-CCDs have 384×384 pixels, which means an image area of 28.8mm×28.8mm, for a field of view of 61" diameter. [19, 20]

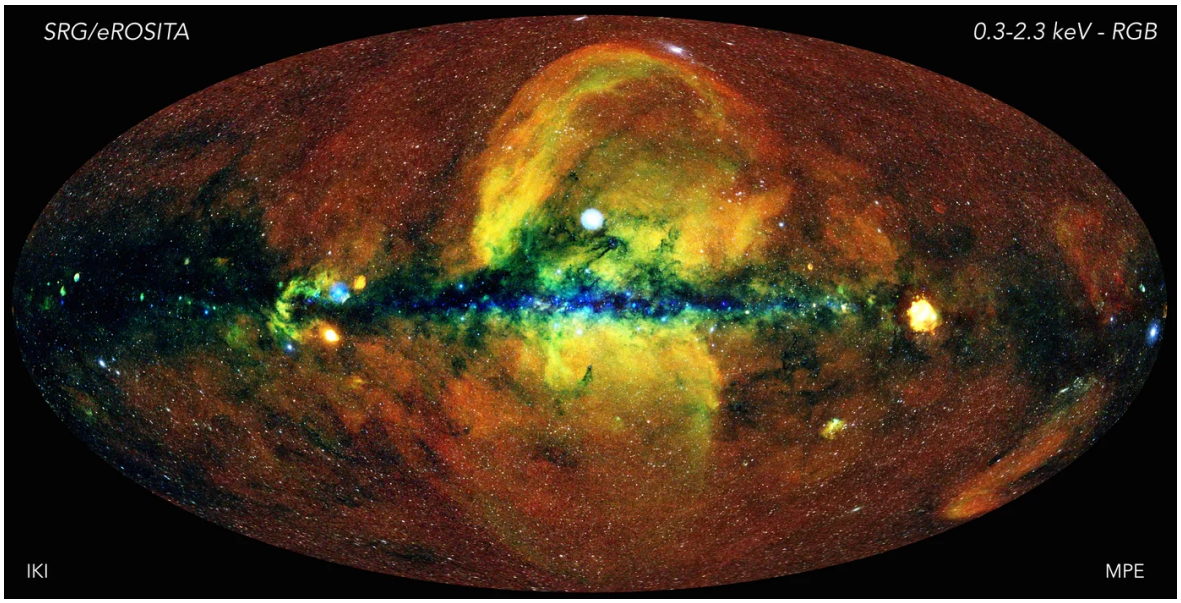


**Fig.** 2.1: To generate this image, in which the whole sky is projected onto an ellipse (so-called Aitoff projection) with the centre of the Milky Way in the middle and the body of the Galaxy running horizontally, photons have been colour-coded according to their energy (red for energies 0.3-0.6 keV, green for 0.6-1 keV, blue for 1-2.3 keV). The original image, with a resolution of about 10", and a corresponding dynamic range of more than one billion, is then smoothed (with a 10' FWHM Gaussian) in order to generate the above picture. Credit: Jeremy Sanders, Hermann Brunner and the eSASS team (MPE); Eugene Churazov, Marat Gilfanov (on behalf of IKI).

# 3 X-ray optics

This chapter presents the X-ray optics of Wolter, Kirkpatrick-Baez and lobster eye types. All designs have in common that grazing angles have to be small (of the order of 1 degree or less) - the higher the photon energy, the smaller the angle - to allow for total reflection, as in detail described in Chapter 4.1.2. Because every reflection causes energy losses, the optics are designed to work with only one reflection per mirror. From design point of view [1], this is enforced by using the correct ratios between the lengths and height of the optical channels. Occurring multiple reflections are attenuated in the material and reflected out of the focus.

A detailed analysis for the incidence angle and energy dependence of the reflectivity for X-rays is presented in chapter 4. The following sections consider the geometry of different optical designs.

## 3.1 Wolter optics

In 1952, Hans Wolter described how an X-ray telescope could be built using rotationally symmetric grazing incidence mirrors [1]. Invented optics in its essential arrangement uses two reflections at two circular-in-cut, hollow mirrors, which have different longitudinal shape. According to this shape, we distinguish three types of Wolter optics, Wolter I, II and III. The description of all types and imaging principle follows.

### 3.1.1 Types of Wolter optics

The three variants of Wolter optics are depicted in Fig. 3.1. They are all based on two reflections, which focus incoming rays into a point, fulfilling Abbe's sine condition. All three designs have advantages and disadvantages. The imaging performance of Wolter optics is perfect only on the optical axis, while it degrades inevitably towards larger off-axis angles, quantitatively depending on the optical design parameters. Angular resolution of Wolter optics is in general given for the on-axis imaging.

Wolter I optics consists of a primary parabolic and a secondary hyperbolic mirror. The hyperboloid cone angle is usually three times the paraboloid, so that the on-axis X-rays have the same incident angle on both mirrors. The ray impacts on the paraboloid section, is reflected, undergoes the second reflection on the hyperboloid mirror and then the image is formed in the hyperboloid focus. This design creates a good image on the optical axis, but when the source moves to the edge of the field of view, starts to suffer

[1] Most relevant for the lobster eye type of optics.

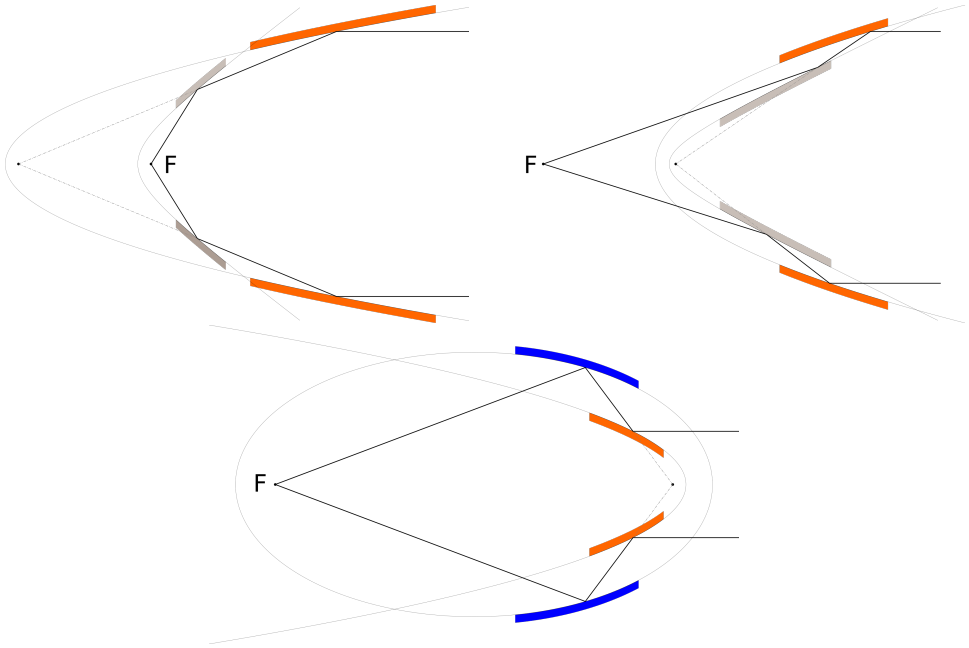


**Fig.** 3.1: Schematics of three types of Wolter optics. Upper left - Wolter I, upper right - Wolter II, bottom - Wolter III. A reflection at both surfaces and the focal point F are displayed, the mirrors are a cut of several possible shapes: paraboloid (orange), hyperboloid (gray) and ellipsoid (blue).

on coma and spherical aberration. To eliminate this effect, Wolter I variations use two non-confocal, coaxial hyperboloid planes, but in that case, the on-axis image quality is reduced [21].

The Wolter II design also uses paraboloid primary and hyperboloid secondary mirror, but in this case, the outer surface of the hyperboloid is used as a reflective one. Type II enables to get longer focal lengths with comparable incidence angle but suffers even more on the aberrations. The nesting of this mirror's layout is also complicated. To increase the collecting area, more than simple nesting is increasing the incidence angle. As was already mentioned, with rising angle, the spectral range in which is the mirror usable, is reduced. For this reason, this method is ineffective for wavelengths shorter than 10 nm and makes the Wolter II telescope suitable rather for extreme to far ultraviolet observations than for focusing X-rays. Wolter II was used for example on SOHO satellite, as part of CDS (Coronal Diagnostic Spectrometer) [22].

The Wolter III type uses a paraboloid as the primary mirror as well, but its outer surface. As the secondary serves the inner surface of an ellipsoid. Both shapes are confocal again, the image appears in the ellipsoid's focus. Wolter III design has never been used for X-ray astronomy yet.

There is also the question of nesting possibilities. The effective aperture of a single Wolter mirror shell is not the surface of a circle, with the diameter of the mirror. It is a narrow intermediate ring, which corresponds to the difference between the diameter

of mirror's entrance and exit aperture. For this reason, the mirrors are co-axially nested and the effective area of the modulus rises. Large current X-ray missions (Chandra, XMM-Newton, eROSITA) are all equipped with the Wolter I telescopes. Its the only design that allows nesting of confocal mirror shells with different radii and such allowing to fill a given diameter with collecting area. The challenge of mirror shell nesting are extreme demands on the preciseness during completion of the whole module. [1,23–26]

## 3.2 Non-Wolter grazing incidence optics

In the following section, several types of non-Wolter grazing incidence optics and the basic principle of focusing in a lobster eye are presented. All these optics work analogously to Wolter optics, with a double-reflection under very small incident angles and also require high surface quality of the mirrors. As is described further, some of them have much wider field of view for the price of lower angular resolution, others are comparable with Wolter optics in the imaging quality and FOV. The concepts with flat mirrors are also much simpler to manufacture, than replicated Wolter I optics.

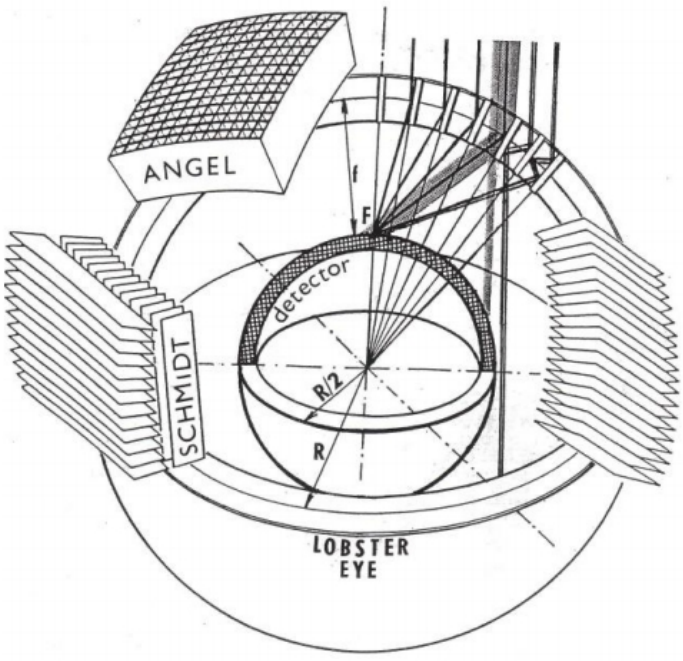


**Fig.** 3.2: Lobster eye arrangements. Schmidt's arrangement consisting of two sub-modules, a compact Angel arrangement with rectangular cells, principle of single and multiple reflection in one sub-module. Such multiple reflection will lead to strong attenuation of the incoming rays due to the losses at surface imperfections and penetration into the mirror material, as the larger grazing incident angle does not allow total reflection [27].

### 3.2.1 Principle of lobster eye optics

Figure 3.3 shows the basic setup of the lobster eye optics in one dimension, and its main features. Characteristic is the fan-like mirror arrangement, which imaginary prolongations converge in R, and the resulting focal point in F. The focal length $f$ is defined from the middle of the on-axis mirror and is related to the convergence of the mirrors as $f = r/2$. In the case of several sub-modules in a line, the effective focal length is always measured from the middle of the whole optical system. In the simplified example in Figure 3.3 is shown only one set of mirrors with reflection only on one side of mirrors, although there would be symmetry, if the rays were coming from other side. Result of this setting would be a stripe shaped focus, with width in respect to the width of single channels, marked $a$, not a true image of observed object. Such focus is later called 1D.

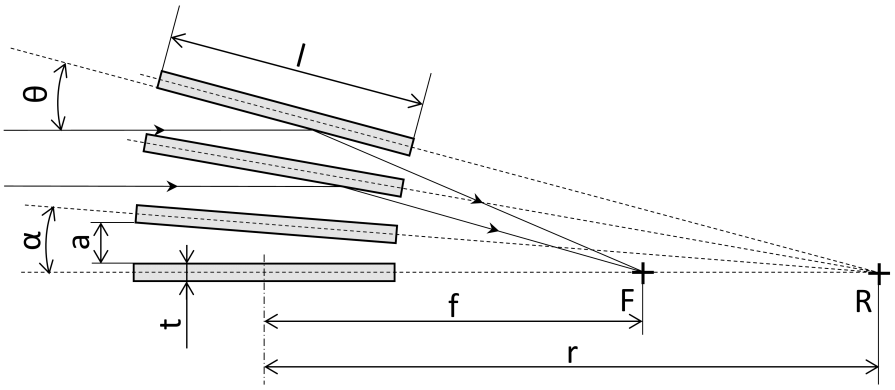


**Fig.** 3.3: Schematic arrangement of a Lobster eye optics. $t$ is the thickness of a single mirror, $a$ the distance between the mirror centres, $l$ is the length of a mirror, $\alpha$ is the angle between the centres of two neighbouring mirrors, $r = 2f$ is the average radius, $f$ is the focal length, F the focal point, R the convergence point of all the mirrors. Two parallel rays from a source placed in infinity impact and reflect on a mirror under angle $\theta$. [28]

The following equations are used to determine the angular resolution of the optical module:

$$\theta = \omega = 2\alpha = \frac{2(a+t)}{r}, \tag{3.1}$$

where $\omega$ is the angular resolution, $\alpha$ is the convergence of the mirrors, and $a, t, r$ diameters according to 3.3. The field of view (FOV) of the module derives from:

$$FOV = \frac{A_{eff}}{r}, \tag{3.2}$$

where $A_{eff}$ is the effective aperture of the optics, $r$ the curvature radius [29].

### 3.2.2 Angel optics

In 1979 J.R.P. Angel described an optics, which tries to truly imitate the eye of some crustaceans species [30]. These animals are usually living in deep, scanty illuminated waters and their eyes work on completely different principle than the mammal chamber eye. Instead of using lenses, they consist of small rectangular cells, which have reflective internal surface. The light is transmitted through the cells, undergoing two reflections and focused into a spherical surface, which is in the middle of the radius of the eye. Using two reflections, the eye produces 2D picture of the surroundings.

In the crustacean's eye, which is adapted for observing in visible light, the ratio of length and width of the square cells is lower, as described in [31–33]. For X-ray focusing, the ratio has to be much bigger, typically the length is about 100 times the width, due to the small grazing angles [30].

This system is not easy to manufacture technologically. Possible ways are to use square pore channel plates or to use a bunch of microtubes, which are squeezed to get the desired shape [34, 35].

### 3.2.3 Schmidt optics

A different type of optics, which also provides a 2D picture, is the lobster eye design in Schmidt's arrangement [36]. This kind of optics uses planar mirrors, which are arranged into the shape of a fan. X-rays, which are in the focus of this optics, were reflected one time on each mirror. The whole optics consists of two sub-modules, which are arranged perpendicularly to each other as can be seen in Fig. 3.2. The rays are coming into the aperture and are focused into a line by the first sub-module. Then, the rays undergo the second reflection, when are reflected in the perpendicular sub-module. These two subsequent reflections form a cross-shaped picture of the source. How the real images created by this kind of optics look can be seen in Fig. 3.4.

The efficiency of the optics depends on the thickness of the mirrors, on the gaps between them, as well as on the reflectivity and the quality of the mirrors surface [36]. One of the possible ways how to improve the efficiency of the lobster eye optics is to use the two sub-modules independently, with two detectors, and get a real picture in post-processing [37]. Of course, this concept requires adequately shaped and sized detector, which would be capable of detecting the whole length of 1D focus without losses.

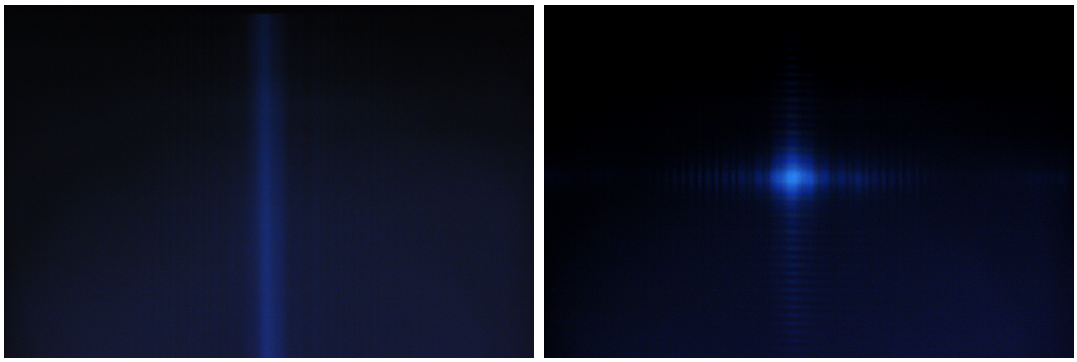

**Fig.** 3.4: Images produced by a lobster eye optics in Schmidt's arrangement. Line focus, a result of the first reflection in 1D single optical module, and a cross from two placed perpendicularly, 2D image. Images were taken using SLR camera at the Ondrejov observatory and the observed object is the bright star Vega.

### 3.2.4 Kirkpatrick-Baez optics

The third type of non-Wolter optics is the Kirkpatrick-Baez (K-B) design. Compared to the lobster eye, it has better angular resolution and smaller FOV, in these parameters is a K-B system more like the Wolter. This type basically also uses two sub-modules for focusing at first into a line and then into a spot, similarly to the lobster eye in Schmidt's arrangement. Compared to it, the mirrors of the K-B optics are not planar but curved. Schema of rays coming through the K-B optical module can be seen in Figure 3.5. The first experimental optics was completed from parabolic and elliptical mirrors [38]. Ideally, the shape of a very eccentric ellipsoid is used for the mirrors, but it can be also replaced by a spherical surface [39], due to easier manufacturing of such shape. This design however suffers from strong astigmatism [38]. Different experiments with shape and the ways how to improve it were made [40–42].

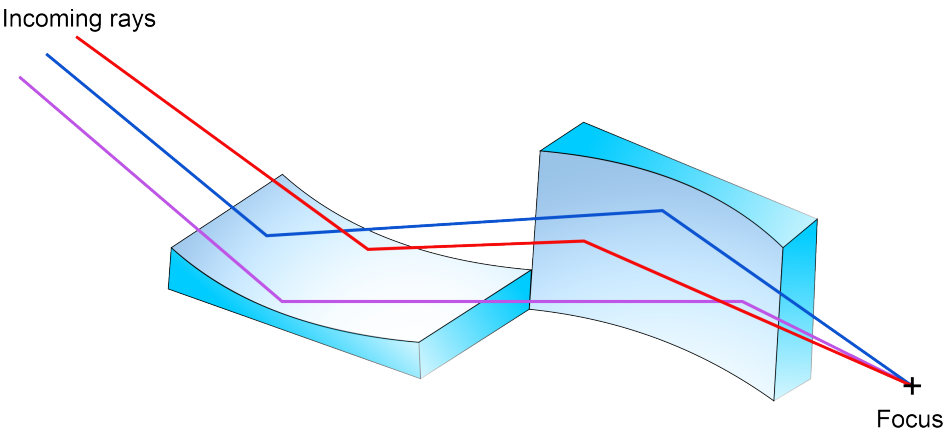


**Fig.** 3.5: Schematic of a double-reflection in a Kirkpatrick-Baez module.

### 3.2.5 Experimental optics

For tests described in this work, a hybrid optics was designed and manufactured. Its design is based on K-B optics, but while K-B uses curved mirrors, this concept borrows the flat mirrors from lobster eye optics. The basic idea is that using several flat mirrors in a row, it is possible to approximate the parabolic K-B mirror, while maintaining the simplicity of production that characterises the lobster eye.

Figure 3.7 shows a CAD image of the simplest realisation, with two segments approximating the curved surface per reflection direction. The whole optics consists of four units (mirror-stacks), creating two sub-modules. A sharp image is created by placing them one after, as shown in the CAD image, because their focal lengths by design differ by their physical length. Details about the dimensions and geometry are given in Table 3.1.

Compared to the lobster eye in Schmidt's arrangement, which is symmetric, this optic's geometric and optical axes are not the same. As the mirrors are coated only from one side, the optics can be imagined as a quarter of a full lobster eye. Geometrical axis is moved with respect to the same optical axis. That as well effectively eliminates all the direct rays which would be coming through only partially closed channels in case of classic lobster eye design.

The basic idea of this four-units module is that the mirrors are working complementary. Part of the incoming rays reflects from the first mirror in the sub-module, part from the second one, with respect to the gap between the mirrors. The path of the rays through the module is depicted in Figure 3.6. Here can be seen that the beams reflected at the first mirror do no intersect with the next unit, but reflect for the second time at first in the other sub-module, which is oriented perpendicularly, and are directed to the focus. This geometry is selecting the compatible incidence angles.

After the idea of multiple-layers coating with Cr-Ir was developed over the course of this work, planned testing module was updated to enable wider scale of experiments.

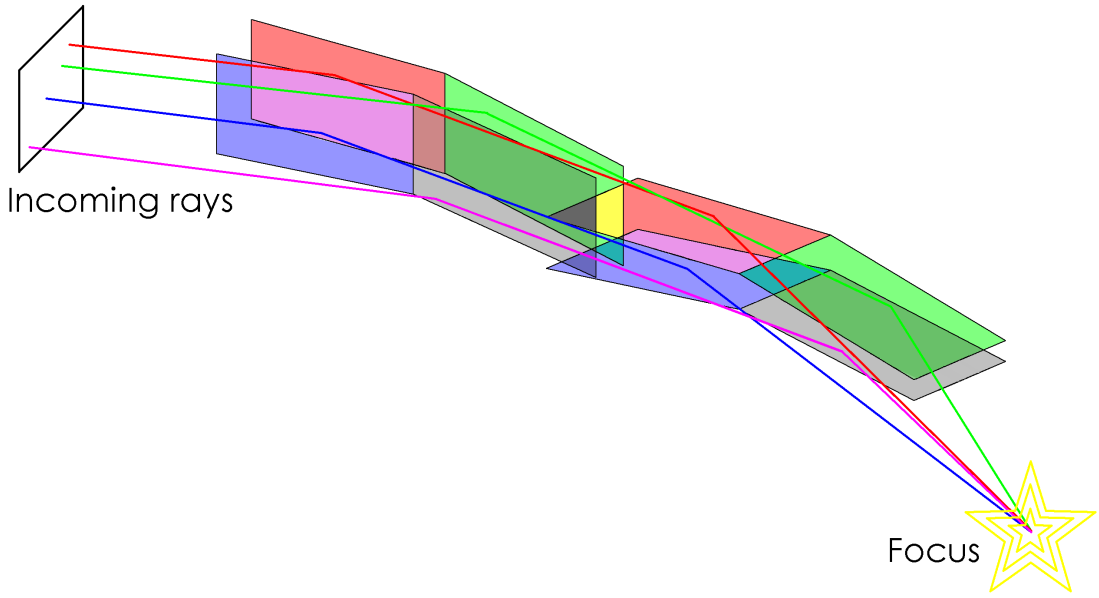


**Fig.** 3.6: Schematic of a double-reflection in hybrid lobster eye modules. For better readability, the rays and the mirrors they are reflected from are coded in the same colour.

Instead of coating all four units with one type of layer, two were coated with gold, a long-term standard coating in space born X-ray optics, and two with Cr-Ir tri-layer, as described in Chapter 4.

These four units can be arranged in various ways, with each sub-module coated with one material, and the units being in line or orthogonal:

- two sub-modules with both units oriented in the same direction placed separately; this option provides two independent 1D, line foci
- two sub-modules with both units in the same orientation, and these sub-modules oriented perpendicular to each other; this option behaves as a K-B approximation and provides one 2D, point focus
- two sub-modules with units oriented perpendicular to each other; this arrangement behaves like a lobster eye module in Schmidt's arrangement and provides two times an independent 2D, point focus
- all four units separately, providing 4 independent 1D, line foci

Due to these different organisation of the units and sub-modules, it was possible to perform comparative measurements during the measurement campaigns, evaluating the properties of the layers, as well as the behaviour of the whole, pseudo-K-B optics. The assembled optics got the name HORUS[2], and was tested in configurations HORUS I and HORUS II, as is described in Chapter 9.

[2]The name was chosen according to the ancient Egypt falcon god Horus. According to the description in legends, his golden right eye was the Sun, the silver left one to the Moon. In the testing configuration, the optics sitting next to each other will match this arrangement.

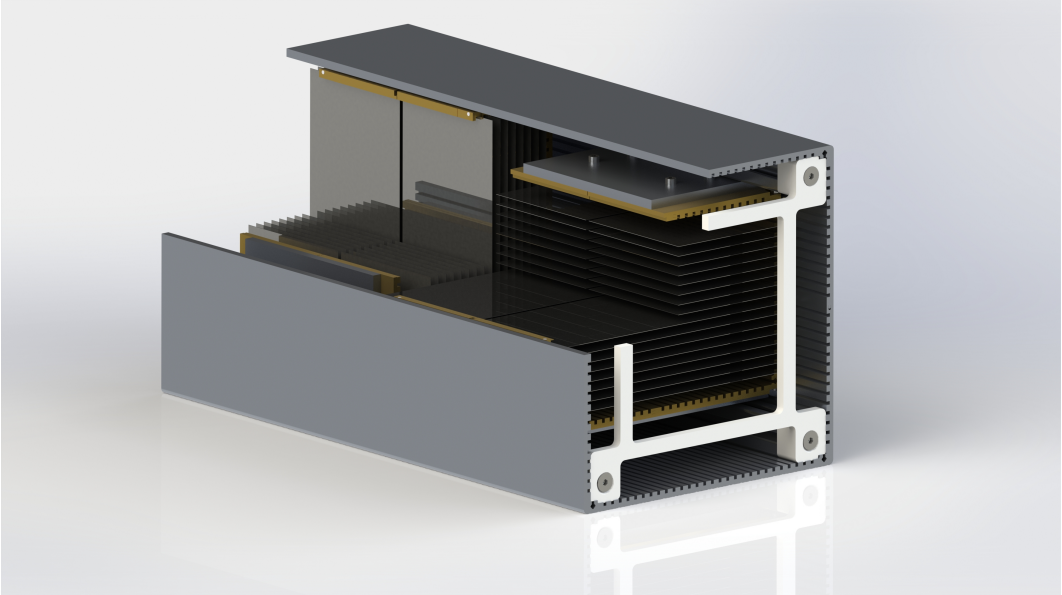

**Fig.** 3.7: 3D model of hybrid lobster eye optics.

**Tab.** 3.1: Basic properties of experimental optics HORUS

| | Au coated | Cr-Ir-Cr coated |
|---|---|---|
| Number of mirrors | 68, 17 pcs per unit | |
| Aperture | 80 mm × 80 mm | |
| Material of mirrors | silicon | |
| Number of units | 2 | 2 |
| Mirror dimension | 100 mm × 50 mm | |
| Focal length | 2.05 m | 1.95 m |
| Maximal grazing angle | 0.5° | |
| Gap between the mirrors | 4.336 mm | |
| Thickness of mirrors | 0.625 mm | |
| Coating material | Au | Cr-Ir-Cr |
| Coating thickness | 30 nm | 60/30/6 nm |
| Required microroughness | RMS < 0.5 nm | |
| Energy of observed sources | 0.1–10 keV | |

# 4 Reflective layers for X-ray mirrors

This chapter is dedicated to the theoretical background of preparation of reflective layers for X-ray mirrors and ways how to improve their properties and quality, which affect the final reflectivity in the desired energy range [43]. Coating layers used for producing X-ray reflective surfaces are usually made of heavy metals like gold and iridium and the thickness of these layers varies from tens to hundreds of nanometers [44].

The quality of the coating can be evaluated from two different points of view. The first is the qualitative rating of the coating material. Here can be assessed the reflectivity of the selected material, i.e. the effectivity of reflection in dependence on the incident angle or the reactivity with the environment during the process of layer deposition. The second examines the properties of the prepared layer. Here are evaluated features like adhesivity between the reflective layer and carrying substrate, microroughness achievable using actual deposition methods, stress in the layers, which can affect the temporal stability of coatings and others [45].

The chapter describes a theoretical study of coatings dedicated for a hybrid lobster-eye optical module design, which was described in chapter 3 and in [46–48]. The main idea was to prepare a reflective layer suitable for relatively soft X-rays, up to 8 keV, 10 keV maximum. There were two possible partner laboratories capable to produce the reflective layers for this work. One could provide the golden layer, the other one the iridium ones. Because the iridium layers show overall better performance and were at the time also the choice for upcoming large space X-ray telescopes, iridium layers were chosen to be prepared. The iridium layer's advantage over gold is about 5 % better reflectivity in the energy range from 2.2 keV to 9 keV, the positive difference is ever rising at the higher energies. A common disadvantage of such one-material layers are energetic gaps, caused by absorption edges. Namely, iridium has an energetic gap around 2 040 eV, corresponding to the electron binding energy of Fermi level M5. Here, the reflectivity of the material at the considered incident angle drops from about 90 % to about 10 % and then returns to 80 %, with not so prominent decreases at other Fermi levels (M4, M3, M2, M1; 2040.4 eV, 2116.1 eV, 2550.7 eV, 2908.7 eV, 3173.7 eV respectively). For gold, this gap occurs as well, with most prominent gap at Fermi level M3-M5, and weaker decreases at other Fermi levels (M5, M4, M3, M2, M1; 2205.7 eV, 2291.1 eV, 2743.0 eV, 3147.8 eV, 3424.9 eV respectively).

Later, experimental optics were produced, as described in Chapter 5. One was coated with described iridium layers, and a mechanically identical copy had golden coating for comparison. These two optics then served as testing pieces to confirm the theoretical expectations.

## 4.1 Reflection basics

This introduction includes an explanation of total reflection and its relation to relevant material properties, which are considered in the optic design and the simulation tools.

The benefit of total reflection is to avoid pervasion into the material, but relies on small angles, typically below 0.5 degree. As Fig. 4.1 shows, the reflectivity drops sharply at increasing angles, especially at higher energies. A high reflectivity is essential for a good efficiency in optical, especially astronomical, applications.

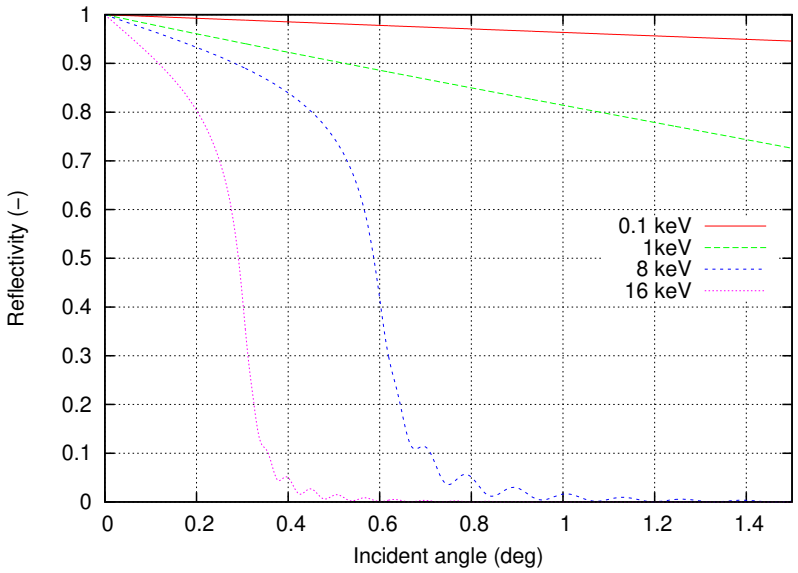


**Fig.** 4.1: Different X-rays wavelengths reflectivity dependence on incident angle. Thick iridium coating on silicon, 0.5 nm microroughness of the surface [49].

### 4.1.1 Atomic scattering factor

Each chemical element has a different atomic scattering factor, which represents how strongly X-rays interact with individual atoms. The scattering factor consists of two components. Absorptive coefficient $\beta$, which describes how strongly the material absorbs the radiation, and dispersive coefficient $\delta$, describing the non-absorptive interaction leading to refraction, are defined as

$$\beta = \frac{e^2\hbar^2}{2\epsilon_0 m_e E^2}\bar{f}_2, \tag{4.1}$$

$$\delta = \frac{e^2\hbar^2}{2\epsilon_0 m_e E^2}\bar{f}_1, \tag{4.2}$$

where $m_e$ is electron weight, $\hbar$ reduced Planck constant, $E$ the energy of incident radiation, $e$ the electron charge and $\epsilon_0$ vacuum permittivity. $\bar{f_1}$ and $\bar{f_2}$, the mean values of atomic scattering factors per unit volume and apply when it does not depend on the scattering angle (the wavelength is large compared to the typical size of bounded electron distribution in an atom), are defined as

$$\bar{f_{1(2)}} = \sum_j N_j f_{1(2)}, \tag{4.3}$$

where N is refractive index and $f_1$ scattering factor. These evaluations lead to the total reflection.

### 4.1.2 Total reflection

Total external reflection occurs at a grazing angle $\theta$ according to Snell's law:

$$cos\theta = 1 - \delta \tag{4.4}$$

or for $\delta \ll 1$:

$$\theta = \sqrt{2\delta} \tag{4.5}$$

where $\delta$ is the index of refraction or the optical constant. $\delta$ can be computed from anomalous dispersion theory. For X-ray wavelengths $\lambda$ sufficiently apart from absorption edges $\delta$ reads as follows:

$$\delta = N_0 \frac{Z r_e}{A 2\pi} \rho \lambda^2 \tag{4.6}$$

where $N_0$ is Avogadro's number, $r_e$ is the classical electron radius, Z and A are the atomic number and weight, respectively, and $\rho$ is the mass density [50].

The ratio of the absorption coefficient $u$ and the material scattering coefficient $\delta$ affect the reflectivity. The absorption coefficient, as well as the ratio, are zero at the critical angle ($\theta_c$). The reflectivity is very sharply falling after exceeding the $\theta$.

According to Snell's law, the critical condition that makes the total reflection possible is to get the incident angle smaller than the critical angle. In case that the incidence angle is larger than $\theta_c$, multiple reflections can appear in lobster eye optics. To minimise this effect, the geometric design of the optics is chosen such that the critical angle $\theta_c$ is the same as the limit angle $\beta_L$, according to equation:

$$\theta_c = \beta_L = 2\beta_{eff} = \frac{2a}{l} \tag{4.7}$$

where $\beta_L$ is the limit angle, $a$ the gap between neighbouring mirrors, and $l$ the length of single mirror. The geometric properties are according to the schematic in Figure 3.3.

Beside the minimisation of multiple reflection this condition allows to achieve the optimum ratio between the largest effective aperture $b^2$ and reflectivity at $\beta_{eff}$. Another condition which must be considered during the lobster eye design is

$$\beta_{eff} \gg \alpha = \frac{a+t}{r} \tag{4.8}$$

where the $\alpha$ angle is the mirror's convergence. All formulas are used according to [29, 50–52].

## 4.2 Simulations

All figures represent the result of simulations, prepared as a template for an integrated testing set of multiple layers coatings on silicon. They were done using an online available software solution from Berkeley laboratories, based on the research of B.L.Henke et al., [49].

Materials of the layers were chosen according to the previous tests and are reflecting the already acquired experiences. The thicknesses of each layer are chosen according to two main parameters. The first is minimal thickness, which is needed to get a fully-reflective layer avoiding energetic transmission into substrate. The second is the influence of thickness on microroughness and energy losses in the layers. Other constraints were given by the equipment available.

The sputtering machine, which has been used to produce samples for real tests, is able to work with two targets at once [53]. Thus, during changing between two materials, there is no need to open the chamber and flood it with air. Layers prepared by this procedure are thus not threatened by oxidation, which could cause material degradation and generation of indefinable interlayers. A limitation is that the chamber has only two targets, so the combinations of layers are constrained. The simulations work included the following parameters:

- materials of layers and substrates,
- roughness of the surface,
- density and thickness of the layers,
- energy of incident rays and the angle of incident.

### 4.2.1 Materials

The materials for the planned experiments are chromium and iridium, the substrate for the mirrors is a silicon wafer. Other assessed materials were gold and aluminium. The reasons of the final choice are described below.

According to previous studies, an iridium layer sputtered on super-polished silicon does not have adequate adhesivity. Because of internal stress in the layer and insufficient adhesivity between the layer and the substrate, cracks occur and peeling off of

the layers happens [43, 54, 55].

To improve the adhesivity, an interlayer prepared of suitable element can be introduced between the substrate and the reflective layer. Previously, we have tested the interlayers based on aluminium and chromium. These elements have similar crystalline structure and adhesivity tests performed according to ISO2409 standard showed that both aluminium and chromium eliminate the peeling-off issue. Chromium was chosen as the inserted element because of its environmental stability, which is generally better than of aluminium. As was mentioned above, when wanting to avoid the oxidation influence in between the coatings, only two targets can be mounted, so the chromium has to be used as the overlayer as well. At this moment, the better stability of chromium is beneficial.

### 4.2.2 Surface roughness

The parameter of surface microroughness has strong impact on the final reflectivity, because the wavelength of incident rays is similar to the mean value of microroughness, and therefore the scattering effect causes strong energy losses. To get relevant results, root mean square (RMS) roughness values measured using AFM on the samples of proper materials and thicknesses were used as the simulation input. Mean values obtained from these measurements are listed in Tab. 4.1.

The samples which were used are listed bellow:

- a pure silicon wafer with crystallographic structure (1,0,0),
- the same grade silicon wafers with a 100 nm thick layer of chromium,
- a 30 nm thick layer of iridium,
- a 30 nm thick layer of gold.

For sputtered layers, the microroughness of the surface rises with layer thickness. Because of that, is was important to measure the samples with actual production thickness, as is listed above.

**Tab.** 4.1: Table of different sputtered layers microroughnesses.

| Surface type | RMS (nm) |
|---|---|
| Silicon substrate | 0.17 |
| Chromium | 0.35 |
| Iridium | 0.50 |
| Gold | 0.38 |

### 4.2.3 Layer thickness

The optimal thickness of the layers depends on the factor of ideally zero transmission into the substrate for the reflective iridium layer and of stress compensation in the

chromium-iridium bi-layer. The stresses in iridium and chromium layers are inverse and to achieve the lowest possible stress level, the thickness ratio Cr:Ir is 3:1 [56].

There is the question of the chromium overlayer thickness as well. The iridium layer is the main reflective surface and should be opaque for the X-rays in the whole considered energy range. Contrary to that, the overlayer, which has a better reflectivity at lower energies, should be transparent for the higher ones, to not unnecessarily limit the reflection at the main layer. According to the sputtering abilities of the machine, the thinnest layer with sufficient homogeneity in all the points is 4 nm. Aiming for thinner layers showed that the islands of material with gaps in between them tend to form.

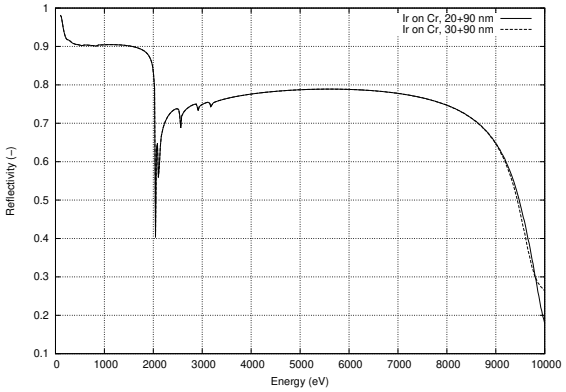


**Fig.** 4.2: Influence of different iridium reflective layer thickness. Chosen 20 and 30 nm.

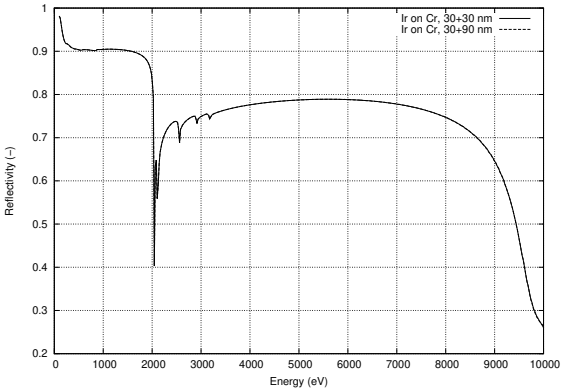


**Fig.** 4.3: Influence of different chromium adhesive layer (90 or 30 nm) on reflective properties of 30 nm thick iridium surface.

### 4.2.4 Limits of the simulation

As a relevant reflectivity limit was chosen 50 %. Even with improved optical design, which allows to focus more rays into the focal point, the ray still undergoes two reflections and that doubles the energy loss. Since the potential targets for observation are generally weak, lesser reflectivity was considered as not worth it.

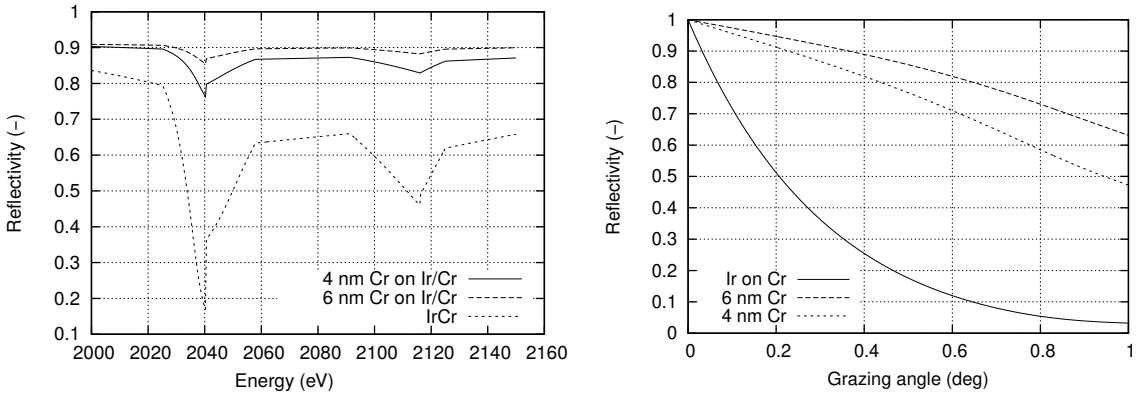


**Fig.** 4.4: Detail of the energy gap at 2040 eV, where the improvement caused by usage of chromium overlayer is clearly visible (left figure); The dependence of reflectivity on the incident angle for the critical M5 energy. Angle values range from 0 to 1 deg, the layer is 4 or 6 nm thick chromium on 30 nm of iridium (right figure).

### 4.2.5 Simulations results and discussion

The simulations were performed for a series of combinations of thicknesses of adhesive layer, main reflective layer and an overlayer. The first task is to compare the influence of different thicknesses on the absolute reflectivity of the main reflecting layer. The comparison of 20 nm, 30 nm, 40 nm and 50 nm layers of iridium showed only marginal changes (<1%) in reflectivity at energies over 9 keV. In figure 4.2 is a comparison of chosen values of thickness, 20 and 30 nm.

Also the thickness of the adhesive layer was changed to ensure the reflectivity will not be affected by it. As expected, if the simulation shows that the iridium layer behaves like an opaque one, the underlayer thickness does not have anymore effects on the reflectivity in case of chromium-iridium bilayer (chosen two examples again, figure 4.3). The real risk of changing the thickness of adhesive layer is based more on possible rising microroughness, which can then project into the main layer, with thicker layers.

As already mentioned in the beginning of this chapter, there was a possibility to choose between golden and iridium layer for the main reflective surface. The comparison of reflectivity is in Fig 4.5, where are shown iridium and golden layers of the same thickness (30 nm) and on the same chromium underlayer (70 nm). The reflectivity of iridium is from 3% to 25% better in almost the whole range with an exception of the energy gap at 2 040 eV. The region with reflectivity better than 50 % goes actually even 1 keV further towards high energies.

The application of a chromium overlayer is illustrated in Fig. 4.4. There is a detail of the energy gap around M5 for two different overcoating thicknesses and for two conditions; energy change in close surroundings (left figure) and an influence of the

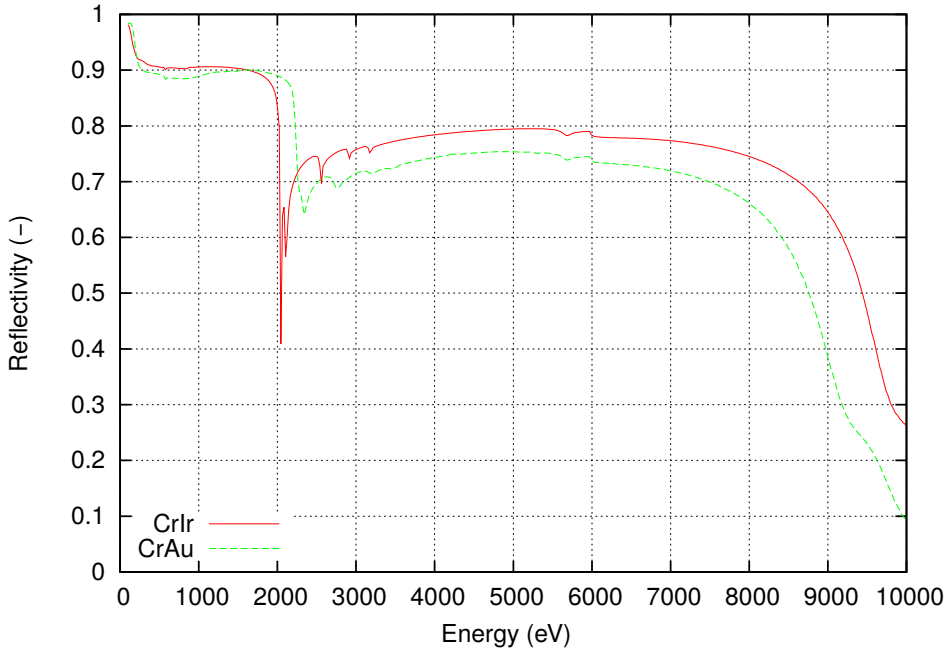


**Fig.** 4.5: Difference between golden and iridium coating of the same thickness for incident angle 0.5 deg.

overlayer when changing incidence angle of incoming ray exactly at the binding energy (right figure). The effect of levelling the gaps is clearly visible, thicknesses 4 and 6 nm are accompanied by reference iridium-only surface.

The thickness of the overlayer was scaled from 2 nm to 8 nm. The effect on the reflectivity is antagonistic at low and at high energies. The border between these areas creates the K1 line at 5 989 eV, where the reflectivity of pure chrome layer drops under 10 %. Looking at the figure 4.6, the thickness of overlayer degrades the reflectivity of iridium equally, but the improvement in the softer rays is more exponential. Preparation of layer thicker than 6 nm seems meaningless, only degrading the high energy part; as ideal thickness for real experiments were chosen 5 nm and 6 nm.

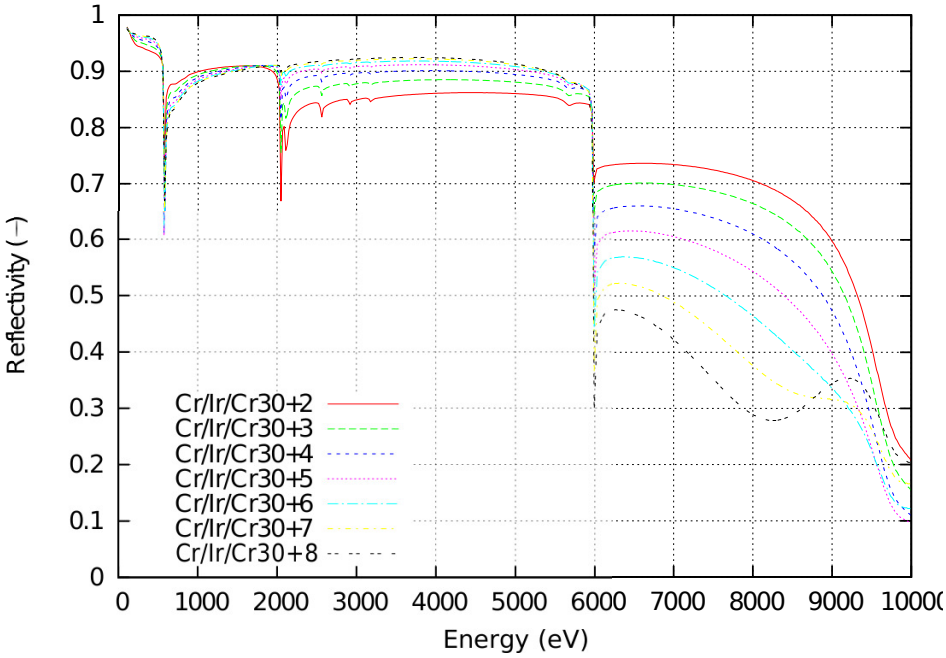


**Fig.** 4.6: The 30 nm thick reflective iridium surface on 90 nm adhesive chromium interlayer, covered by different thickness (2 nm - 8 nm) chromium overcoating which improves the reflectivity of mirrors at lower energies

For a better comparison between the chosen possibilities, there is Fig. 4.7. The best choice seems to be the combination of main iridium reflective layer and 5 nm thick chromium overlayer. It levels the gaps caused by iridium electron binding energies and concurrently does not cause too critical energy losses in the rest of the studied energy range. It is necessary to count with imperfect homogeneity of the layers, which can cause fluctuations of layer thickness $\pm 1$ nm. Although, this value is small, in the context of Fig. 4.6 is obvious that the effect is not negligible.

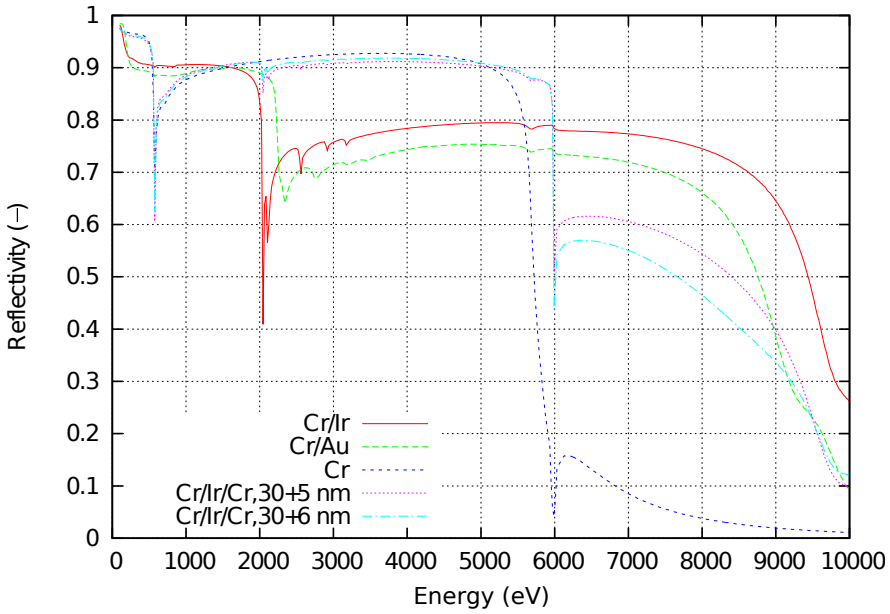


**Fig.** 4.7: The 30 nm thick reflective iridium surface on 90 nm adhesive chromium interlayer, covered by different thicknesses of chromium overcoating which improves the reflectivity of mirrors at lower energies.

# 5 Manufacturing experimental samples

This chapter describes the sputtering facility, various samples which were produced, and their test methods and results.

Experimental samples for testing were prepared with author's participation at the University of Applied Sciences Aschaffenburg. During the course of development, various combinations of layers and materials were manufactured. For coating, a sputtering facility which can provide two sputtering targets at once was used. This made it possible to prepare multiple layers using two different materials without opening the sputtering machine to swap the targets.

In Aschaffenburg, they already had rich and positive experiences with coating glass substrates with iridium layers [57, 58]. However, better surface quality, like microroughness and flatness, was achieved using silicon wafers. Silicon was accordingly used for hybrid demonstrator preparation, as is described and simulated in Chapter 4.
A tri-layer coating showed the best performance and was chosen as the final design for the experimental optic.

## 5.1 Sputtering facility and test devices

All discussed experimental layers were deposited using a direct current (DC) regime of magnetron sputtering machine VPA 21 produced by Aurion Anlagentechnik.
A schematic representation of the machine can be seen in Figure 5.1.

The chamber was equipped with Cr and Ir targets, with diameters of 6 inch and a purity of 99.9%. The targets are placed 120 mm above the substrates, and their inclination with respect to the substrate is 45°. Substrates lay on the table, which can rotate to reach better homogeneity of the layers. During plasma etching and layers deposition, this plate rotated at 8 RPM. Because the sputtering time for top layers was much shorter then for the primary layers, the rotation of the table was increased to 20 RPM during this phase. Power has been adjusted to the different phases as well. For plasma etching in the beginning, the power was 600 W. For sputtering itself, the power was reduced to 300 W. As the operating gas carrier served high-purity argon with a flow of 50 sccm [1].

The mirrors were tested during the development in Aschaffenburg and in Prague, using various measurement devices. To check the planarity of mirrors, a Zygo New View 7300 white-light interferometer was used. For measurement of layer thicknesses,

[1] Standard cubic centimetre

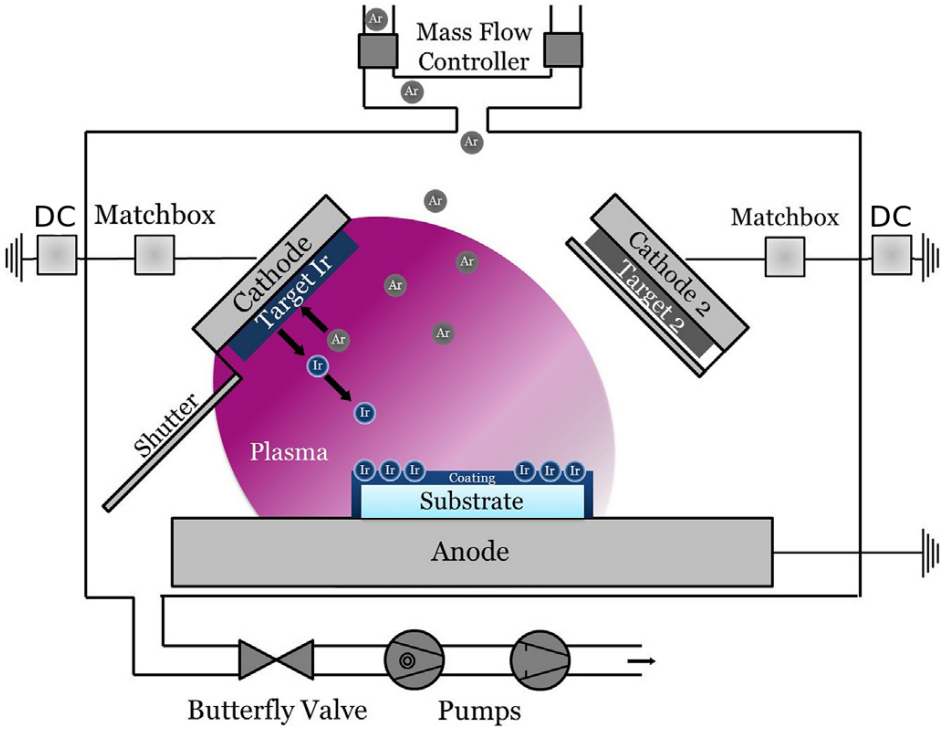


**Fig.** 5.1: Schematic of sputtering machine with two targets [59].

a tactile profilometer Dektak XT from Bruker with stylus radius of 12.5µm was available. The microroughness measurements were obtained using AFMs (atomic force microscopes) Asylum Research MFP-3D microscope and Ntegra. Adhesivity tests were performed as described in the ISO2409 norm.

## 5.2 Preparation and tests of the test samples

In the beginning, a set of sample silicon mirrors coated with iridium was prepared. These samples were planned to be the prototypes of iridium coated silicon mirrors for a lobster eye optic, whose production was expected to be the next step. Their size was larger than the planned size of the mirrors for optic demonstrator, 75 mm × 150 mm. They were accompanied by the witness samples - small pieces of Si and glass, lying around the mirrors. One side of the silicon wafer is polished by the producer, the other is matt. We were coating the polished side of the wafer, which, as we measured, has the microroughness in range 0.08 - 0.17 nm. Iridium was sputtered directly on the polished surface, to obtain the smoothest possible layer.

The mirrors were prepared in two steps. At first, the silicon substrate was plasma-etched for 120 s. Plasma etching cleans the surface of the substrate, in case there were present any impurities caused by storage and handling. This was followed by a 50 s pre-sputtering process and 190 s of Ir sputtering.

The prepared samples were visually checked and stored under standard clean room conditions. A sample of an iridium coated mirror in comparison with a silicon wafer can be seen in Figure 5.2. The witness samples were used to check the thickness of the layers. To do this test, part of the witness sample was covered by removable mask during the sputtering process, either by isopropanol-removable paint, or a piece of glass. The thickness of the layer was then measured using the profilometer. This way, we have verified that we prepared the expected 50 nm Ir layers. The microroughness of the layers was verified as well, and was found to be in range of 0.34 - 0.49 nm. These values are much higher in comparison with the surface quality of polished silicon wafer, but are still fulfilling the demands of the mirror design. The increase of microroughness is caused by the structure of growing layer, which is in the required thickness expected to be crystalline.

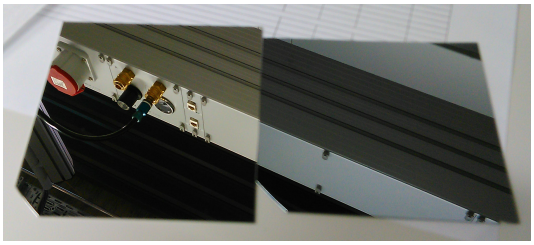

**Fig.** 5.2: Comparison of a mirror coated with iridium (on the left in the picture) and bare silicon substrate (on the right). [60]

**Fig.** 5.3: Delamination of iridium layer applied directly on silicon substrate. No adhesive layer was applied. [60]

After two months of storing the mirrors, we wanted to take out another couple of witness samples to repeat the microroughness measurement. Checking the large samples, a problem with the stability of the iridium layer has been discovered. Full-sized samples were covered in peeled-off rolls of iridium, which lost the contact to the silicon surface. Delamination of iridium occurred on the silicon samples only - the witness samples on glass substrates remained of original quality. Degradation of the reflective surface, as was imaged by an optical microscope, is illustrated by Figure 5.3.

We repeated the coating process with the same parameters to purposefully test the adhesion of the iridium layer. It turned out that the layer is not unstable only over the time. Right after production, it was possible to destroy the iridium layer by gently rubbing the surface with a soft piece of cloth, as well as by rinsing the surface with isopropanol.

The deduced reason of delamination was the internal stress of the iridium layer. The problematic of stress in the layers and the possible usage of Cr layer as compensation on glass substrate was studied at the TH Aschaffenburg in the past, as is described in [61].

The next batch of mirrors with witness samples was prepared with an adhesive chromium layer of 70 nm thickness, between the silicon substrate and the reflective iridium layer [43, 54, 55]. These mirrors then underwent an adhesion test according to ISO2409 norm [60]. Comparison of test results for a mirror with and without chromium adhesive layer can be seen in Figures 5.4 and 5.5. The mirrors with adhesion layer did not show any delamination during the test.

The samples were stored under standard clean room conditions over a period of about 18 months, before the tests described in the next section. The surface of the remaining mirrors has been regularly visually checked since 2017 without any signs of delamination, which is up to now 6 years (in 2023). Thus, the compensated Cr/Ir layers can be considered environmentally stable.

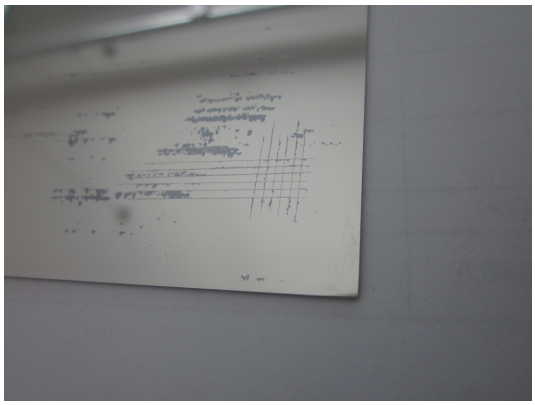

**Fig.** 5.4: Adhesion test - iridium sputtered directly on the silicon. Degradation and peel-off effect occurs on the whole surface, not only in the testing area (a grid of scratch lines visible in the bottom right corner of the sample) [60].

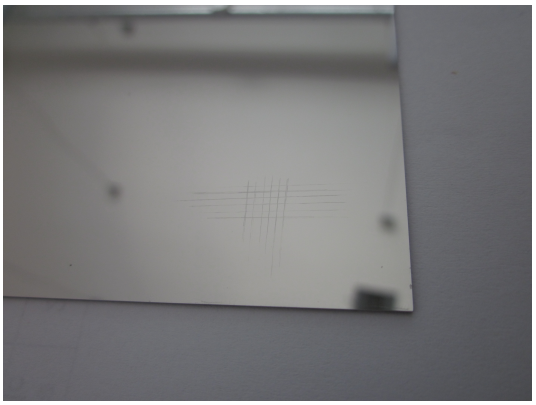

**Fig.** 5.5: Adhesion test - iridium with chromium adhesive layer. In this case, no peel-off occurs, and the testing scratches have defined, clean edges [60].

## 5.3 Reflectivity test samples preparation

After resolving the issues with environmental stability of the Ir/Si mirrors, the batch of final mirrors could have been prepared. However, during this period, I have developed a new idea regarding the layers composition - the idea of using thin overcoats to improve the mirror's properties, as is described in Chapter 4. Thus, the primary focus moved towards testing the reflectivity of these proposed Cr overcoatings. Instead of mirrors for lobster eye modules, a set of 4 samples with different overcoat thicknesses was manufactured according to the presented simulations.

The planned experimental optics, as described in section 3.2.5, is supposed to be produced from lightweight, thin sheets of silicon. However, to prevent possible disturb-

ing influences, for example varying surface quality or substrate deformation caused by tension of the layers, the mirror samples use as the substrate thick, sturdy borosilicate glass plates. With dimensions of 150 mm of diameter and 6.5 mm of thickness, and taking pieces from the same batch, we consider these to be identical to each other and stable enough. Hence, we assume that the differences between the results arise from the differences between the overcoating thicknesses, not from substrate influence.

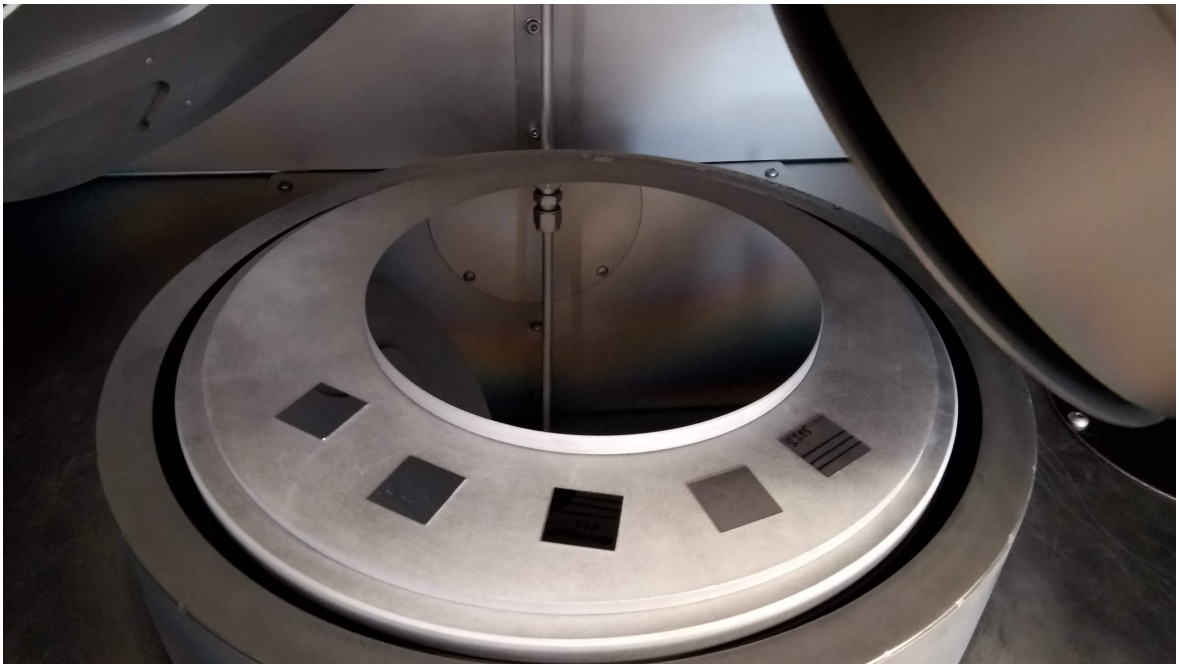

**Fig.** 5.6: Photo of the round mirror sample inside of the sputtering machine. Around the main mirror are small witness samples. On the very right, a sample with stripes can be seen - this one serves to check the layers thickness.

To coat these test samples following reflective layers were prepared, using again the DC sputtering method. As the adhesive layer serves a 40 nm layer of chromium. As the main reflective layer a 30 nm layer of iridium. And as the overcoating, additional 4, 6, 8, and 10 nm of chromium. A fifth mirror without chromium overcoating serves as the reference piece.

The 150 mm wide, round substrates were placed on the rotating plate in the sputtering facility. As in the other cases, also these mirrors were accompanied by witness samples, on both glass and silicon. The mirror and its companions can be seen in Figure 5.6.

The four mirrors with thin overcoatings and one mirror without were then visually checked, packed and delivered to MPE's X-ray facility PANTER for reflectivity test. Description and results of this test are given in detail in Chapter 7.

**Tab.** 5.1: Facility settings during preparation of layers demonstrators with different thicknesses of chromium overcoatings. Last three lines show sputtering process for chromium overlayers, from 4 nm to 10 nm.

| Step | t (s) | Material | Gas | Flow (sccm) | T (°C) | p (hPa) | P (W) |
|---|---|---|---|---|---|---|---|
| Plasma etching | 120 | - | N2 | 30 | 25 | 5e-2 | 600 |
| Pre-sputtering 1 | 60 | Cr | Ar | 50 | 25 | 5e-2 | 300 |
| Pre-sputtering 2 | 60 | Cr | Ar | 50 | 25 | 2.5e-2 | 300 |
| Sputtering | 183 | Cr | Ar | 50 | 25 | 2.5e-2 | 300 |
| Pre-sputtering 1 | 10 | Ir | Ar | 50 | 25 | 5e-2 | 300 |
| Pre-sputtering 2 | 40 | Ir | Ar | 50 | 25 | 5e-3 | 300 |
| Sputtering | 189 | Ir | Ar | 50 | 25 | 5e-3 | 300 |
| Pre-sputtering 1 | 60 | Cr | Ar | 50 | 25 | 5e-2 | 300 |
| Pre-sputtering 2 | 60 | Cr | Ar | 50 | 25 | 2.5e-2 | 300 |
| Sputtering | 19/29/39/49 | Cr | Ar | 50 | 25 | 5e-3 | 300 |

## 5.4 Mirrors for hybrid optic demonstrator

PANTER, BESSY and TEM tests of the mirror bash with the various overcoatings lead to the decision which option is best to use for the lobster eye demonstrator's mirrors. Taking into consideration various parameters, for example the improvement of X-ray reflectivity and the layer uniformity and stability, the 6 nm overcoating was decided to be manufactured.

Four silicon wafers with dimensions 50 mm × 100 mm × 0.625 mm can be placed into the sputtering machine at one run. With a process time about 2 hours per run, the production of the whole set of 32 mirrors plus several spares took about three days of work. The parameters of the process were in agreement with the sputtering process during the preparation of the round reflectivity test samples.

Also for these mirrors, thickness measurement of witness samples was performed. Using masking during sputtering enabled to quantify the layer thickness. The variation of the chromium overlayer was ±0.11 nm.

The AFM measurement of surface microroughness showed expected rising trend in dependence on thickness. The obtained RMS values range from 0.17 nm to 0.41 nm. That means, even the worst prepared mirror sample fulfils the requirement of RMS <0.5 nm.

After finishing the whole batch, checked mirrors were packed in clean transport boxes and shipped to partner company Rigaku in Prague. Here, the mirrors were integrated into two sub-module housings of lobster eye optic, the optic was checked for focal length and manufacturing quality, and then shipped to MPE's PANTER X-ray facility for testing. The manufactured optics can be seen in Figure 5.7. Description and results of these tests are given in detail in Chapter 9.

In the end of this chapter, I would like to point out the interconnected character of Chapters 4, 5, and all the Chapters describing the testing, from TEM tests to the final HORUS tests. The models of layers, as were described in Chapter 4, were changed with each production and measurement iteration. Mean values of microroughness for individual layers, as the process was improved, were updated in the model, to ensure the prediction is close to the physical samples. After studying the TEM images, measured influence of chromium oxidation was included. The final produced mirrors used in the HORUS optics are the result of all empirical measurements and experiences, gained on the way, and included in final model.

The next chapters in this thesis do not represent the chronological order of the development cycle, but lay out the separate blocks of it. Accordingly it should be kept in mind that individual parts of the thesis were directly influencing the work on the others, achieving positive results through a reproducible, converging iteration cycle.

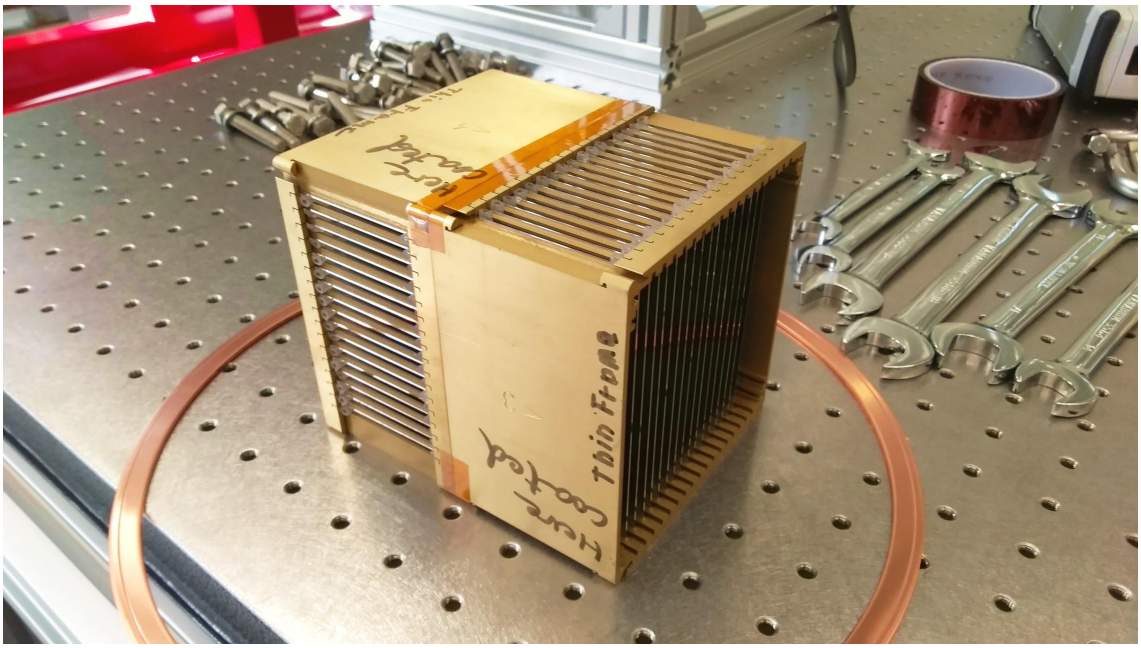

**Fig.** 5.7: Manufactured module with one-side iridium coated mirrors in Schmidt's arrangement. Notes helped with orientation of PANTER facility crew during the X-ray measurement campaign.

# 6 TEM test

Designed sandwich layers from two materials, chromium and iridium, show good performance in the simulations. However, we knew that the chromium overlayer will change during the storage period in normal atmosphere - the material will create a chromium-oxide layer on top, which should reach 0.9 - 1.5 nm thickness, before the equilibrium will be established [62]. To check the oxidation behaviour, which is supposed to lead to the formation of a $Cr_2O_3$ layer, we used transmission electron microscopy (TEM), provided by a laboratory at the Institute of Physics of the Czech Academy of Sciences. Combining different methods of measurement, we obtained a detailed picture of the layers. The results were more information rich then expected and uncovered unforeseen proprieties, as is described in this chapter. To get results corresponding to prolonged storage times, an older batch of the sandwich layers sputtered on glass was used - the samples were 1.5 year old prior the preparation of TEM slice specimen.

## 6.1 Specimen preparation

To check the layer composition, two specimen types were used. First was the most promising variant regarding the simulated reflectivity rise, an iridium main reflective layer with 6 nm chromium overcoating. Second was the thickest option we considered, simulated and produced, the main reflective layer equipped with 10 nm of chromium overlayer.

For performing the TEM measurement, the samples have to be translucent for the microscope. Thus, a thin slice of material is cut out from the prepared mirror piece [63]. The thickness is less than 100 µm with the cutting direction through the reflective layers and into the substrate. For the measurement, several such slices were prepared, then the ones with best thickness homogeneity underwent the measurements.

Because the the handling of the specimens under normal atmosphere would cause the build-up of oxide on the cut, they were prepared under protective nitrogen atmosphere and covered in resin. For presented two overlayer thicknesses (6 nm, 10 nm), following samples were measured:

- 10 nm sample - thick lamella from the edge of the mirror
- 10 nm sample - thick lamella from the centre of mirror
- 10 nm sample - thin lamella from the centre of mirror
- 6 nm sample - thick lamella from the centre of mirror
- 6 nm sample - the same, just thinned lamella from the centre of mirror

Thick samples served to get information using methods like EELS (Section 6.2.3). Thin samples are used for other methods, giving more details.

The samples were prepared using the FIB (focused ion beam) technique performed with an FEI Quanta 3D FEG. Cutting and thinning is achieved by aiming an energetic, focused gallium ion beam on the sample. The ions are accelerated using an electromagnetic field, and focused on the sample using magnetic lenses. The atoms are kinetically sputtered off the sample surface and this way, the desired thickness of the lamella can be reached. To acquire the best possible surface quality and thickness homogeneity of the lamella, the cut sample is at first coated with a layer of protective resin. The encasing resin, providing machinable bulk of the material, contains among other materials tungsten (W). The thinning process can also cause deposition of Ga ions into the surface of the specimen. The implanted material, as well as the resin, can be later found in the analysis and it is important to know about their origin in order to prevent wrong conclusions.

## 6.2 TEM results description

In this section are presented results from various analysis methods for both types of samples. The sub-sections show the results of various methods, which are concluded in the next section. Various analysis methods are required to fully quantify the heterogeneous composition with mixed crystalline and amorphous structures, and a difference in relative atomic mass of up to a factor of 12.

### 6.2.1 Diffraction view on sputtered layers

Fig. 6.1 shows the TEM diffraction pattern, averaged over several measurement locations on one sample. Integration of the rings, analogous to X-ray powder diffraction (XRD), shows the crystalline phases of the elements. The darker the areas in the Fig.6.1 are, the closer is the material to the Bragg condition - the ideal diffraction orientation. Sharp features show the crystalline structures of both Cr and Ir. The blurred halo indicates the presence of an amorphous Cr-Ir phase. Figure 6.2 shows the distribution of identified elements in diffraction scan. Green colour represents the cubic chromium, blue colour the cubic iridium. The widening in the chromium is caused by the oxygen, which is chemically bonded, forming chromium-oxide.

### 6.2.2 EDX

The energy-dispersive X-ray spectroscopy (EDX) was used to analyse the chemical composition of the layers. The sample was analyzed by a scanning electron microscopy (SEM) setup (TESCAN Vega 3) equipped with an EDX spectrometer (Brukker Detector 5010). This method enables to obtain information about present elements and their distribution.

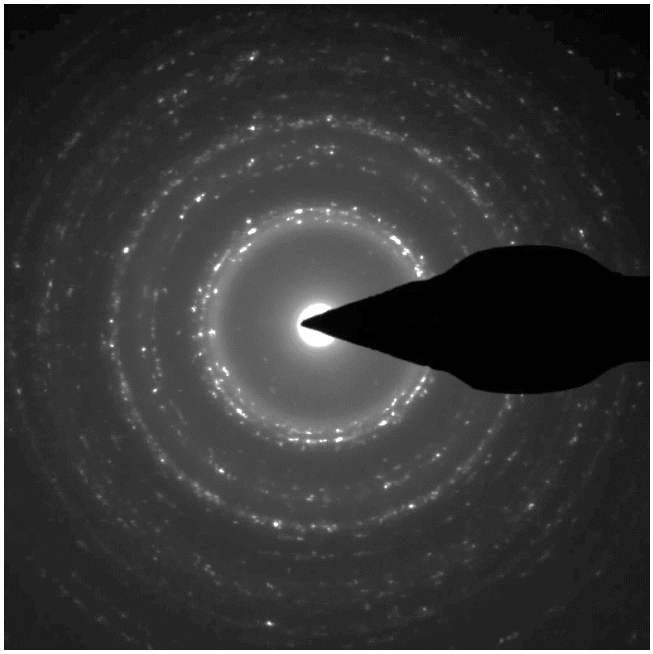

**Fig.** 6.1: One of the TEM images showing the diffraction pattern, indicating the presence of crystalline phases of Cr and Ir in form of bright points, and amorphous chromium as halo.

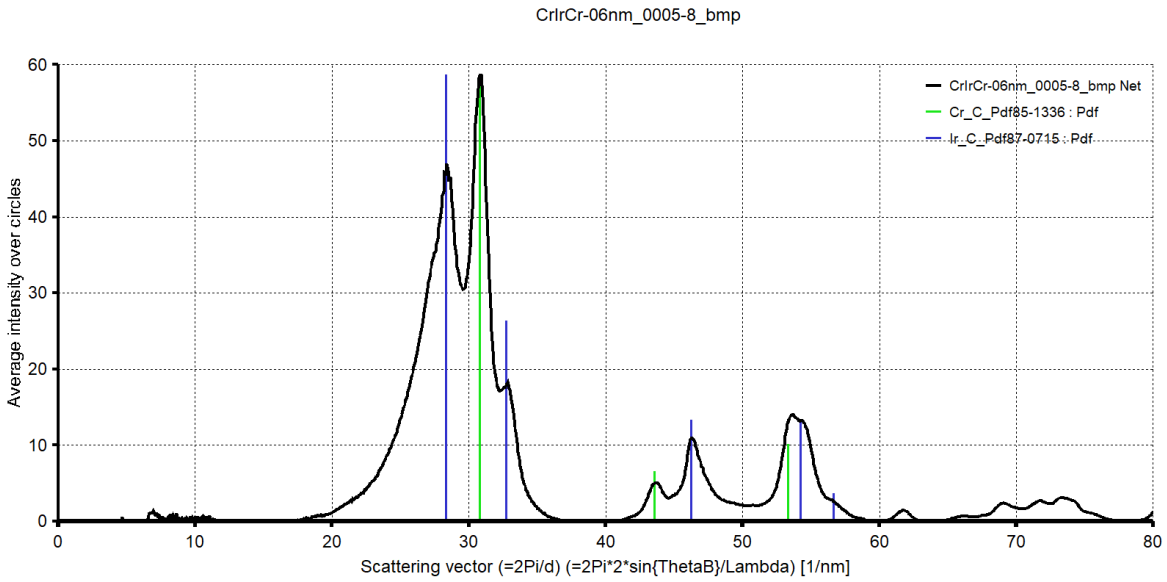


**Fig.** 6.2: Distribution of identified elements in diffracting scan.

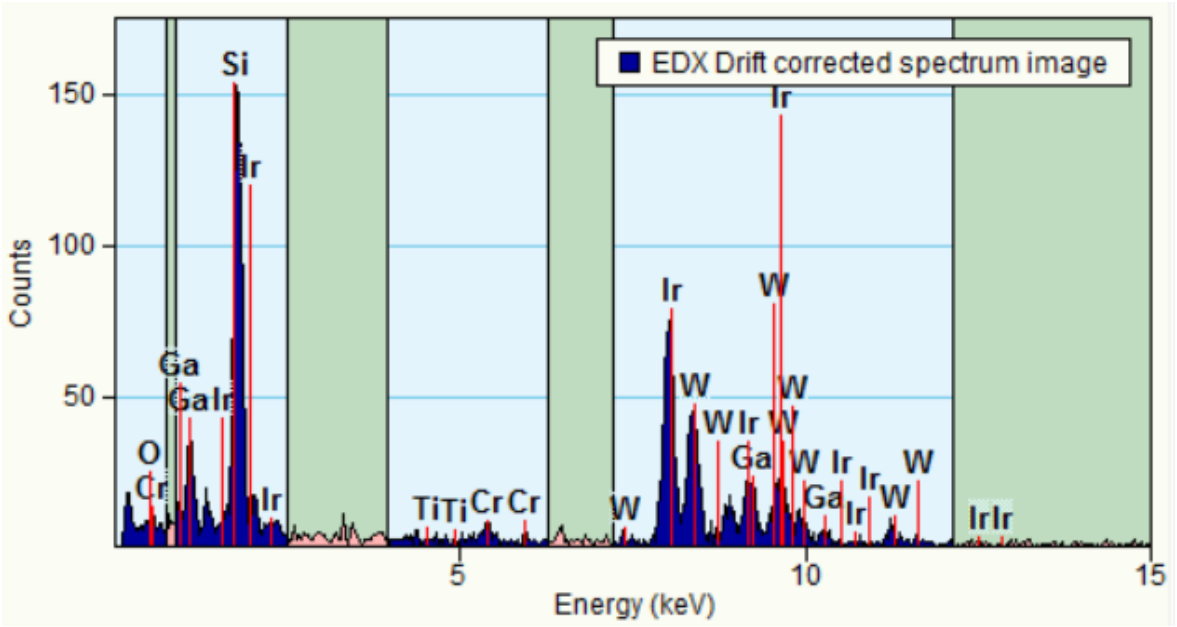


**Fig.** 6.3: EDX spectrum with contributions labelled according to source element.

During the EDX measurement, a focused electron beam excites electrons at the inner shell. The vacancy is filled up by another electron, originating in an outer shell, which emits an X-ray photon. The set of energies of such photons is unique to a specific element, thus the composition of studied material can be obtained.

The EDX spectrum, like shown in Figure 6.3, contains contributions from all present elements. Unexpected was the presence of titanium, as it is neither part of the protective resin, nor the reflective layers. Upon request the glass producer clarified that the glass substrates had a titan oxide lacquer on their surface. As it is the deepest layer, it is not disturbing the reflectivity in our case.

For future projects an initial analysis for remnants of technical materials not explicitly listed in the materials datasheet is recommended. Generally, impurities, especially in full area coatings, could affect manufacturing processes like sputtering in terms of material adhesion, homogeneity, and finally reflectivity.

### 6.2.3 Electron energy loss spectroscopy

To obtain information about the elements in the sample, electron energy loss spectroscopy (EELS) was used. This is an extension to scanning transmission electron microscopy (STEM) mode, where the beam is focused into a point of $\approx 1\,\mathrm{nm}$ size, scans over the specimen and gradually creates an images. EELS method is most suited for measurement of lighter elements layers, here was used to evaluate the thickness of the chromium-oxide and chromium overlayer.

EELS scan shown the thickness of the chromium overlayer and the depth of the oxidation. For 10 nm thick sample, the chromium was found in thickness of $11.8 \pm 1.3$ nm. From this layer, chromium oxide represented $6.5 \pm 0.7$ nm. For 6 nm thick sample, chromium overlayer had $11.3 \pm 4.4$ nm. Oxidised part was $6.5 \pm 2.1$ nm thick. The errors are in case of 6 nm overcoating larger. Looking at images 6.6 and 6.8 suggests that the 6 nm layer is in fact thinner than the 10 nm layer. The boundary between the chromium overcoating and iridium layer is more irregular and the chromium layer is less homogeneous. These influences affected the preciseness of EELS method, which is not anymore suitable for performing measurements on such a small scale.

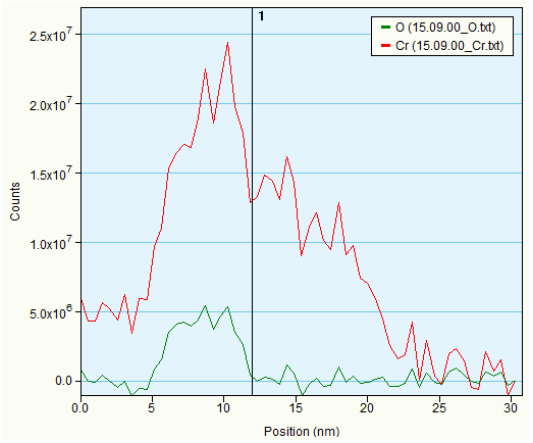


**Fig.** 6.4: Result of EELS analysis of 10 nm thick chromium overcoating. The measurement started from the resin towards the layers. At first appears signal of both oxygen and chromium. This could be evidence of the presence of $Cr_2O_3$ layer. Deeper into the mirror surface, the oxygen signal disappears, while chromium stays. This shows that the oxidation stops in certain depth and does not affect the overlayers in their full thickness.

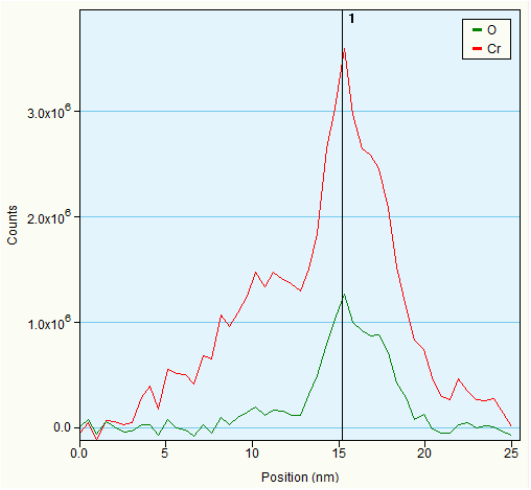


**Fig.** 6.5: Second EELS scan of a 10 nm overcoated sample. This time, the measurement started from the depth of layers, heading from iridium layer towards the mirror surface. At first appears the chromium, then joins the oxygen in the overlayer. Even in this measurement, the oxidised and pure chromium layers are clearly recognisable, and their ratios are comparable with measurement on the first sample.

### 6.2.4 HRTEM scan

In the high-resolution transmission electron microscope (HRTEM) mode, the whole specimen was illuminated by a parallel beam. The HRTEM data for the structural investigation and images of the sample were recorded on a TEM with a LaB6 cathode operating at 120 kV. The microscope was equipped with a DigiStar (NanoMegas) pre-

cession device, a CCD Camera and EDAX energy dispersive X-ray detector Apollo XLTW.

In Figures 6.6 and 6.7 is depicted the sample of the mirror with 10 nm thick overcoating. On the glass substrate are well formed crystals of chromium and iridium in various orientations. The overcoating shows presence of chromium oxide, as was expected. The thin chromium layer, probably due to very short sputtering process and overall thinness of the layer, did not form any crystalline structure. Instead, the chromium formed an amorphous layer. As can be seen in the scans, the surface of this amorphous layer is smoother than the crystalline structures underneath. This finding corroborates the previous finding from AFM measurements (Chapters 4, 5) where the surface micro-roughness of the final layer was determined to be lower ($\approx 0.4$ nm RMS) than expected for a crystalline layer, given the values of the chromium and iridium interlayers ($\approx 0.35$, respectively 0.50 nm RMS).

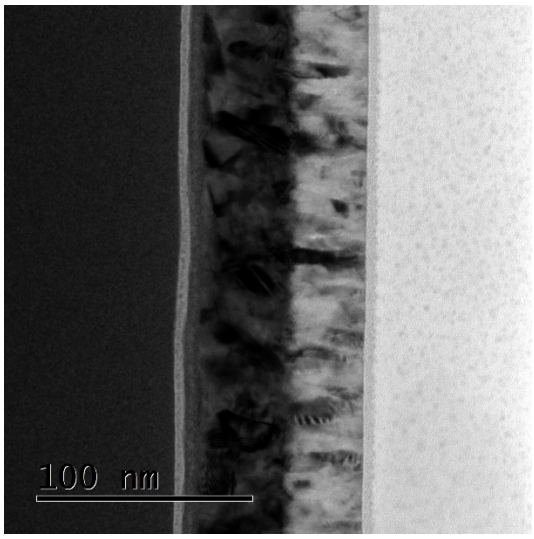


**Fig.** 6.6: Image obtained in HRTEM, 10 nm overcoating. From left to right are recognisable the oxidised layer of chromium and chromium overcoating, dark-coloured iridium and lighter-coloured chromium layers with visibly crystalline structure, and very light-coloured glass substrate.

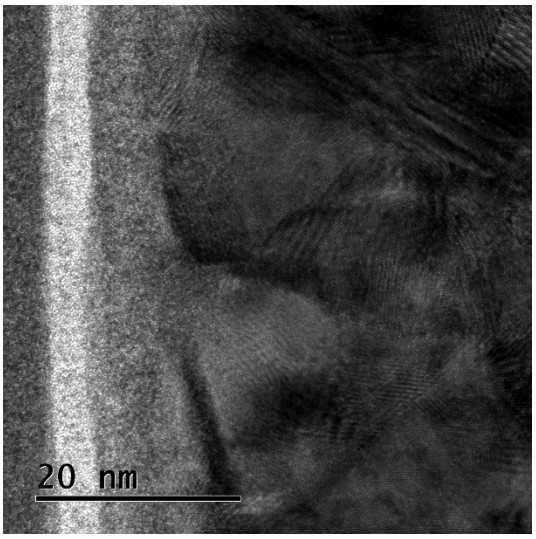


**Fig.** 6.7: Detail of chromium overcoating. In lighter colour the oxidised chromium, in grey the amorphous layer of pure chromium. Dark coloured iridium, with distinctive crystalline structure in various orientations.

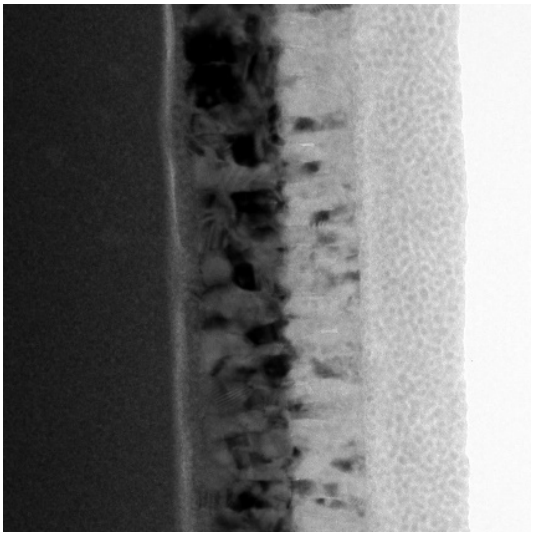

**Fig.** 6.8: Image obtained in HRTEM, 6 nm overcoating. The oxidised layer of chromium and chromium overcoating are less defined in comparison with images of 10 nm overcoating. Smoothing effect of amorphous layer is less strong.

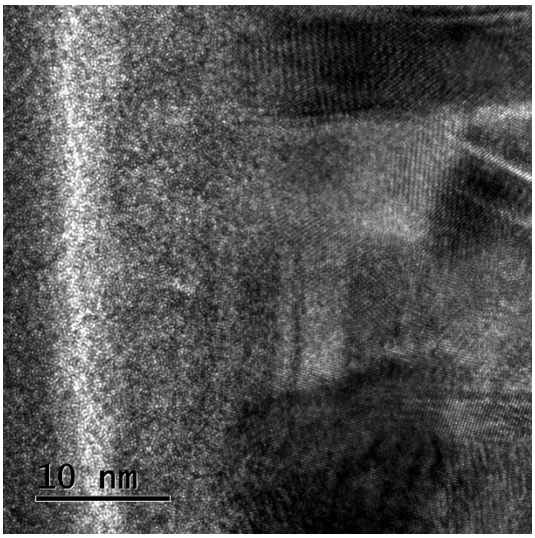


**Fig.** 6.9: Detail of chromium overcoating. In lighter colour the oxidised chromium, in grey the amorphous layer of pure chromium. Dark coloured iridium, with distinctive crystalline structure. Thickness of oxide layer as well as the whole chromium overcoating indicates higher variability than in case of 10 nm overlayer.

## 6.3 TEM findings - conclusion

Looking closely into the layer structure lead to important insights for designing multiple layers. First of all, the nano-layer overcoating of chromium stays amorphous, instead of crystallising. The observed amorphous structure is reducing the microroughness of the surface, compared to the stacked crystalline layers below.

Another important finding was that the chromium and iridium layers are not fully separated after the deposition. Instead, at least two Cr-Ir binary mixed phases were identified. These areas blur the transition between the crystalline chromium in the adhesive under-layer and the main iridium reflective layer. The formation of mixed phases should be considered in future multi-layer designs, as for thin layers, the effect could greatly influence their properties.

Better understanding of the Cr-Ir structures would require similar in-depth analysis of several more thickness variations. The two samples studied here showed the mixed phases only between the crystalline forms of the metals, i.e. the adhesive and the main reflective layers. The small Cr-Ir overlap reported between the main iridium layer and the amorphous over-coating results from the evaluation method and roughness of the interface, not from an actual presence of mixed phases.

The formation of chromium oxide, expected according to other studies, was confirmed on the surface of chromium overlayer. While being stored in normal atmosphere, the oxygen from the air reacts with the chromium surface, creating a layer of oxide. The analysis has shown that the thickness of this oxide layer was comparable between the investigated layer types. Thus it is confirmed that the oxidation of chromium nanolayers occurs, but is reproducible and can be modelled. This is important, as the oxide has influence on the reflectivity.

# 7 X-ray testing of the first set of experimental samples

The first test campaign was done at PANTER, which is a long-beam X-ray facility in Neuried southwest of Munich, part of Max Planck Institute for Extraterrestrial Physics (MPE). The facility provides measurements in ultra-high vacuum (UHV) of the order of $10^{-7}$ and an almost parallel beam. Discrete X-ray energies can be chosen in the range from 0.2 to 10 keV, using a target source. The test campaign aimed on direct comparison of various thicknesses of chromium-iridium-chromium sandwich's overcoatings, as described in Chapters 4.

For this experiments, a batch of five sturdy round mirrors was used. The detailed description of them is given in Chapter 5 and in Table 7.1.

All five mirror samples were tested in the reproducible experimental setup and for the same X-ray energies, as is explained in the next section. The PANTER facility is able to provide several targets with different elements (see table 7.2) plus filters that restrict the out-coming radiation to almost the energy corresponding emission line of the target.

From the measured data, including the data analysis, error propagation, and geometrical correction, can be gained the reflectivity of each sample.

## 7.1 Experimental setup

The mechanical setup of the PANTER testing facility was adapted to the measurement purpose. It included several elements in following configuration:

- X-ray radiation source with aperture of 15 mm
- Optical mask placed in distance 1188 mm from the middle of the active test sample (Fig.7.1)
- Sample wheel mounted on a manipulator (Fig.7.2)
- TRoPIC detector

The setup from the direction of the X-ray source can be seen in Figure 7.1. The optical mask on the left is a slid of 10 mm to 0.25 mm dimension. This size was chosen as it will provide a well defined beam aperture, which with the change of incidence angle will not exceed neither the surface area of the mirrors, nor the active area of used TRoPIC detector. The sample wheel in the middle (close up view in Figure 7.2) is rotatable. During test, its rotation will bring the measured mirror into the upper position, where the X-ray beam from the mask slid aims. The sample wheel is mounted on a manipulator enabling translational and rotational moves. During tests, the manipulator will provide pitch change to vary the incident angle of incoming rays on the

**Tab.** 7.1: Panter X-ray test: List of samples and their identification numbering.

| Sample number | Coating composition (from top) |
|---|---|
| 1 | Ir 30 nm / Cr 40 nm |
| 2 | Cr 4 nm / Ir 30 nm / Cr 40 nm |
| 3 | Cr 6 nm / Ir 30 nm / Cr 40 nm |
| 4 | Cr 8 nm / Ir 30 nm / Cr 40 nm |
| 5 | Cr 10 nm / Ir 30 nm / Cr 40 nm |

sample surface, roll for keeping spatial homogeneity of photon distribution over the slid area, and sideways move to obtain flat field images without sample reflection for reference. To obtain data, the X-ray camera TRoPIC, which can be seen on the right in the Figure 7.1, was used. TRoPIC is a solid state pnCCD camera, a prototype of the ones used at eROSITA, with operating temperature below -90 °C and a framestore. With a pixel size of 75 µm × 75 µm, a cycle time of 50 ms, an out-of-time event fraction of 0.2%, and a 256 × 256 pixel FOV (19.2 × 19.2 $mm^2$) it is well suited for point-spread function (PSF) measurements and high-resolution imaging [64, 65].

The X-ray source provides radiation at specific energy levels corresponding with the source target. The X-ray source and the test chamber, where optics and detectors are located are connected by an approximately 120 m long evacuated tube that provides an almost parallel beam.

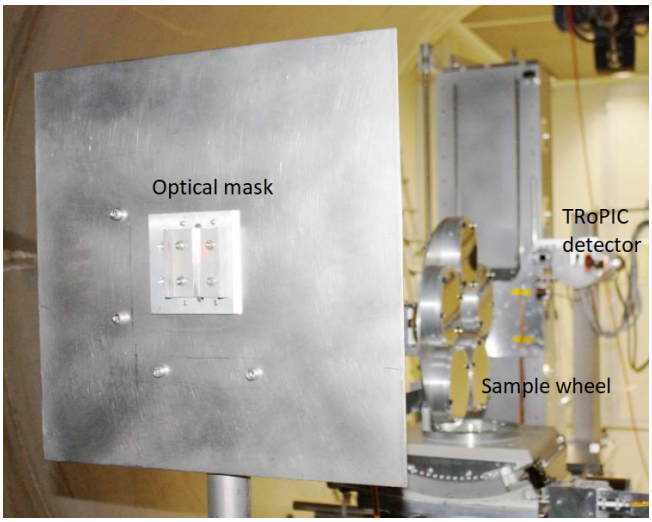


**Fig.** 7.1: The optical mask inside the PANTER chamber, with the sample wheel behind the mask (view is towards the detector). The alignment laser is visible on the optical mask slit.

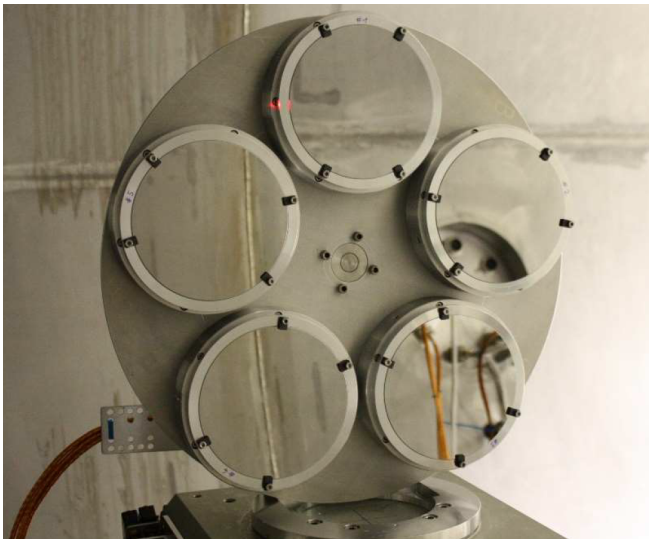

**Fig.** 7.2: The five mirror samples mounted in the sample wheel holder. Image from inside the PANTER chamber, the wheel stands on manipulator.

## 7.2 X-ray sources of interest

The X-ray source energies were chosen according to the interesting points predicted by simulation on the reflectivity curve, as described in chapter 4. In the Fig. 4.7 can be seen how the expected reflectivity changes in dependence on element absorption lines, namely Cr-L and Ir-M lines influence. Because an iridium target is not available at the measuring facility, in this testing phase it was not possible to choose exactly the energies which correspond to the energy edges of interest (around 2050 eV). On the other hand, a chromium target was available and used.

Reflecting this fact, I decided to choose two sets of energies. The first set is based on calibration campaign of eROSITA X-ray mirrors and cameras [20], which was performed at PANTER and the experience obtained during these measurements could be also used during my tests. The second set is an enrichment for a couple of energies which can PANTER provide and which are as close to the energy range of interest as possible. The quasi monochromatic measurements all are within the energy range from 280 eV to 8.04 keV, or from 4.43 nm to 0.15 nm wavelength, respectively

The energies and the source targets are listed in Table 7.2. Here, the eROSITA inspired test set is the base, and the additional energies are marked with an asterisk.

**Tab.** 7.2: Panter X-ray test of samples with different over-coating thicknesses: used element lines, corresponding energy and wavelength.

| Element line | Energy (keV) | Wavelength (nm) |
|---|---|---|
| C-K | 0.28 | 4.43 |
| O-K | 0.53 | 2.34 |
| Cu-L | 0.93 | 1.33 |
| Al-K | 1.49 | 0.86 |
| W-M* | 1.78 | 0.69 |
| Au-M* | 2.14 | 0.58 |
| Ag-L | 2.98 | 0.42 |
| Cr-K | 5.41 | 0.23 |
| Fe-K | 6.40 | 0.19 |
| Cu-K | 8.04 | 0.15 |

## 7.3 Measurement plan

The sample wheel was placed into the vacuum chamber of Panter, with measured sample oriented as the top one. The measurements were done for rising incident angle. The mirror, after taking the direct beam count rate, was translated into the beam, checked that its surface is parallel to the beam and then tilted in optic pitch axe to the desired angles. The angles were chosen according to the source energy and mirror coating. For different energy lines, various sets of incidence angles were chosen, because the reflectivity of harder X-rays drops earlier with larger incidence angles. The general angles for different energies can be seen in Table 7.3. Some of the angles differ at some samples, according to the status of measurement. These cases are visible from the final figures, and to not exceed the dedicated space, only aforementioned table is kept for general orientation.

The tests run over eleven days. The sample alignment was done at first. Then, individual mirrors were tested one after the other at required energies and corresponding angles. Testing sequence was 8 nm, 10 nm, 6 nm, 0 nm, and 4 nm, using over-coating thickness for identification. This order was dependent on the absolute position of the sample wheel in the vacuum chamber. The results are later represented in more logical way, from lowest to highest overlayer thickness.

**Tab.** 7.3: Panter X-ray test: Incident angles used during the campaign, in dependence on the source energy.

| Element line | Angle (arcmin) |
|---|---|
| C-K (0.28 keV) to W-M (1.78 keV) | 18, 36, 42, 54, 72, 90, 108 |
| Au-M (2.14 keV) to Ag-L (2.98 keV) | 18, 36, 42, 54, 72, 90 |
| Cr-K (5.41 keV) to Cu-K (8.04 keV) | various, smaller steps up to 50 |

### 7.3.1 Laser alignment

At first, the alignment of the mirrors, respectively the sample wheel, in the vacuum chamber was done. The aim was to have the reflection from mirror always falling fully onto the detector surface. To make the alignment of the X-ray image on detector more simple, a laser beam is used, while the chamber is still opened and flooded with normal atmosphere.

The laser source is mounted in the same position like the X-ray source, and aligned to provide a beam with the same trajectory like the X-ray beam.

At first, the laser beam was auto-collimated: One after the other, each sample on the wheel was brought in a well defined position, where it faces the laser beam or later the X-ray source, respectively. All five stages of the sample wheel were checked. This process ensures that the samples are correctly aligned in rotation (pitch and roll).

Once auto-collimated, the sample wheel was rotated by 90°, thus being close to the small incidence angles, used in the reflectivity measurements. The optical mask was mounted in front of the sample wheel. This arrangement is depicted in Fig. 7.1. The passing through laser beam was used to centre the detector housing. Centred position of samples were noted, and the vacuum chamber was closed and pumped down.

### 7.3.2 X-ray measuring sequence

After switching to X-ray, further alignment steps followed. At first, the position for the direct beam was set. Because it was not possible to monitor the variation of the beam intensity with time, the direct beam was measured before and after each measurement. This way, one measurement sequence started with imaging the direct beam, then the selected mirror sample got moved into the beam, desired angle steps were set and measurements recorded, and in the end of this sequence, the sample wheel moved again out of the beam and a direct beam image was taken. The beam intensity variation is assumed to be linear with time, and is interpolated between these two direct beam measurements to derive a normalisation factor for each reflectivity measurement.

## 7.4 Measured versus simulated reflectivities

This part shows the results of reflectivity test campaign. All these figures are plotted using simulation based on [49] and obtained PANTER values. The lines represent the model prediction for various angles in interval from 0° to 2° with steps of 0.004°. Colours indicate the X-ray energies at which the tests were performed according to Table 7.2.

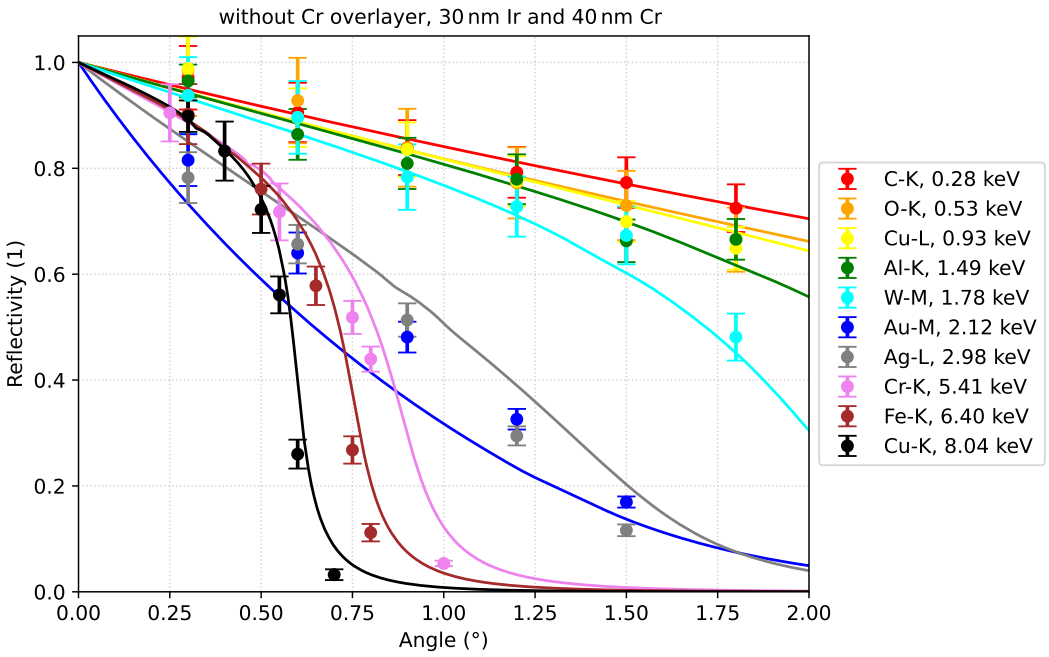


**Fig.** 7.3: Reflectivity measurement of sample without Cr overlayer. Lines represent model predictions, same colour circles are measurement results with $3\,\sigma$ confidence interval.

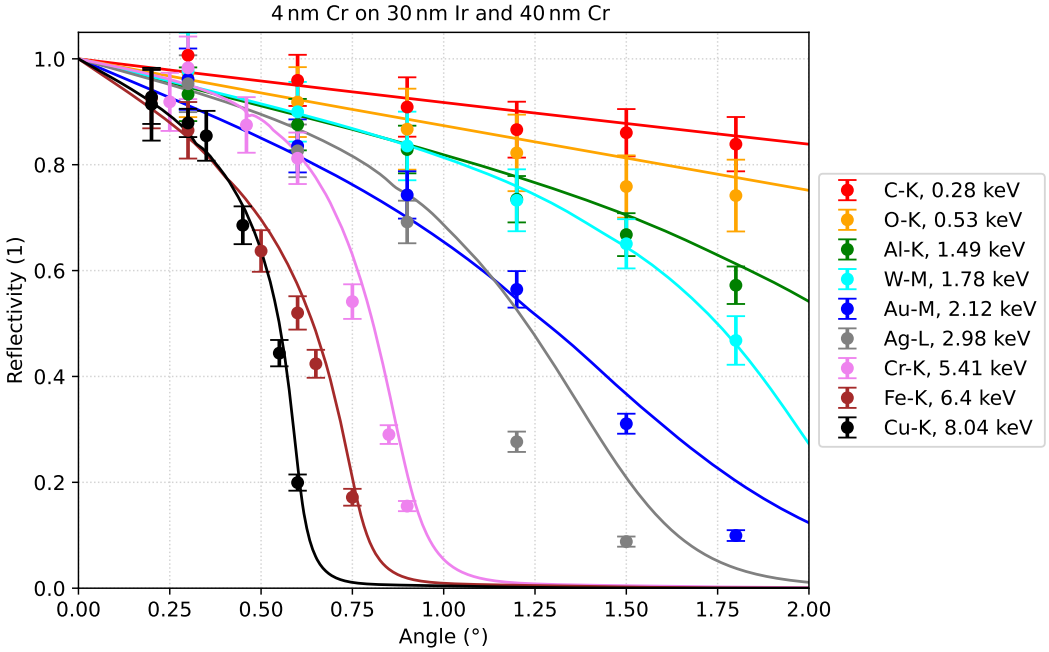


**Fig.** 7.4: Reflectivity measurement of sample with 4 nm Cr overlayer. Lines represent model predictions, same colour circles are measurement results with $3\,\sigma$ confidence interval.

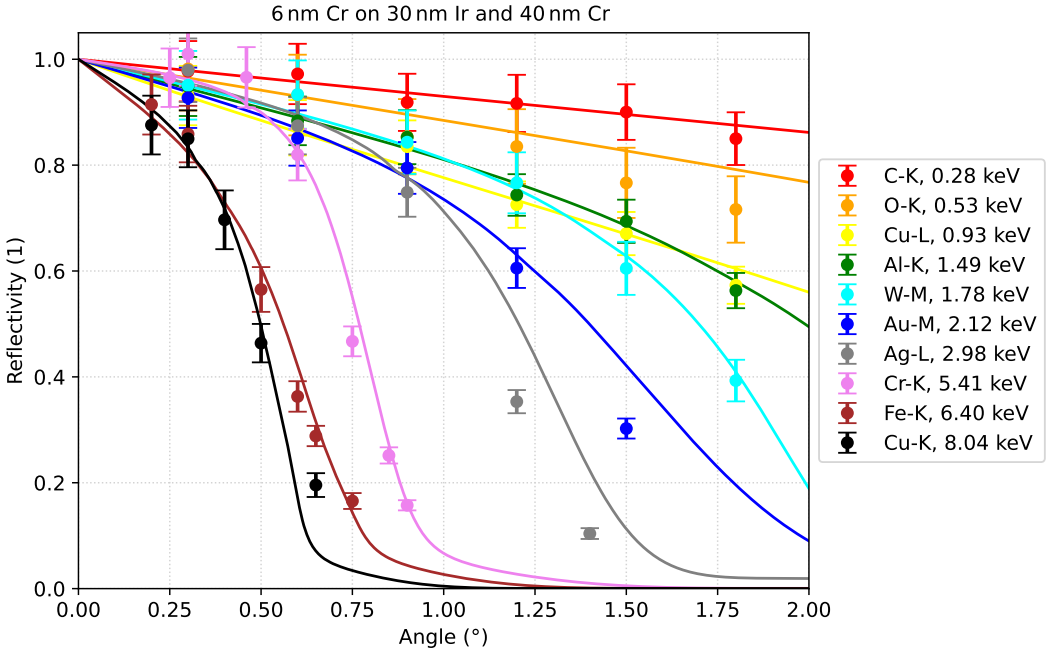


**Fig.** 7.5: Reflectivity measurement of sample with 6 nm Cr overlayer. Lines represent model predictions, same colour circles are measurement results with $3\,\sigma$ confidence interval.

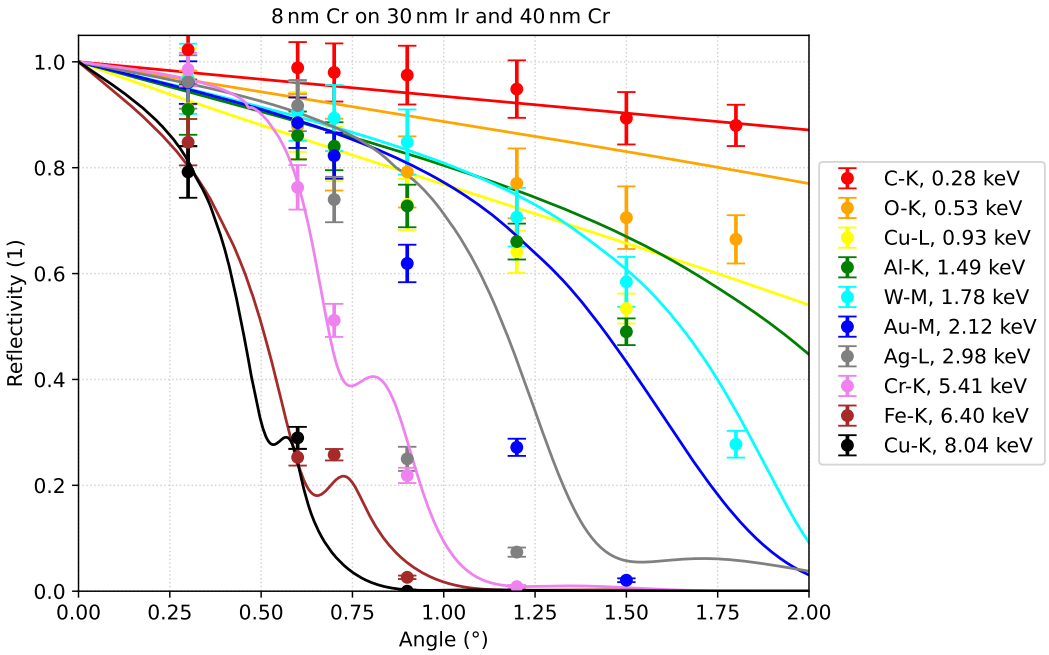


**Fig.** 7.6: Reflectivity measurement of sample with 8 nm Cr overlayer. Lines represent model predictions, same colour circles are measurement results with $3\,\sigma$ confidence interval.

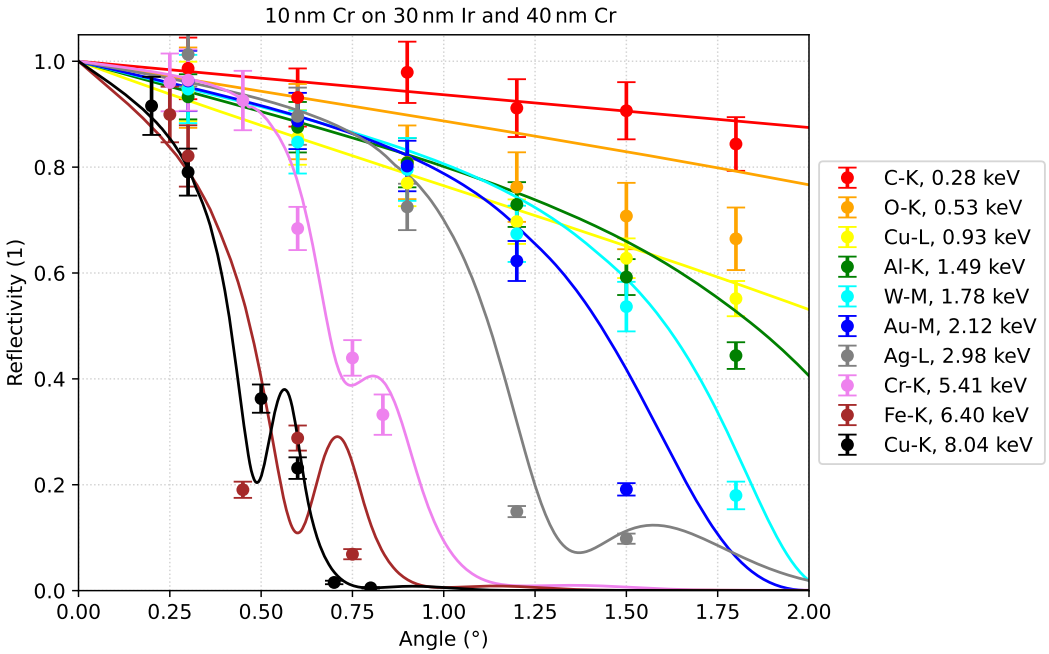


**Fig.** 7.7: Reflectivity measurement of sample with 10 nm Cr overlayer. Lines represent model predictions, same colour circles are measurement results with $3\,\sigma$ confidence interval.

## 7.5 Conclusion

The measurements mostly agree with the predictions, verifying the value of the model for designing reflective layers. The largest discrepancy is seen in the range of 2 keV - 3 keV, where the measurements show an earlier drop in reflectivity than predicted, with the difference being tens of standard deviations determined for the measurement result. These energies were covered with Ag-L, and Au-M lines. Compared to K-lines, which are closer to monochromatic radiation, the L and M lines have substructures, which can have distorting influence on the obtained results of measurement. The contribution of Bremsstrahlung can increase the distortion as well.

The properties of TRoPIC detector are another reason for observed behaviour. The energy resolution of TRoPIC is not infinite, and ranges from 60 eV at 0.5 keV to 160 eV at 8 keV. Combination of limited energetic resolution of the sensor and the substructures in L and M lines can lead to the discrepancy between the model and the results, as is seen in Figures in Chapter 7.4. Most influenced are then the areas, where the energy dependence of reflectivity in the corresponding range is strong. This areas are in particular at the chromium absorption edge around 0.6 keV and at the decrease at higher energies, where the limit of total reflection is reached.

The discrepancy in the relative reflectivity is lowest for a 10 nm surface layer of Cr. The simulations were done with the values for micro-roughness and thickness of the chromium-oxide according to the literature. Later performed TEM measurements showed, that the real thickness and oxidation depth can vary with respect to the original theory. The difference in the layer density and oxidation depth has, according to the simulations, significant influence on the reflectivity, and is the parameter potentially causing a mismatch with the PANTER results from this chapter. This motivates further studies on the effect of penetration in the multiple layers configuration. Alternatively it can be seen as hint that the surface quality is of importance and based on limited empiric measurements, was not modelled with enough precision.

At energies up to 1.8 keV and from 5.4 keV the angle and energy dependence is quantitatively well predicted by the model. The model accuracy is shown to be in principle sufficient for fine tuning layer parameters before manufacturing and testing.

# 8 Reflectivity measurement at BESSY II synchrotron

X-ray test of reflectivity at Panter facility showed that iridium coated mirrors with thin chromium overcoatings are performing in agreement with the simulation. As described in Chapter 5, test samples with different thicknesses of Cr overcoating had been studied, to evaluate the optimum coating for the lobster eye demonstrator. As the best option from the considered overcoating thicknesses - 10, 8, 6, or 4 nm - the variant with 6 nm of chromium on top was chosen. However, to avoid any doubts about the reliability and translatebility of the test results from glass to silicon substrate, another X-ray test was performed, this time using representative thin silicon wafer substrates. This time, instead of the PANTER facility, the BESSY II synchrotron was used. For my study, the most important difference between these two facilities is that BESSY II provides a much stronger photon flux over a wide range of energies.

This chapter contains a description of the BESSY II facility, the obtained measurement results, and their comparison with the theoretical reflectivity.

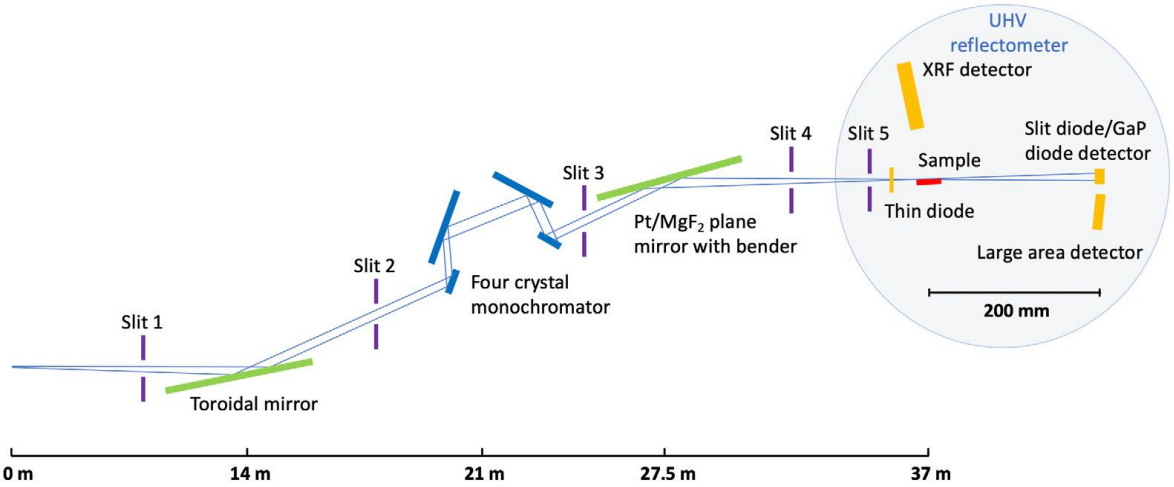


**Fig.** 8.1: The experimental setup for the reflectivity measurement at the PTB-FCM beamline at BESSY II [66].

## 8.1 Experimental setup of BESSY

The experimental characterisation of mirror sample was done at BESSY II in Berlin-Adlershof, in Physikalisch-Technische Bundesanstalt (PTB) laboratory.

The PTB is the national metrology institute in Germany and runs a laboratory with several beamlines at the synchrotron radiation facility BESSY II. The PTB laboratory covers the photon energy range from 1.75 keV to 11 keV. This is achieved using four Si(111) and four InSb(111) crystals, which can be interchanged under vacuum [67]. The beam line provides radiation of very high spectral purity, with higher order contamination typically below $10^{-4}$. Figure 8.1 shows the schematic set-up of the beamline. The detailed instrument data of the four-crystal monochromator beam line are summarised in table 8.1.

During the BESSY II test, the mirrors produced as described in section 5.4 were examined. These are thin mirrors using silicon substrate, as planned for the final demonstrator, so a step further from the technological samples used during Panter test in chapter 7.

The substrate was a semiconductor grade polished silicon wafer from Siegert Wafer GmbH. Dimensions of the wafer were 100 mm × 50 mm × 0.625 mm. Used is the tri-layer with 0.6 nm chromium overcoating.

Sample mirror was placed in an UHV reflectometer, providing 0.001° angular resolution for sample and detector [68]. Photodiodes with different apertures and a photon-counting large area detector are mounted on the detector arm. An additional GaP photodiode operating in transmission in front of the reflectometer is used for normalisation. This setup has already been used in the past to study the effect of low-density overcoats increasing the reflectivity [66, 69].

Measurements were performed for two grazing incident angles, 0.6° and 0.9°. The energy range was from 1.9 keV up to 11 keV. In this range, the measurement steps were:

- 5 eV from 1.90 keV to 2.30 keV
- 10 eV from 2.35 keV to 3.60 keV
- 5 eV from 3.65 keV to 11.00 keV

## 8.2 Measurement results

BESSY II measurement results were compared with previously done simulations. Simulated reflectivity was performed using the parameters of mirrors obtained during previous measurements - surface microroughness, layer density and layer thickness, including the surface oxidation layer influence. Simulations were done for six different grazing angles with a step size of 0.3°, and for the energy range 0.1 keV - 10 keV with 20 eV steps. Synchrotron measurements were not performed at all simulated grazing

**Tab.** 8.1: BESSY II PTB-FCM beamline: instrument data [67, 70]

| | |
|---|---|
| Source | B II dipole |
| Monochromator type | Four-crystal monochromator |
| Monochromator crystals | CSi(111) and InSb(111) |
| Energy range | 1.75 keV to 11 keV |
| Energy resolution | $< 1$ eV |
| Spectral resolving power | $\approx 10^4$ |
| Flux | $10^{11}\,\mathrm{s}^{-1}$ |
| Polarisation | Horizontal |
| Focus size | 0.3 mm × 0.3 mm |
| Fixed end station | X-ray reflectometer |

angles, but for the diagnostically conclusive angles at 0.6° and 0.9°, and in the energy range 1.9 - 11.0 keV.

All the simulation curves together with the BESSY II measurement values are plotted in Figure 8.2. Details of the Ir absorption edge can be seen in Figure 8.3.

The measurement results agree very well with the theoretical values. It is worth noting that the predicted drop in reflectivity in the Ir-M lines region (2040 eV) is slightly deeper than the gained values. The measurements at BESSY II were in this area done with a 5 eV step. The energetic gap in simulations covers about 100 eV. With the ratio of a single step and the expected range of the drop in reflectivity 1:20, these results suggest that the reflectivity of prepared overcoatings is better then of the model. The measured increase of the reflectivity was between 5 and 10 % over the predicted reduced-reflectivity area. From result combination of PANTER and BESSY II measurement, one can conclude that the mirrors have proven their superior reflectivity in region of incident energy up to 5 keV over the golden mirrors, and exceed the expectations based on models which used empirical data.

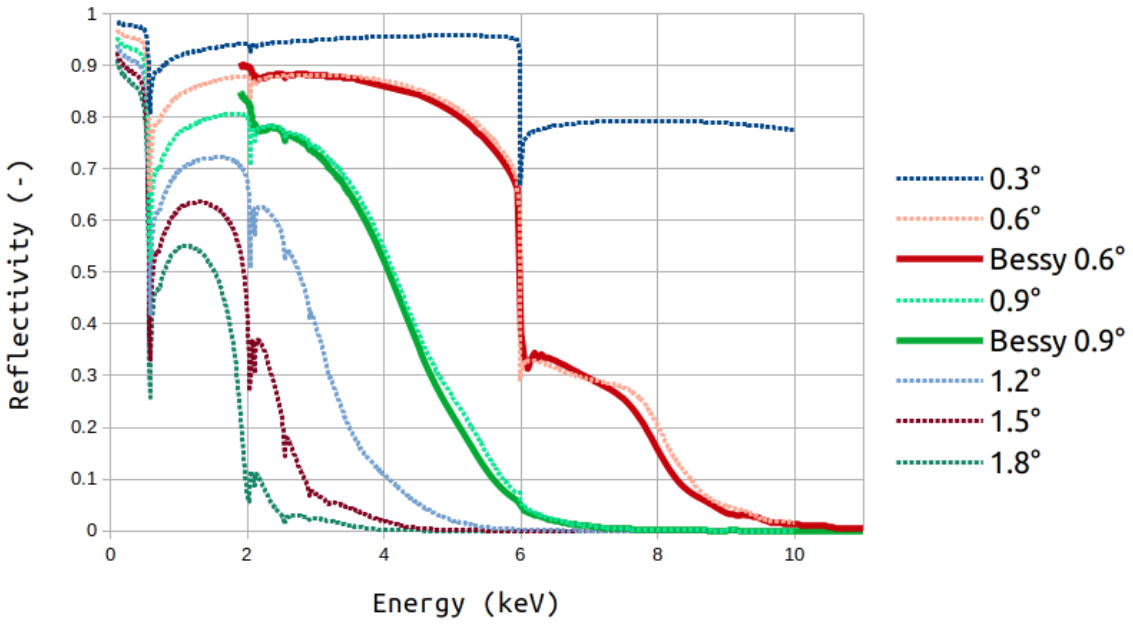


**Fig.** 8.2: Comparison of simulated values at different angles and measured values at BESSY II. Used was and silicon mirror with Cr/Ir sandwich and 6 nm thick overlayer, as manufactured for HORUS experimental optics. Simulations were done with steps of 20 eV. BESSY II measurements were done in steps of 5 eV from 1.9 keV to 2.3 keV, then in 10 eV steps up to 3.6 keV, and finally again in 5 eV steps for 3.65 - 11 keV range. [70]

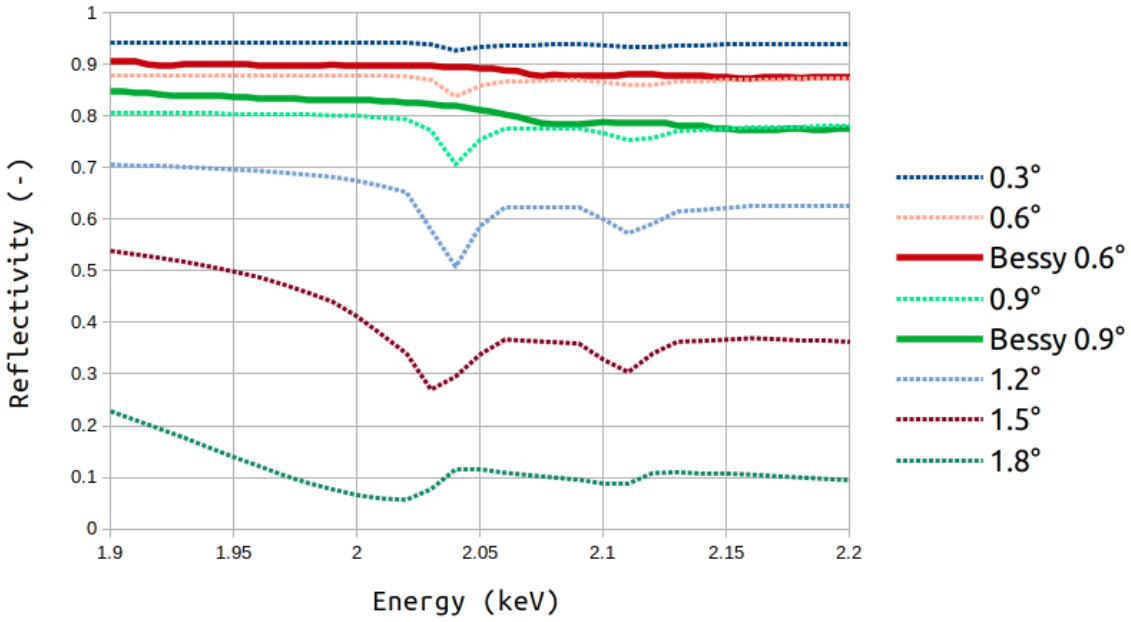


**Fig.** 8.3: Comparison of simulated values at different angles and measured values at BESSY II. Used was and silicon mirror with Cr/Ir sandwich and 6 nm thick overlayer, as manufactured for HORUS experimental optics. Simulations were done with steps of 20 eV. Presented is the region around Ir-M absorption edge, where the BESSY II measurements were done in steps of 5 eV. A detail for comparison with the overview Figure 8.2. [70]

# 9 X-ray testing of built optic demonstrator

After manufacturing the experimental 4-unit demonstrator equipped with two different reflective layers, another testing at the PANTER facility in Neuried followed. These tests were supposed to bring two basic groups of data and results - regarding the arrangement and regarding the type of reflective layers. According to the measurement target, the test campaign was divided into two parts - HORUS I and HORUS II. Between them, the facility had to be vented and opened, to make the reconfiguration of the modules possible. The following pumping down to operational vacuum then typically lasts over weekend, thus careful planning is required.

During the first set of measurements, the modules were divided according to the coating material. The two units with gold coated mirrors were set in an off-axis-focusing Schmidt's arrangement. In the following text, I am naming it GCM (gold-coated module). The units with iridium-chromium coated mirrors were set in the same way. Used name tag is ICM (iridium-coated module). These two independent optics then went through similar sets of measurements. This way, we obtained a direct comparison of gold and iridium-chromium coated optics.

During the second part of the campaign, all four units were stacked in logical order according to their focal length. In this configuration, they simulated a hybrid between lobster eye in Schmidt's arrangement and Kirkpatrick-Baez optic, as described in Chapter 3. Detailed description is given in Chapter 9.2.

Following chapters describe all the performed measurements and show the results we obtained.

## 9.1 HORUS I X-ray experiment

Horus I test campaign at PANTER ran for 11 days. Its objective was to quantify the quality difference between two modules, which have almost identical design - same structure, number of mirrors and were hand-built the same way, only their focal length is different for 10 cm (195 cm for GCM, 205 cm for ICM). The main difference between them is in the material of mirrors' reflective coatings. This section describes the experimental set-up, the course of the campaign, and the results we obtained.

### 9.1.1 Experimental set-up

The mechanical setup of PANTER testing facility was adapted to the measurement purpose. It includes several instruments in following configuration:

- X-ray radiation source with aperture of 315 mm at the optic
- Optical mask illuminating
  - whole optical module, 84 to 84 mm square
  - single horizontal mirror, a slit 84 to 3 mm
  - single vertical mirror, a slit 3 to 84 mm
- Two optical modules mounted side by side on a tip-tilt (Optic Pitch - Optic Yaw) manipulator
- TRoPIC detector

In Figure 9.1 one can see both modules from the direction of detector. Figure 9.2 then shows the optical mask, as mounted in the mouth of vacuum tunnel. During the tests described in Chapter 7, the mask was only a thin slit. In case of HORUS set-ups, the mask was divided into three parts. For measurements from the whole aperture of optical modules, there is a square opening of dimensions 84 to 84 mm. For measurements of single mirrors in both vertical and horizontal orientation are slits of dimensions 84 to 3 mm were used. With given spacing between mirrors, this slit size made it possible to illuminate only one mirror in its whole width. For the single-mirror measurements was always used the horizontal middle mirror, no. 9.

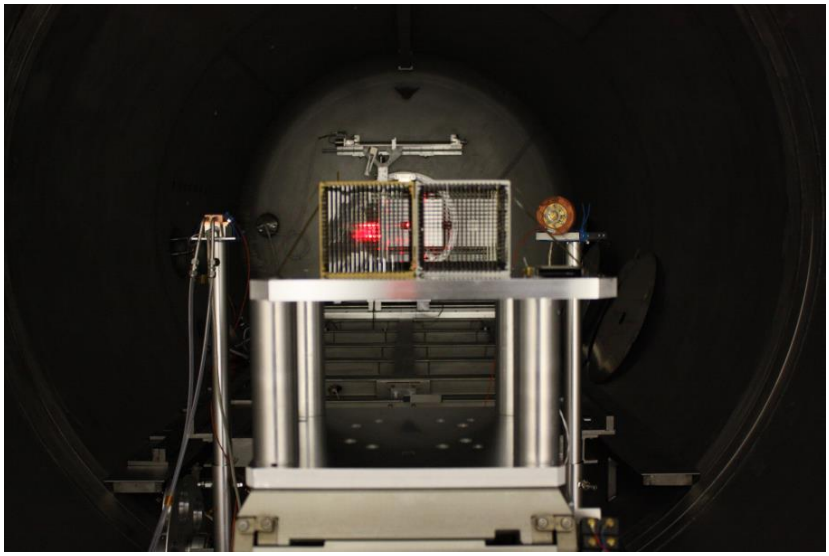

**Fig.** 9.1: Both optical modules mounted on tip-tilt manipulator. View from detector towards X-ray source. In the picture on the left is the module with iridium coated mirrors (ICM), on the right the gold coated one (GCM). Red laser beam, which was used for alignment in air, shines through the iridium-coated module.

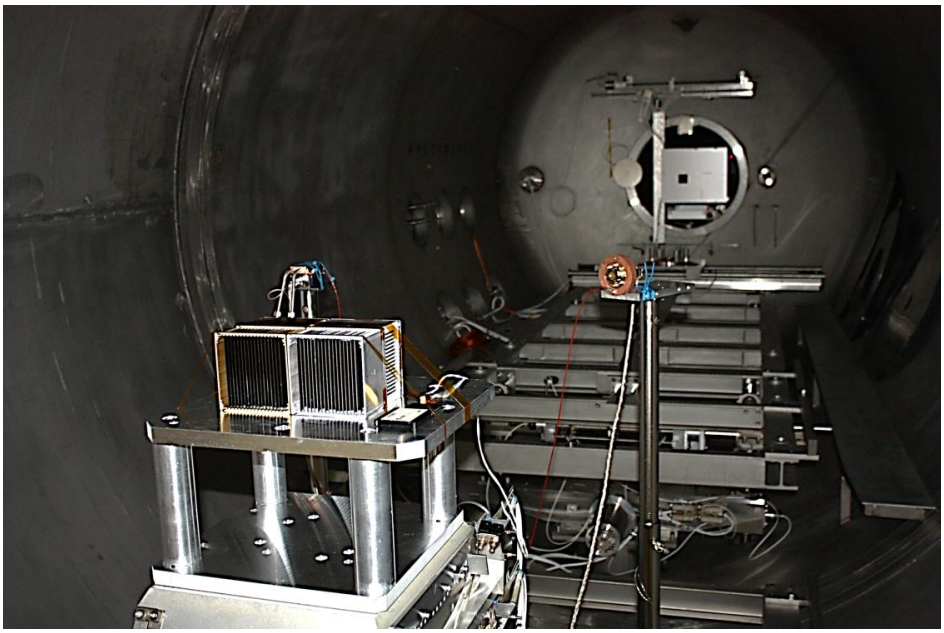

**Fig.** 9.2: Both mirror modules are mounted on manipulator. From afar can be seen the entrance to the test chamber from the vacuum tunnel, with mask placed in it. In the middle is standing QCM (contamination check).

The measurement described in this chapter uses only the Al-K line for calibration and testing, and in addition the low energy band continuum. This choice is based on the measurements from Chapter 7 , which established the efficiently reflected energy range, based on 10 distinct element lines.

The Al-K line belongs into the softer X-ray area, which was our primary interest while designing the Cr-Ir layers. Used source is an Al target with Al 10 µm filter. The low energy band continuum provides energies in the range 700 - 4000 eV. Also Ti-L (452 eV) and W-M (1780 eV) lines are visible. Continuum source is a Ti target, with Ti 1 µm NLT filter.

The measurement started with Al-K line, which was used for first light image and alignment in X-rays. Afterwards were done the experiments in low energy band continuum.

### 9.1.2 Measurement methods

During the HORUS I measurement campaign, the following measurement methods and formulas were applied. Detailed list of the steps and angles can be found in Tables 9.1 and 9.2. Discussed methods were used for all the measurements, and their usage is not repeatedly reminded at every measurement result.

- Focus Search
  - at Al-K line
  - modules were moved along the axe source - detector in 20 mm steps

  - FWHM used as the focus search metric; calculated by fitting a 2D Gaussian profile to the PSF images
  - best fit taken as best focus position
- On-Axis Extended 'Mosaic' PSF
  - extended PSF image made at each energy to characterise the extended arms of the on-axis PSF
  - 5x5 TRoPIC scan of the on-axis in focus PSF
  - combining all 25 images into a mosaic, with dimensions $25 \times 18.6 \times 18.6\,\mathrm{mm}^2$, i.e. $86.5\,\mathrm{cm}^2$
- Single reflection branches, horizontal and vertical
  - measurements at best focus position
  - yaw angle changing to 1.0°, 1.6°, and 2.0°. Pitch stays in best position
  - measuring of single mirror no. 9 taken at various angles
  - extreme intrafocal position measured
- Flat fields
  - a flat field exposure taken before and after each measurement set
  - serve as a reference for the X-ray beam variations
  - TRoPIC remains in the on-axis, in-focus position; optics moves out of the beam
  - best fit taken as best focus position
- Effective area
  - calculated for each energy using the focus search measurements and/or the focal plane mapping measurements
  - obtained values are corrected using the corresponding flat field exposures for each measurement set
  - $A_{eff}$ was calculated using Equation 9.1, where $C_{optic}$ is the count rate from the optic, $C_{FF}$ is the flat field count rate, $A_{det}$ is the collecting area of the TRoPIC detector (3.542 $\mathrm{cm}^2$), and $G$ is the geometrical correction for the divergent X-ray beam.

$$A_{eff} = \frac{C_{optic}}{C_{FF}} \cdot A_{det} \cdot G \tag{9.1}$$

  - geometrical correction for this campaign is $G = 0.972$, calculated using Equation 9.2, where $d_{source-optic}$ is the distance between the X-ray source and the optic and $d_{source-focalplane}$ is the distance between the source and the focal plane. The effective area is measured at the intrafocal distance $d_{intrafocal}$. Therefore, the distance between the source and the detector is $d_{source-focalplane} + d_{intrafocal}$.

$$G = \left( \frac{d_{source-optic}}{d_{source-optic} + d_{intrafocal}} \right)^2 \tag{9.2}$$

  - $1\sigma$ relative statistical error is calculated for each exposure, using the number of counts in the region of interest on the detector
  - this error is propagated through the above calculation to give a $1\sigma$ error on the effective area value of each exposure
- Beam stability monitoring
  - linked to the flat field and effective area measurements
  - overview how much the count rate of the X-ray beam at given energy fluctuates over a specific measurement period

### 9.1.3 Measurement sequence

Complete overview of planned and performed measurements at Al-K line is listed in Table 9.1. The plan for measurement in low energy band continuum (lEBc) can be seen in Table 9.2. For both ICM and GCM the test plan was similar to have data for direct comparison. At Al-K, effective area scans for different angles were made and compared. In low energy band continuum, besides effective area scans at different angles, were single-mirror scans done as well. In the end, panoramic optic mapping of both modules without any mask in lEBc closed the HORUS I testing.

**Tab.** 9.1: HORUS I PANTER X-ray test: used element lines, corresponding energy, wavelength, and incident angles.

| **Type of operation** | **Element line** | **Energy (keV)** |
|---|---|---|
| Alignment steps | Al-K | 1.49 |
| Effective area scans ICM at 1.0° | Al-K | 1.49 |
| Effective area scans ICM at 1.6° | Al-K | 1.49 |
| Effective area scans ICM at 2.2° | Al-K | 1.49 |
| Effective area scans ICM at 1.6°<br>Extreme intra-focal, -467 mm | Al-K | 1.49 |
| GCM - alignment, focal scan, 5 to 5 mosaic | Al-K | 1.49 |
| GCM effective area at 1.0°<br>- double reflection<br>- horizontal reflection<br>- vertical reflection | Al-K | 1.49 |
| GCM effective area at 1.6°<br>- double reflection<br>- horizontal reflection<br>- vertical reflection | Al-K | 1.49 |
| GCM extreme intrafocal scans at 1.6°<br>- double reflection<br>- horizontal reflection<br>- vertical reflection | Al-K | 1.49 |
| GCM effective area at 2.2°<br>- double reflection<br>- horizontal reflection<br>- vertical reflection | Al-K | 1.49 |
| ICM extreme intrafocal scan at 1.6°<br>- double reflection | Al-K | 1.49 |

**Tab.** 9.2: HORUS I PANTER X-ray test: low energy band continuum used, with visible Ti and W element lines.

| **Type of operation** | **Element line** | **Energy (keV)** |
|---|---|---|
| Setup for continuum measurement | Ti-L, W-M | 0.7 - 4 |
| Effective area scans ICM at 1.0°<br>- double reflection<br>- horizontal reflection<br>- vertical reflection | Ti-L, W-M | 0.7 - 4 |
| Effective area scans GCM at 1.0°<br>- double reflection<br>- horizontal reflection<br>- vertical reflection | Ti-L, W-M | 0.7 - 4 |
| Effective area scans ICM at 1.6°<br>- double reflection | Ti-L, W-M | 0.7 - 4 |
| Effective area scans GCM at 1.6°<br>- double reflection | Ti-L, W-M | 0.7 - 4 |
| Effective area - mirror no. 9, horizontal<br>- 0.6°<br>- single reflection<br>- 0.9°<br>- single reflection | Ti-L, W-M | 0.7 - 4 |
| Effective area scans ICM for single mirror<br>- single reflection 1.2°<br>- single reflection 1.5°<br>- single reflection 1.8°<br>- single reflection 2.4° | Ti-L, W-M | 0.7 - 4 |
| Effective area scans ICM at 2.2°<br>- double reflection | Ti-L, W-M | 0.7 - 4 |
| Effective area scans GCM at 2.2°<br>- double reflection | Ti-L, W-M | 0.7 - 4 |
| Effective area of single mirror,<br>ICM scan at 1.5°<br>- single reflection | Ti-L, W-M | 0.7 - 4 |
| Effective area of single mirror,<br>GCM scan at 1.2°<br>- single reflection | Ti-L, W-M | 0.7 - 4 |
| Mosaic 5 to 5 ICM at 0°, 0.6°,2.4° | Ti-L, W-M | 0.7 - 4 |
| 5 to 1 mapping of GCM at 1.5°, single mirror | Ti-L, W-M | 0.7 - 4 |
| 16 to 8 mapping of ICM and GCM at 0° | Ti-L, W-M | 0.7 - 4 |

### 9.1.4 Laser alignment

As the first step before closing the vacuum chamber and pumping the facility down, the optics were aligned in normal atmosphere using a laser beam. The laser source was placed in the same position as is the X-ray source. First was aligned ICM, then GCM at 0° angle. Because both optics have mirrors coated only on one side and are designed as out-of-axis, followed alignment at the operational angle. 2.3° angle was introduced, to reach the expected 160 mm distance from the geometrical axis to the optical axis. The average of the two nominal focal lengths was used to set the distance of the focal plane image. This is needed to ensure the individual modules can be brought to their respective focal distance with the limited movement range of the detector. A photo from the laser alignment under 2.3° angle can be seen in Fig. 9.3.

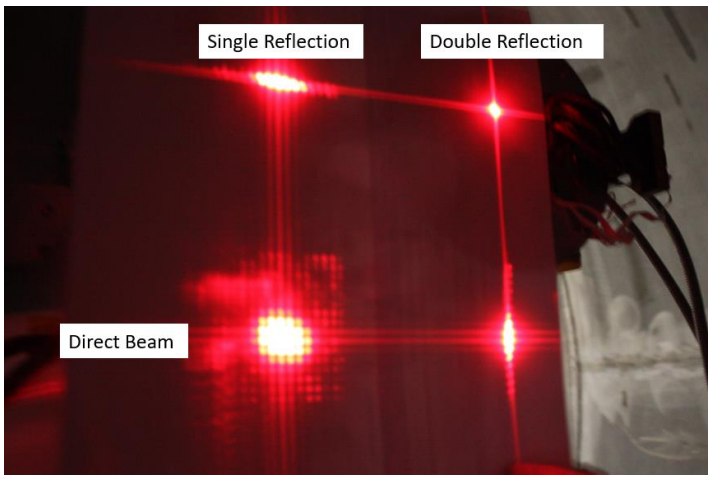


**Fig.** 9.3: Focal plane image during the laser beam alignment. The optic is rotated by 2.3° in yaw and pitch. Direct beam through the optic, horizontal and vertical single reflections, and focal point (double reflection) are marked.

### 9.1.5 X-ray alignment and focus search

After a rough focal alignment using laser beam, the vacuum chamber was closed and pumped down. TRoPIC detector and X-ray source were switched on. For the X-ray alignment, Al-K line was used - the source was an aluminium target, with 10 µm aluminium filter. As starting point for alignment, the individual estimates of the laser alignment were chosen. As the resulting image was obviously out of focus, the detector was re-positioned by eye, to achieve a semi-focused image.

This correction was expected to be needed, because there is always a slight difference between focal length in visible light and in X-rays. Including this shift the detector was

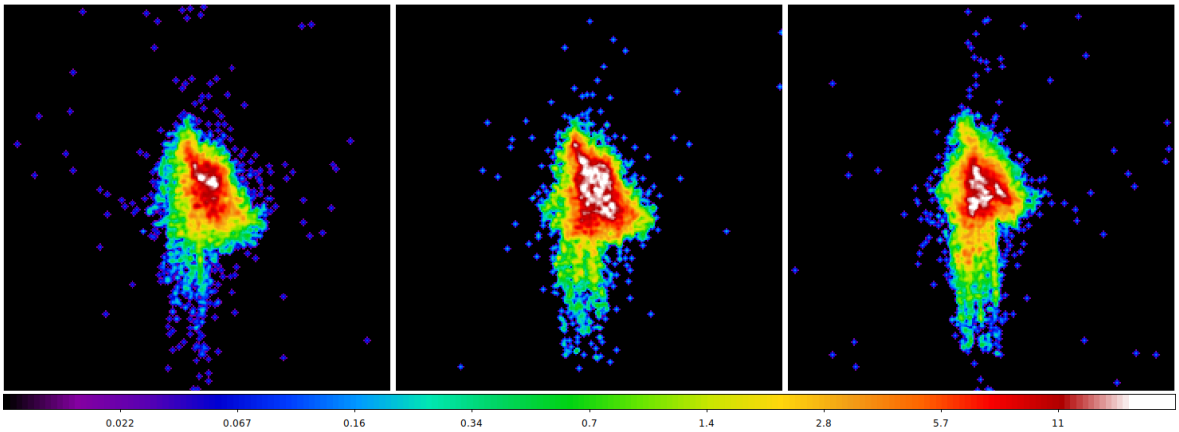


**Fig.** 9.4: The double reflection spots of the ICM at Al-K line. From left to right at 1.0°, 1.6° and 2.2° angles.

still able to reach both focal points, emphasising the importance of the pre-alignment.

With rough focus set, mask alignment was done. The mask was set for all three cases - horizontal and vertical slit to perform measurement on single mirror, and a full-aperture for measuring whole module.

After setting the coordinates for mask positions, fine focus search followed, first for ICM, then for GCM. This was done again with the same Al source settings. Optics position along the optical axis was changed in 20 mm steps. The exposure time for each position was 300 seconds. FWHM of double-reflection point was used in a regression to determine the best focal distance, which is then used for the following measurements. The details of the focus search are presented in the Appendix B.

### 9.1.6 Comparison of reflectivity for ICM and GCM

In following figures can be seen an overview of measurement results. At first, the shape of focal point of both ICM and GCM in the best focus, as a double reflection at different angles. Then the figures of effective area measurement for both full modules measurements and for one mirror measurement only.

Figures 9.4 and 9.5 show ICM and GCM double reflection spots respectively, at the Al-K line for angles at 1.0°, 1.6° and 2.2°. Figures 9.6 and 9.7 show the same comparison for the lEBc.

It follow three figures comparing the effective area at the double reflection for both modules at 1.0° (9.8), 1.6° (9.9) and 2.2° (9.10).

Figures 9.11 and 9.12 show the effective area for a single plate (the ninth) in the the ICM and GCM module respectively, at five different angles.

The final Figure 9.13 is a panorama image of both modules in lEBc.

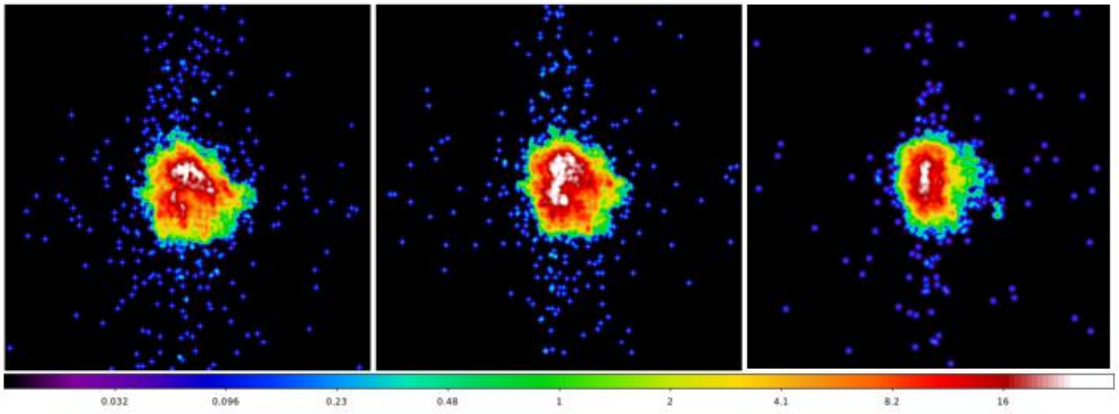


**Fig.** 9.5: The double reflection spots of the GCM at Al-K line. From left to right at 1.0°, 1.6° and 2.2° angles.

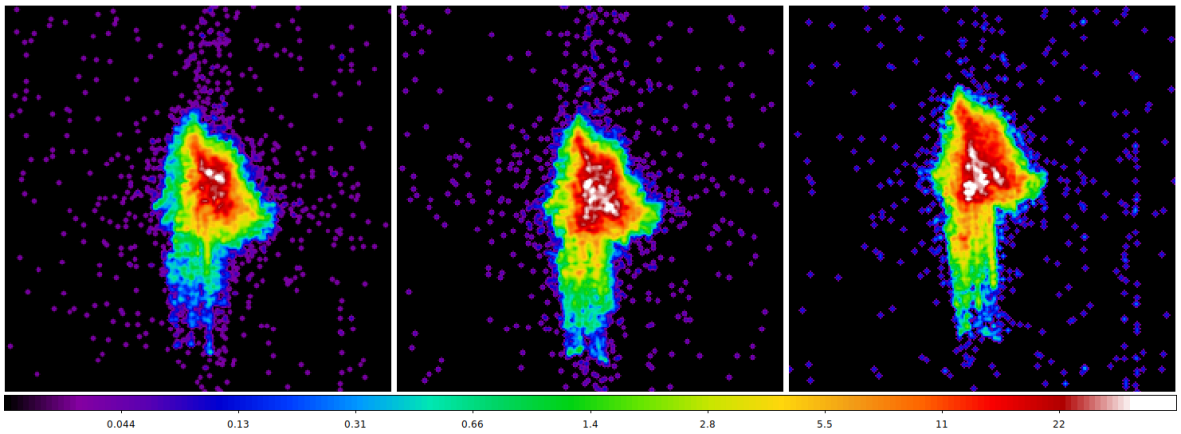


**Fig.** 9.6: The double reflection spots of the ICM at low energy band continuum. From left to right at 1.0°, 1.6° and 2.2° angles.

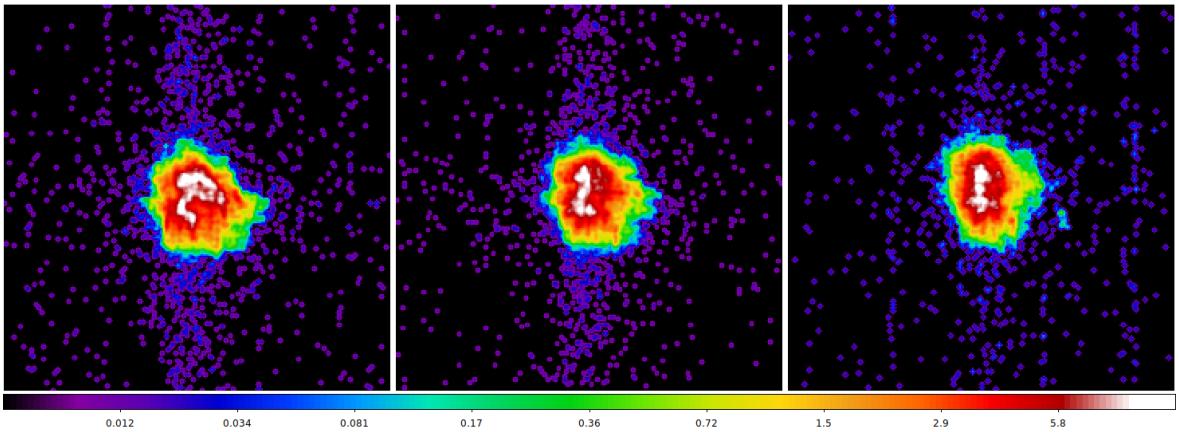


**Fig.** 9.7: The double reflection spots of the GCM at low energy band continuum. From left to right at 1.0°, 1.6° and 2.2° angles.

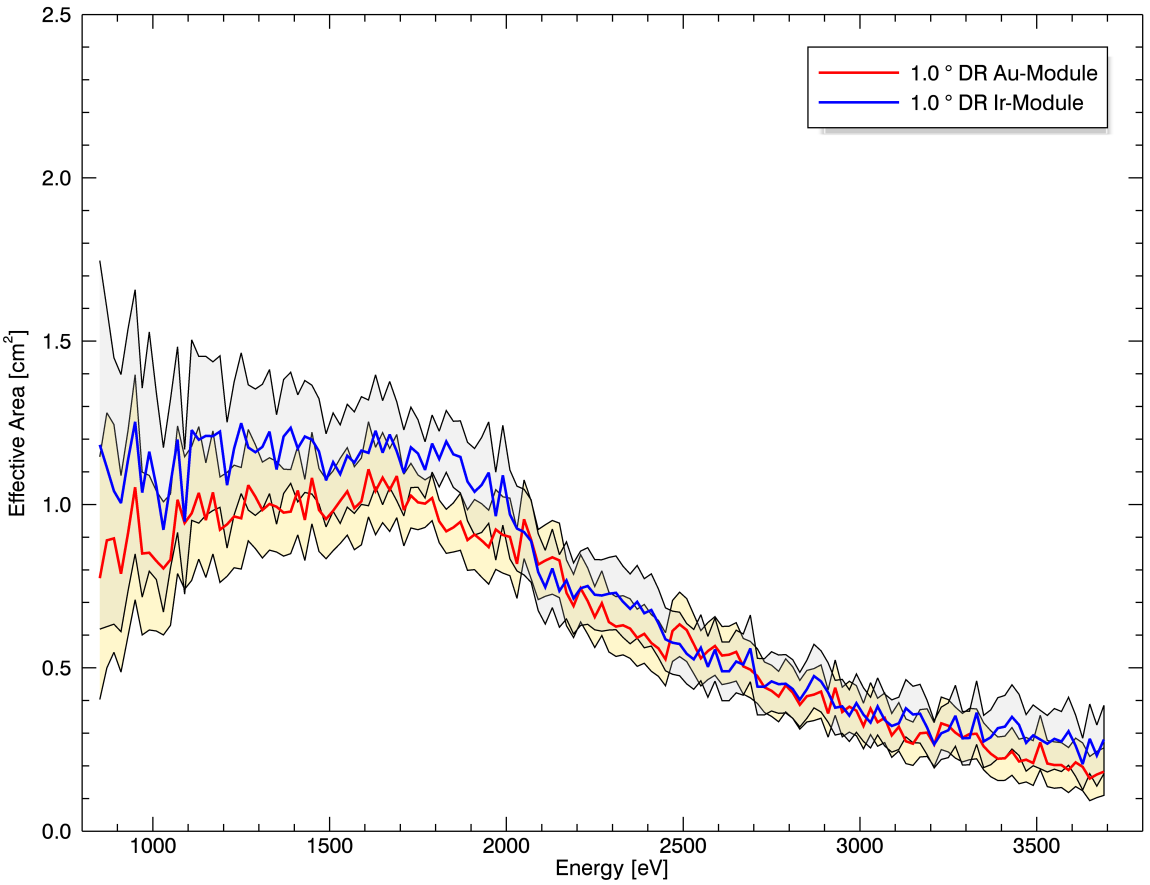


**Fig.** 9.8: Comparison of effective area at the double reflection spot of ICM and GCM at 1.0°. Shaded areas represent $3\sigma$ confidence intervals.

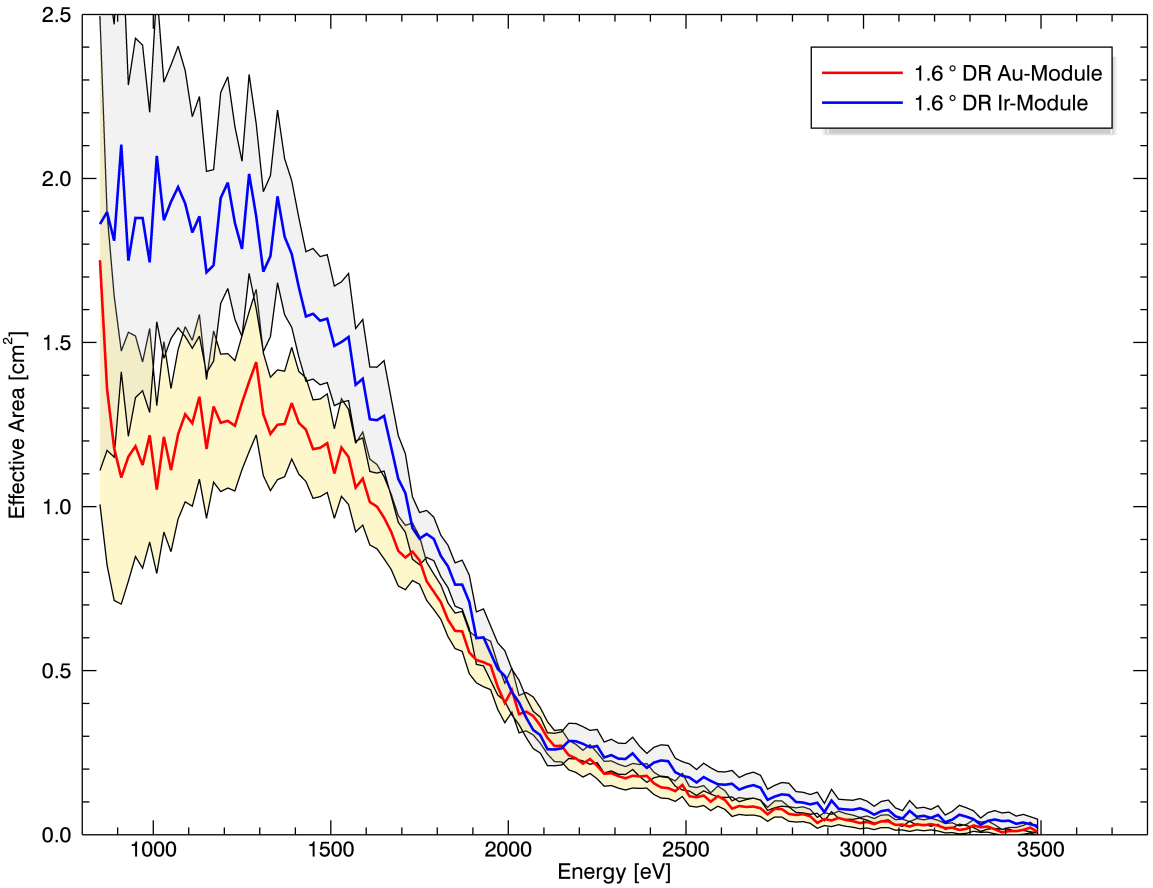


**Fig.** 9.9: Comparison of effective area at the double reflection spot of ICM and GCM at 1.6°. Shaded areas represent $3\sigma$ confidence intervals.

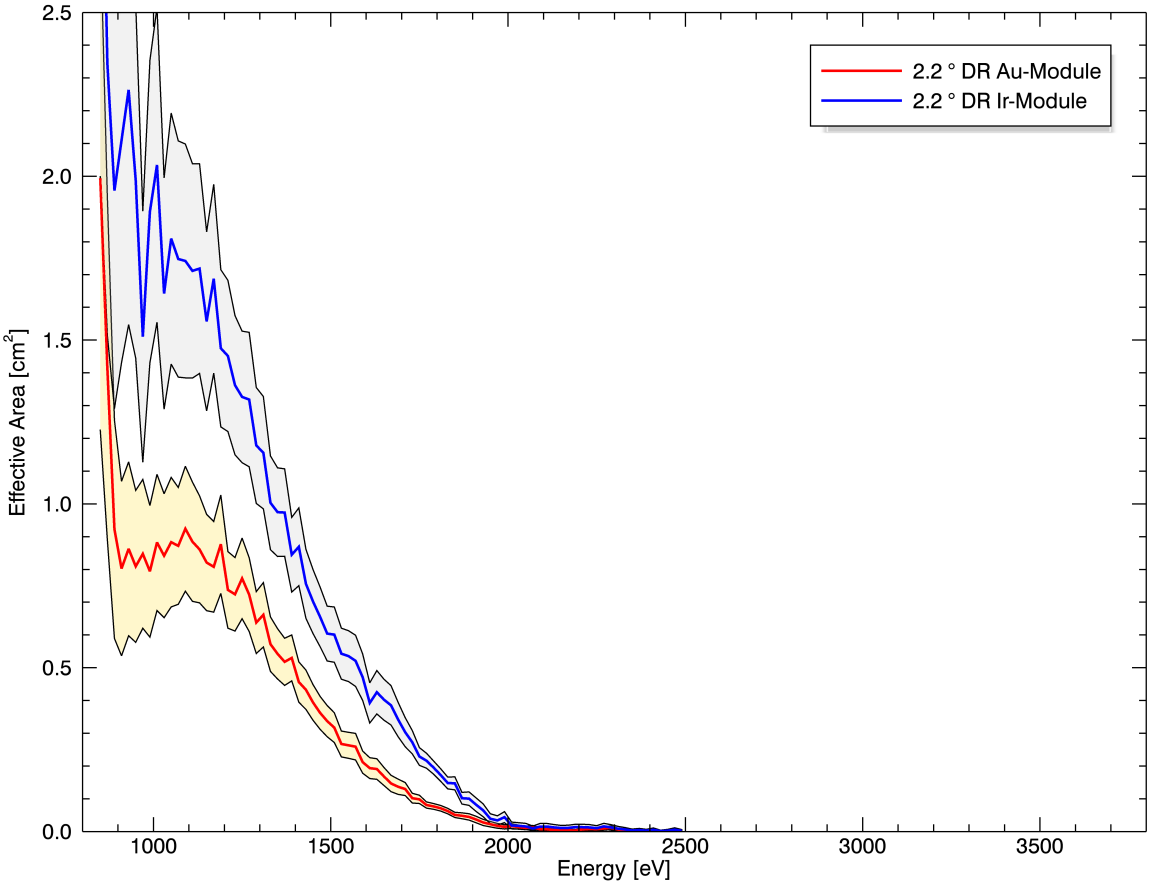


**Fig.** 9.10: Comparison of effective area at the double reflection spot of ICM and GCM at 2.2°. Shaded areas represent $3\sigma$ confidence intervals.

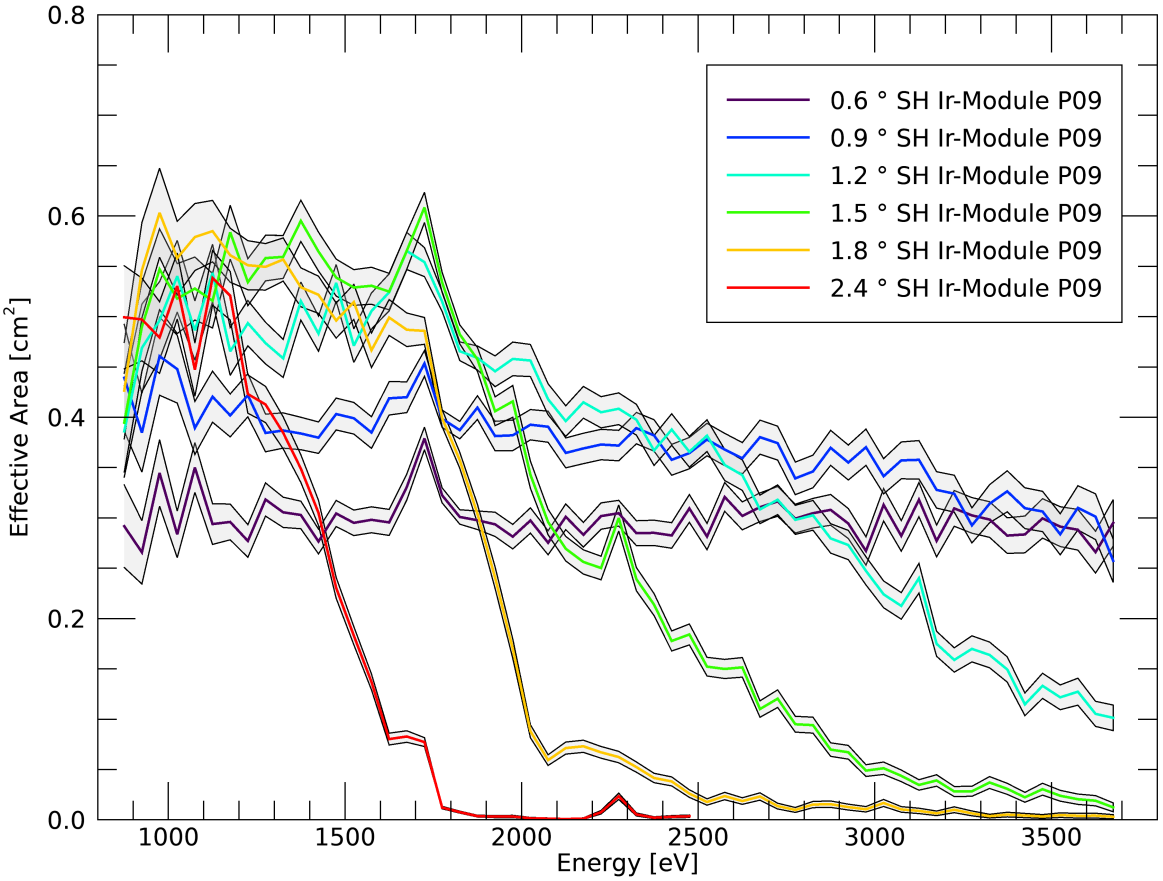


**Fig.** 9.11: Comparison of effective area measurement of ICM plate no.09 in the lEBc. Shaded areas represent $1\sigma$ confidence intervals.

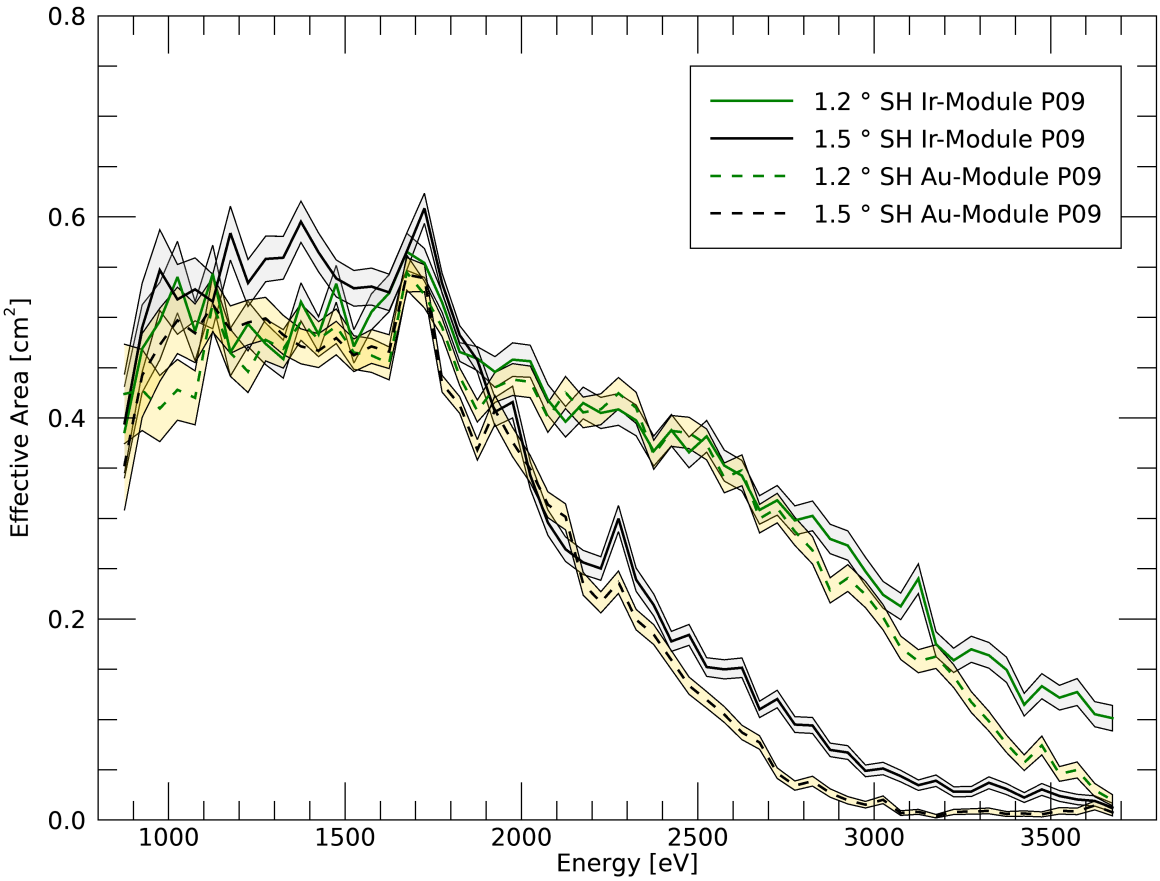


**Fig.** 9.12: Comparison of effective area measurements of ICM and GCM plates no.09 at 1.2 and 1.5° in the lEBc. Shaded areas represent $1\sigma$ confidence intervals.

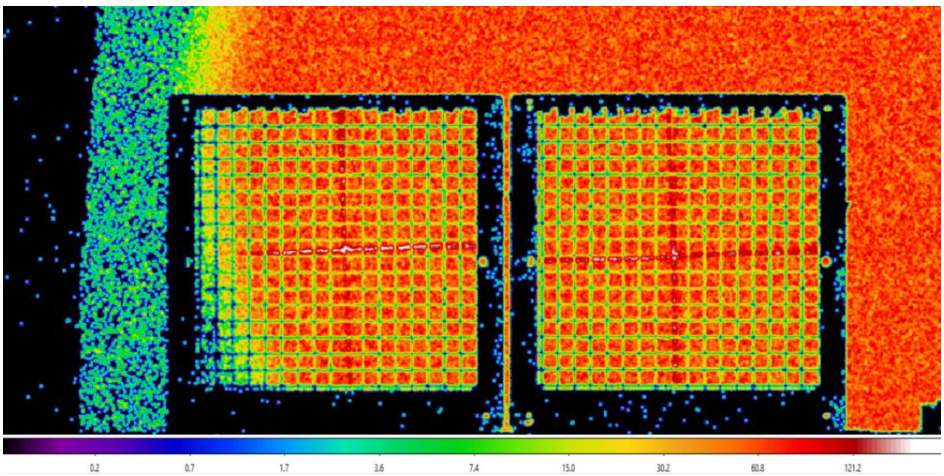

**Fig.** 9.13: Panorama image of both modules in lEBc.

### 9.1.7 Conclusion

Optical performance of two modules with similar design and two different coatings was measured and compared. The theoretical prediction from Chapter 4 and also first tests on individual mirror samples in Chapter 7 indicated a better performance of Cr-Ir compared to pure Au, especially up to 5 keV. The presented HORUS I campaign confirmed the expectation in the energy range from 0.8 keV to 4 keV, for angles in the range of 1.0° to 2.2°. The effective area is increased by about 20-30% in the low energy band continuum.

The PSF of the focal point for both modules was evaluated as well. For the chromium-iridium coated module, the obtained FWHM value was 5.5 arcmin at 1° incident angle. For the gold coated module, the value was comparable, 5.2 arcmin at 1°.

## 9.2 HORUS II X-ray experiment

Horus II test campaign ran for 8 days. Its objective was to quantify the imaging capability of hybrid between lobster eye in Schmidt's arrangement and Kirkpatrick-Baez optic. This optic consists of four sub-modules in a row, two oriented vertically and two horizontally. GCM modules are oriented horizontally, and because of their longer focal length positioned further from the TRoPIC detector. ICM modules are oriented vertically, and closer to the TRoPIC detector. This section describes the experimental set-up, the course of the campaign, and the results we obtained.

### 9.2.1 Experimental set-up and alignment

The mechanical setup of PANTER testing facility was fitted for the measurement purpose. It includes several instruments in following configuration:

- X-ray radiation source with aperture of 315 mm at the optic
- Optical mask illuminating
  - whole optical module, a square of 84 mm to 84 mm
  - single horizontal mirror, a slid of 84 mm to 3 mm
  - single vertical mirror, a slid of 3 mm to 84 mm
- Hybrid optical module mounted on a tip-tilt (setting Optic Pitch and Optic Yaw) manipulator
- TRoPIC detector

In Figure 9.14 one can see the optical module on the manipulator from the direction of the detector. The optical mask is mounted in the place where the vacuum tunnel enters the measurement chamber. The QCM (Quartz Crystal Microbalance) sensor is on the stand on the right. HORUS II optics can be tilted in pitch and yaw to change the incidence angle, and moved between X-ray source and detector for fine focus search.

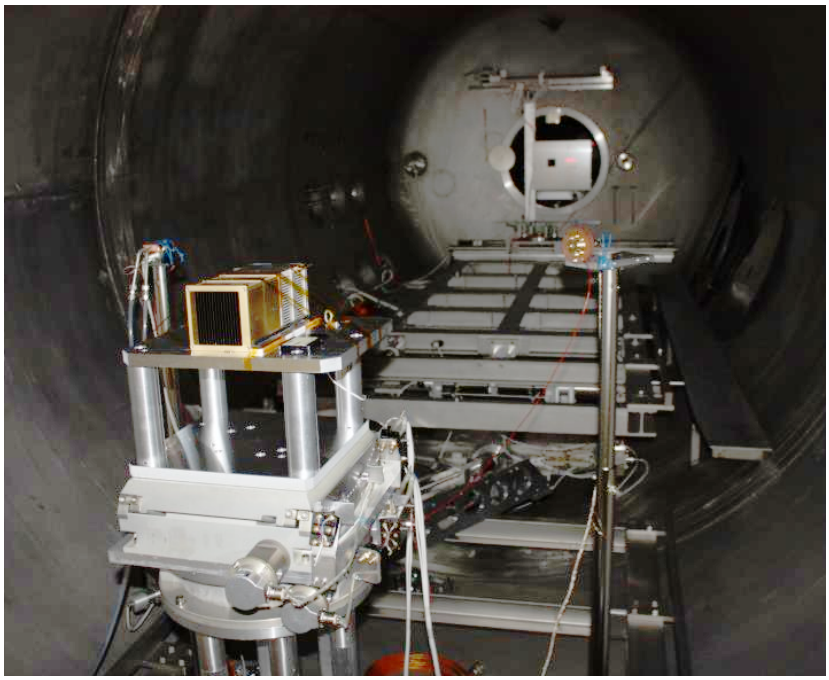

**Fig.** 9.14: HORUS II in vacuum chamber. On the right at the beginning of the vacuum tunnel can be seen the mask, closer the QCM on its mount.

### 9.2.2 Measurement methods

Measurement methods used during HORUS II test campaign were almost the same as during HORUS I tests. The list of measurement methods and formulas can be found in subsection 9.1.2. The only difference is added Off-axis 'corner' measurement. This off-axis, in-focus measurement was done using low energy band continuum (lEBc). The intensity of direct beam, coming through the optic at different angles, was measured. Exposure for these measurements was always approximately 300 s.

### 9.2.3 Measurement sequence

The complete 8-day test plan can be seen in Table 9.3. The steps of the plan are showing the angles, which were used for experiments, as well as their combinations with different wavelengths. 9.1.2

**Tab.** 9.3: HORUS II X-ray test: used element lines, corresponding energy, wavelength, and incident angles.

| **Type of operation** | **Element line** | **Energy (keV)** |
|---|---|---|
| Alignment steps | Al-K | 1.49 |
| Mosaic 7 x 6 at 0° | Al-K | 1.49 |
| Mosaic 6 x 6 at 0.6° | lEBc | 0.8 - 4 |
| Mocaic 5 x 5 at 1.2° | lEBc | 0.8 - 4 |
| Mocaic 5 x 5 at 1.8° | lEBc | 0.8 - 4 |
| Effective area scans at 1.0°<br>- double reflection<br>- horizontal reflection<br>- vertical reflection | lEBc | 0.8 - 4 |
| Effective area double reflection at 2.4 ° | lEBc | 0.8 - 4 |
| Effective area double reflection at 2.2 ° | lEBc | 0.8 - 4 |
| Effective area double reflection at 2.0 ° | lEBc | 0.8 - 4 |
| Effective area double reflection at 1.8 ° | lEBc | 0.8 - 4 |
| Effective area double reflection at 1.6 ° | lEBc | 0.8 - 4 |
| Effective area double reflection at 1.4 ° | lEBc | 0.8 - 4 |
| Effective area double reflection at 1.2 ° | lEBc | 0.8 - 4 |
| Effective area double reflection at 1.0 ° | lEBc | 0.8 - 4 |
| Effective area double reflection at 0.8 ° | lEBc | 0.8 - 4 |
| Effective area double reflection at 0.7 ° | lEBc | 0.8 - 4 |
| Effective area at 0.7°<br>- horizontal reflection<br>- vertical reflection | lEBc | 0.8 - 4 |
| Effective area at 1.2°<br>- horizontal reflection<br>- vertical reflection | lEBc | 0.8 - 4 |
| Single reflection mirror no. 9<br>- horizontal at 0.6° pitch, 0.9° yaw<br>- horizontal at 0.9° pitch, 0.9° yaw<br>- vertical at 0.6° yaw, 0.9° pitch | lEBc | 0.8 - 4 |
| Single reflection mirror no. 9<br>- vertical at 0.9° pitch, 0.9° yaw | lEBc | 0.8 - 4 |
| Effective area double reflection at 0.7 ° | mEBc | 2 - 8 |
| Effective area double reflection at 0.8 ° | mEBc | 2 - 8 |
| Effective area double reflection at 1.0 ° | mEBc | 2 - 8 |
| Effective area double reflection at 1.2 ° | mEBc | 2 - 8 |
| Effective area double reflection at 1.4 ° | mEBc | 2 - 8 |
| Single reflection mirror no. 9<br>- horizontal at 0.6° pitch, 0.9° yaw<br>- vertical at 0.6° yaw, 0.9° pitch | mEBc | 2 - 8 |

### 9.2.4 Laser alignment

Laser alignment of HORUS II experiment was done analogically to HORUS I campaign. The four-piece mirror module on a manipulator was at first aligned under 0° angle, then a 1° pitch and yaw tilts were introduced to observe single and double out-of-axis reflections. Resulting focal length of module in laser beam was 2000 mm.

### 9.2.5 X-ray alignment and focus search

Alignment in X-ray was also done similarly to HORUS I alignment. After pumping down, the alignment was carried out using Al-K energy line and TRoPIC detector. It started at the position of laser alignment at pitch and yaw angles tilt of 1°. At this starting point, first light image was taken and rough focus search started. Rough focus search was going -200 mm intrafocal to +250 mm intrafocal from the laser alignment position, with step size of 50 mm. According to calculated FWHM, best focus position was found and used as starting position for fine focus search.

Fine focus search was done from best rough focus position in range -100 mm to +100 mm in 20 mm steps, and FWHM at double reflection was calculated again. Resulting best focus was used during the rest of measurements. Compared to the laser pre-alignment, it was corrected, and new best focal length was 22054.16 mm for Al-K.

As focus search is not a direct part of this work, the image results and the figures are listed only in the Appendix B.

### 9.2.6 Test campaign results

This section shows the collection of campaign results. Presented are the figures of effective areas at different angles for the whole hybrid module, as well as measurements of single mirrors.

Figure 9.15 shows the effective areas of HORUS II plotted versus the ray energy in the low energy band continuum, from 0.8 keV to 3.7 keV. The individual lines are measurements for various incidence angles, with the shaded areas representing the $1\sigma$ confidence area.

The total reflectivity is the product of the reflectivities of the individual sub-modules. In HORUS II, there are contributions of two different coatings, Au and Cr-Ir. Accordingly, the drop in effective area towards higher energies and angles is dominated by the Au modules, see Figure 9.12.

Individual mirrors were tested as well, similar to HORUS I. For this a mask with a slit of 84 mm × 3 mm is used to block all but one mirror. In these measurements, always the central mirror no. 9 was active.

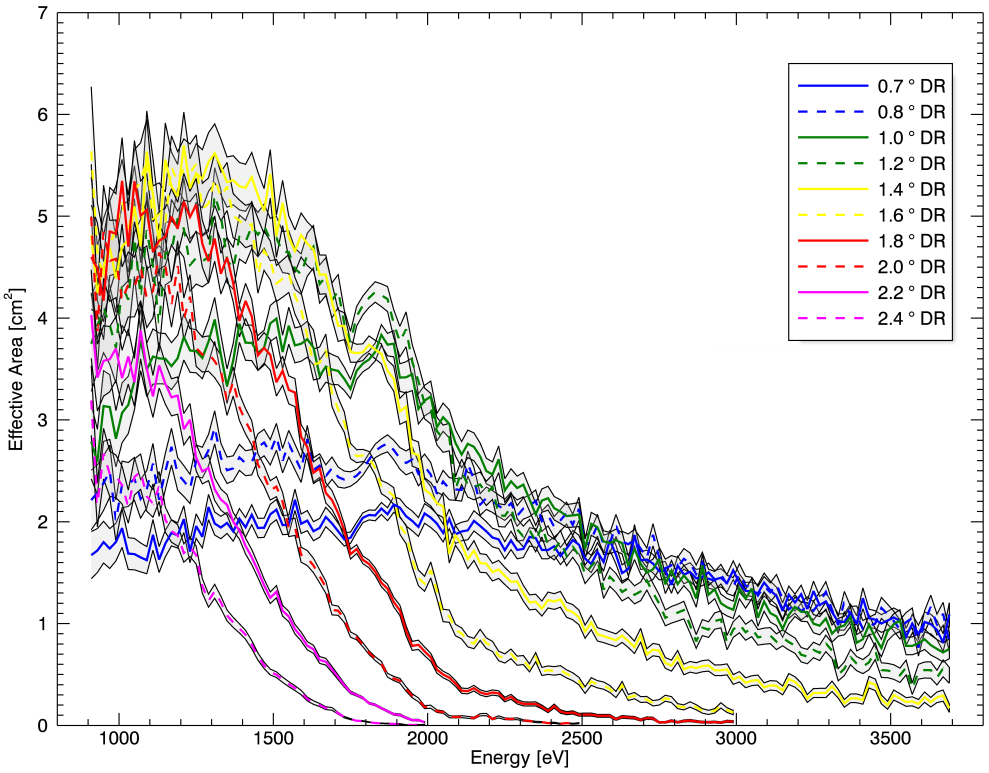


**Fig.** 9.15: Comparison of effective area at the double reflection spot in HORUS II configuration. Shaded areas represent $1\sigma$ confidence intervals. Measurement over lEBc. Please note that the effective area is not govern only by the reflectivity, but by the geometrical effects as well. The optics is designed to work with incidence angle 1.6°. At lower angles part of the incoming beam passes between the mirrors, and does not get reflected to the focus. With angles exceeding the ideal incidence angle, the loss is caused by mirror shadowing. (Geometrical problem as described in Fig. 3.3)

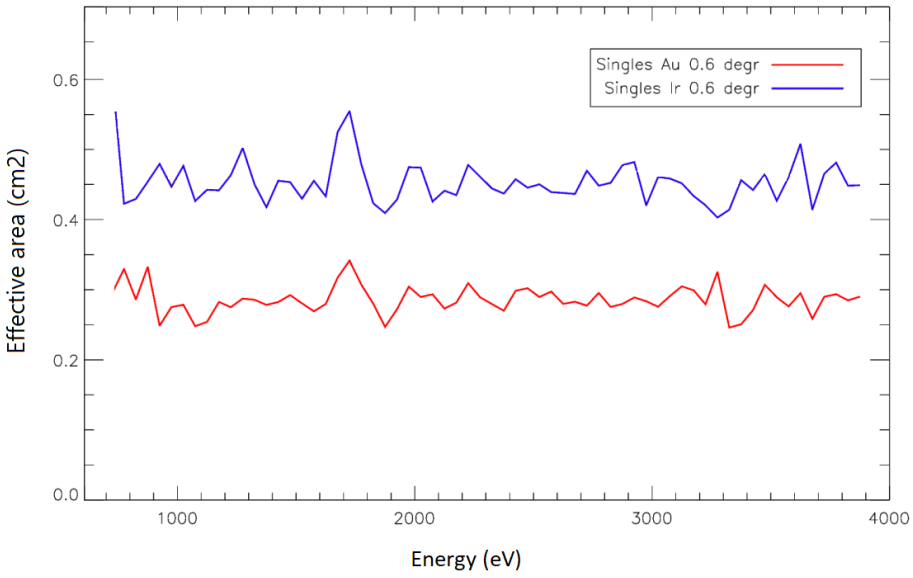


**Fig.** 9.16: Effective area for mirrors no. 9. Comparison of single reflection for horizontal and vertical mirror, i.e. golden and iridium coated one. Same as in case of HORUS I measurement, the single mirror coated with iridium shows about 50% higher effective area than the one coated with gold.

Result from measurement in lEBc can be seen in Figure 9.16. In this case, the angle is more shallow than during the comparative measurements for HORUS I configuration (0.6° versus 1.2° & 1.5°). Accordingly, reflectivity and effective area are less energy dependent in the shown energy range, showing close to constant values. The chromium-iridium mirror provides about 50% higher effective area over the whole measured energy range.

This difference seems too extreme to be caused only by the material choice for the reflective layer in otherwise identical mirrors properties. Another factor is the improved surface micro-roughness, as found in TEM scans, see Ch. 6, and quantified in Ch. 5. While the golden surfaces has crystalline structure, the amorphous layer of chromium in the chromium-iridium coated sub-module is smoother, thus more reflective.

Figure 9.17 shows the angle-dependence of the point spread function (PSF) of HORUS II. Plotted are the PSFs of single mirrors in both direction, as well as the focal, double reflection point. For single mirrors, the PSF values are higher in the horizontal direction, that means, for the golden mirror. For double reflection, the PSF values at low angles are similar for all measured energy lines and start to differ with angles over 1.6°. ICM performs better, with 3-4 arcmin compared to 5-6 arcmin PSF at angles below 1.5°. For higher angles both sub-modules focus worse and get more similar. Generalisation however would require more tests on physical samples, as the modules are not perfectly identical. Manual assembly does not guarantee repeatability, and in addition GCM has a 10 cm longer focal length.

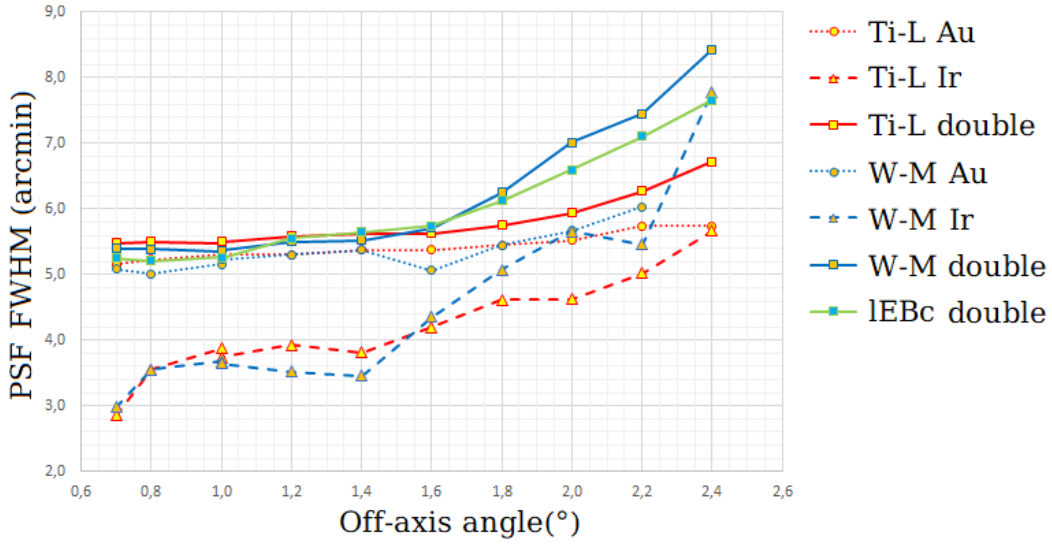


**Fig.** 9.17: The FWHM of the point spread function for various angles. Au and Ir refer to the x- and y-axis on the detector. The double reflection is the effective FWHM for the 2D image.

### 9.2.7 Conclusion

The experimental optics was tested in X-rays in a configuration which approximates the Kirkpatrick-Baez optics shape using two flat mirrors. Aim of the test was to obtain information about its behaviour, assess the PSF width, and the effective area of the optics, at various energies.

Comparative measurements on the full mirror aperture and individual mirrors confirms the improvement in effective area of the Cr-Ir layers, compared to the Au layer. The whole K-B-approximation module had the effective area of 4.8 $cm^2$ at 1 keV and 1.6° incident angle. The widths of the point spread functions (in 1D, line focus) for both sub-modules were determined, with ICM outperforming GCM. Cr-Ir coated sub-module showed PSF 3.7 arcmin at 1.0°, rising with the angle. In comparison with measurement of PSF in HORUS I campaign, this value is smaller - HORUS I shown for ICM PSF of 5.5 arcmin. In HORUS II configuration showed the gold coated module PSF 5.2 arcmin at 1°, which value corresponds to the results from HORUS I, where the obtained PSF for GCM was 5.2 arcmin as well. Difference between the HORUS I and II results are supposedly caused by mechanical re-organising of the modules. The PSF images of ICM showed in the Schmidt's arrangement a prolonged character in vertical direction, as can be seen in Fig. 9.4. This structure influenced the PSF negatively, but was eliminated during rearrangement of the modules into the HORUS II shape. Total PSF for the K-B approximation arrangement was 5.5 arcmin at 1°. Considering the

PSF of the iridium coated sub-module only, the potential of the design could be higher, but in this case, the total PSF was influenced by worse performance of the gold coated sub-modules. With all units in the same manufacturing quality and same coatings as had ICM during HORUS II campaign, the PSF could reach 3.6 arcmin at 1°.

Deeper understanding of the concept would require side-by-side test of HORUS II optics and a true K-B optics with similar geometrical properties, but parabolic shape of the mirrors. As such optics was not available during the test and its preparation was not scope of this thesis, a direct comparison cannot be provided.

# 10 Summary and conclusion

This thesis concludes seven years of designing, manufacturing and testing X-ray telescope mirrors, and later whole X-ray optics. The aim of the work was to study currently used technologies in terms of material selection and manufacturing, to investigate potential for improvement, and to apply and test the most promising alternatives.

The work started with the idea of creating a hybrid between the Kirkpatrick-Baez and lobster eye optics. Using multiple flat mirrors in a row as an approximation of K-B curved mirrors, the motivation was to simplify manufacturing in comparison with K-B, while reaching better resolution than has a simple lobster eye. This optics design development resulted in HORUS II optics, which was tested and has shown that the concept is viable.

The second development task was targeting an improvement in reflectivity, which grew into a model-driven development cycle of multiple layer mirrors. The sample manufacturing cycle led to optimised mirrors used in one half of the new hybrid optics demonstrator, enabling a comparison to the established gold layer. At first, the layers for HORUS optics were supposed to be sputtered iridium on silicon substrates. The reflectivity assessment in combination with stability concerns led to the application of two additional chromium layers: one as adhesive layer below the iridium, one as nanolayer on top to improve reflectivity around iridium absorption edges.

The layer development was a combination of simulation-based reflectivity optimisation and sample manufacturing. The success of this approach led to a hunt for the best possible layer quality and optimal composition. Numerous iterations of the layers were manufactured. With each step the measured sample parameters, like microroughness or oxidation depth, were used to update the simulation input. This resulted in a converging optimisation cycle for the reflectivity, restrained by the achievable sample properties during real world manufacturing. The flow of the work, testing and influences between individual steps can be seen in Figure 10.1.

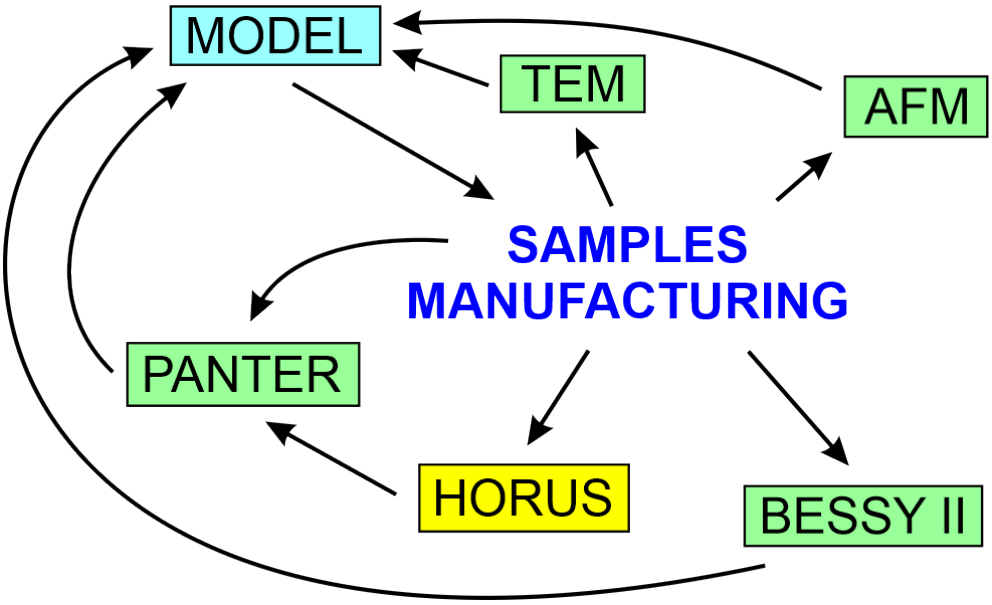


**Fig.** 10.1: Flowchart of performed work, composing the thesis.

Result of my work is a functional demonstrator, which quantitatively confirmed the potential of both, the hybrid optics and the chromium-iridium reflective layers. Going step-by-step, effective, reproducible reflective layers, well suited for space-born X-ray telescopes were obtained.

In my future work, I want to proceed with designing and testing of the materials for space-born telescope, as well as optics and other related systems.

# References


[1] H. Wolter, "Spiegelsysteme streifenden Einfalls als abbildende Optiken für Röntgenstrahlen," Annalen der Physik **445**, 94–114 (1952).

[2] N. Lund and S. Brandt, "Wide field monitoring of the X-ray sky using Rotation Modulation Collimators," Experimental Astronomy **6**, 19–24 (1995).

[3] R. Hudec, A. Inneman, L. Pina, and P. Gorenstein, "Replicated Reflectors for Wide Field X-Ray Imaging Telescopes," in "Imaging in High Energy Astronomy," (Springer Netherlands, Dordrecht, 1995), pp. 263–266.

[4] F. D. Seward and P. A. Charles, *Exploring the X-ray Universe* (Cambridge University Press, 2010).

[5] D. Barret, K. Nandra, X. Barcons, A. Fabian, J.-W. D. Herder, L. Piro, M. Watson, J. Aird, G. Branduardi-Raymont, M. Cappi, F. Carrera, A. Comastri, E. Costantini, J. Croston, A. Decourchelle, C. Done, M. Dovciak, S. Ettori, A. Finoguenov, A. Georgakakis, P. Jonker, J. Kaastra, G. Matt, C. Motch, P. O'Brien, G. Pareschi, E. Pointecouteau, G. Pratt, G. Rauw, T. Reiprich, J. Sanders, S. Sciortino, R. Willingale, and J. Wilms, "Athena+: The first Deep Universe X-ray Observatory," ArXiv e-prints **1310**, 7 (2013).

[6] R. Giacconi, W. P. Reidy, T. Zehnpfennig, J. C. Lindsay, and W. S. Muney, "Solar x-ray image obtained using grazing-incidence optics," Astrophysical Journal **142**, 1274–1278 (1965).

[7] C. U. Keller, "X-rays from the sun," Experientia **51**, 710–720 (1995).

[8] M. Blazek, P. Pata, A. Inneman, and P. Skala, "Astronomical Tasks for Tests of X-Ray Optics in VZLUSAT-1 Nanosatellite," Advances in Astronomy **2017**, 1–6 (2017).

[9] F. E. Marshall, E. A. Boldt, S. S. Holt, R. Mushotzky, S. H. Pravdo, R. E. Rothschild, and P. J. Serlemitsos, "New Hard X-ray Sources Observed with HEAO A-2," The Astrophysical Journal Supplement Series **40**, 657 (1979).

[10] R. Giacconi, G. Branduardi, U. Briel, a. Epstein, D. Fabricant, E. Feigelson, S. S. Holt, R. H. Becker, E. a. Boldt, and P. J. Serlemitsos, "The Einstein 'HEAO 2' X-ray Observatory," The Astrophysical Journal **230**, 540 (1979).

[11] J. E. Trümper and G. Hasinger, eds., *The Universe in X-Rays*, Astronomy and Astrophysics Library (Springer Berlin Heidelberg, Berlin, Heidelberg, 2008).

[12] B. G. Taylor, R. D. Andresen, A. Peacock, and R. Zobl, "The Exosat mission," Space Science Reviews **30**, 479–494 (1981).

[13] Y. Tanaka, H. Inoue, and S. S. Holt, "The X-Ray Astronomy Satellite ASCA," Publ. Astron. Soc. Jap.**46**, L37–L41 (1994).

[14] P. Serlemitosos and all, "The X-ray Telescope with ASCA," Astronomical Society Japan **47**, 105 (1995).

[15] J. Trümper, "The rosat mission," Advances in Space Research **2**, 241 – 249 (1982).

[16] J. H. M. M. Schmitt, B. Aschenbach, G. Hasinger, E. Pfeffermann, P. Predehl, and J. Trümper, "A soft X-ray image of the Moon," Nature **394**, 583 – 587 (1991).

[17] ""XMM-Newton Users Handbook", Issue 2.19, 2021 (ESA: XMM-Newton SOC)," .

[18] M. C. Weisskopf, H. D. Tananbaum, L. P. Van Speybroeck, and S. L. O'Dell, "Chandra X-ray Observatory (CXO): overview," Proc. SPIE Vol. 4012 **4012**, 2–16 (2000).

[19] A. Merloni, P. Predehl, W. Becker, H. Böhringer, T. Boller, H. Brunner, M. Brusa, K. Dennerl, M. Freyberg, P. Friedrich, A. Georgakakis, F. Haberl, G. Hasinger, N. Meidinger, J. Mohr, K. Nandra, A. Rau, T. H. Reiprich, J. Robrade, M. Salvato, A. Santangelo, M. Sasaki, A. Schwope, J. Wilms, and the German eROSITA Consortium, *eROSITA Science Book: Mapping the Structure of the Energetic Universe* (MPE, Garching, 2012), 1st ed.

[20] Predehl, P., Andritschke, R., Arefiev, V., Babyshkin, V., Batanov, O., Becker, W., Böhringer, H., Bogomolov, A., Boller, T., Borm, K., Bornemann, W., Bräuninger, H., Brüggen, M., Brunner, H., Brusa, M., Bulbul, E., Buntov, M., Burwitz, V., Burkert, W., Clerc, N., Churazov, E., Coutinho, D., Dauser, T., Dennerl, K., Doroshenko, V., Eder, J., Emberger, V., Eraerds, T., Finoguenov, A., Freyberg, M., Friedrich, P., Friedrich, S., Fürmetz, M., Georgakakis, A., Gilfanov, M., Granato, S., Grossberger, C., Gueguen, A., Gureev, P., Haberl, F., Hälker, O., Hartner, G., Hasinger, G., Huber, H., Ji, L., Kienlin, A. v., Kink, W., Korotkov, F., Kreykenbohm, I., Lamer, G., Lomakin, I., Lapshov, I., Liu, T., Maitra, C., Meidinger, N., Menz, B., Merloni, A., Mernik, T., Mican, B., Mohr, J., Müller, S., Nandra, K., Nazarov, V., Pacaud, F., Pavlinsky, M., Perinati, E., Pfeffermann, E., Pietschner, D., Ramos-Ceja, M. E., Rau, A., Reiffers, J., Reiprich, T. H., Robrade, J., Salvato, M., Sanders, J., Santangelo, A., Sasaki, M., Scheuerle, H., Schmid, C., Schmitt, J., Schwope, A., Shirshakov, A., Steinmetz, M., Stewart, I., Strüder, L., Sunyaev, R., Tenzer, C., Tiedemann, L., Trümper, J., Voron, V., Weber, P., Wilms, J., and Yaroshenko, V., "The erosita x-ray telescope on srg," A&A **647**, A1 (2021).

[21] Y. Liao, Z. Shen, and Z. Wang, "Design of conical Wolter-I geometry with sectioned secondary mirrors for x-ray telescopes," Journal of Astronomical Telescopes, Instruments, and Systems **5**, 014004 (2019).

[22] R. A. Harrison and A. Fludra, "Coronal diagnostic spectrometer on soho," (1995).

[23] F. Graham-Smith, *Eyes on the Sky: A Spectrum of Telescopes* (Oxford University Press, 2016).

[24] P. Murdin, M. Giavalisco, L. C. Ho, and J. Kormendy, "The Encyclopedia of Astronomy and Astrophysics," (2001).

[25] R. Hudec, "Kirkpatrick-Baez (KB) and lobster eye (LE) optics for astronomical and laboratory applications," X-Ray Optics and Instrumentation **2010**, 1–39 (2010).

[26] H. E. Martz, C. M. Logan, D. J. Schneberk, and P. J. Shull, *X-ray Imaging: Fundamentals, Industrial Techniques and Applications* (CRC Press, 2016).

[27] R. Hudec, L. Pina, A. Inneman, and L. Sveda, "Variable X–ray sky with Lobster Eye Telescopes," Nuclear Physics B – Proceedings Supplements **132**, 320–323 (2004).

[28] O. Nentvich, M. Urban, V. Stehlikova, L. Sieger, and R. Hudec, "Lobster eye X-ray optics: Data processing from two 1D modules," Contributions of the Astronomical Observatory Skalnate Pleso **47**, 178–183 (2017).

[29] A. Inneman, "Technologicke aspekty vyvoje a vyroby optickych prvku pro rentgenove zareni," Ph.D. thesis, Czech Technical University in Prague (2001).

[30] J. R. P. Angel, "Lobster eyes as X-ray telescopes," The Astrophysical Journal **233**, 364 (1979).

[31] V. B. Meyer-Rochow and J. Gál, "Dimensional limits for arthropod eyes with superposition optics," Vision Research **44**, 2213–2223 (2004).

[32] M. F. Land, "Eyes with mirror optics," Journal of Optics A: Pure and Applied Optics **2**, R44–R50 (2000).

[33] M. F. Land, "Animal Eyes with Mirror Optics," Scientific American **239**, 126–134 (1978).

[34] H. N. Chapman, K. A. Nugent, and S. W. Wilkins, "X-ray focusing using square channel-capillary arrays," Review of Scientific Instruments **62**, 1542–1561 (1991).

[35] Y. Zhang, S. Qiao, L. Sun, Q. W. Shi, W. Huang, L. Li, and Z. Yang, "Photoinduced active terahertz metamaterials with nanostructured vanadium dioxide film deposited by sol-gel method," Optics express **22**, 11070–8 (2014).

[36] W. K. H. Schmidt, "A proposed X-ray focusing device with wide field of view for use in X-ray astronomy," Nuclear Instruments and Methods **127**, 285–292 (1975).

[37] O. Nentvich, V. Stehlikova, M. Urban, R. Hudec, and L. Sieger, "Data processing from lobster eye type optics," in "EUV and X-ray Optics: Synergy between Laboratory and Space V," (SPIE, 2017).

[38] P. Kirkpatrick and A. V. Baez, "Formation of Optical Images by X-Rays," Journal of the Optical Society of America **38**, 766 (1948).

[39] N. An, X. Du, Q. Wang, Z. Cao, S. Jiang, and Y. Ding, "Kirkpatrick-Baez microscope with spherical multilayer mirrors around 2.5keV photon energy," in "Target Diagnostics Physics and Engineering for Inertial Confinement Fusion III," , vol. 9211 P. M. Bell and G. P. Grim, eds., International Society for Optics and Photonics (SPIE, 2014), vol. 9211, p. 92110I.

[40] L. M. Cohen, "Optimum shape of a Kirkpatrick-Baez X-ray reflector supported at discrete points for on-axis performance," Applied Optics **20**, 1545 (1981).

[41] R. Hudec, L. Pina, A. Inneman, L. Sveda, H. Ticha, V. Semencova, and V. Brozek, "Innovative technologies for future astronomical x-ray mirrors," in "UV and Gamma-Ray Space Telescope Systems," , vol. 5488 G. Hasinger and M. J. L. Turner, eds., International Society for Optics and Photonics (SPIE, 2004), vol. 5488, pp. 875 – 885.

[42] G. E. Ice, C. R. Hubbard, B. C. Larson, J. W. L. Pang, J. D. Budai, S. Spooner, and S. C. Vogel, "Kirkpatrick–Baez microfocusing optics for thermal neutrons," Nuclear Instruments and Methods in Physics Research Section A: Accelerators, Spectrometers, Detectors and Associated Equipment **539**, 312–320 (2005).

[43] V. Stehlikova, A.-C. Probst, O. Nentvich, M. Urban, A. Inneman, L. Sieger, V. Marsikova, and T. Dohring, "Development of iridium coated silicon x-ray mirrors for lobster eye astronomical telescope," in "Proceedings of 5th EOS Conference on Manufacturing of Optical Systems," (2017).

[44] J. J. Kolodziejczak, R. F. Elsner, R. A. Austin, and S. L. O'Dell, "Ion transmission to the focal plane of the chandra x-ray observatory," in "X-Ray and Gamma-Ray Instrumentation for Astronomy XI," , vol. 4140 (2000), vol. 4140, pp. 135–143.

[45] T. Dohring, A.-C. Probst, F. Emmerich, M. Stollenwerk, V. Stehlikova, P. Friedrich, and C. Damm, "Development of iridium coated x-ray mirrors for astronomical applications," in "Society of Photo-Optical Instrumentation Engineers," , vol. 10399 (2017), vol. 10399.

[46] W. K. H. Schmidt, "A proposed x-ray focusing device with wide field of view for use in x-ray astronomy," Nuclear Instruments and Methods **127**, 285–292 (1975).

[47] R. Hudec, L. Pina, A. Inneman, and V. Tichy, "Applications of lobster eye optics," in "EUV and X-ray Optics: Synergy between Laboratory and Space IV," , vol. 9510 (SPIE, 2015), vol. 9510.

[48] V. Stehlikova, A.-C. Probst, O. Nentvich, and M. Urban, "Reflective coating layers for X-ray optics," in "Axro 2016," (2016).

[49] B. Henke, E. Gullikson, and J. Davis, "X-ray interactions: photoabsorption, scattering, transmission, and reflection at E=50-30000 eV, Z=1-92," Atomic Data and Nuclear Data Tables **54**, 181–342 (1993).

[50] B. Aschenbach, "REVIEW ARTICLE: X-ray telescopes," Reports on Progress in Physics **48**, 579–629 (1985).

[51] R. Giacconi, W. P. Reidy, G. S. Vaiana, L. P. Van Speybroeck, and T. F. Zehnpfennig, "Grazing-incidence telescopes for X-ray astronomy," Space Science Reviews **9**, 3–57 (1969).

[52] M. Bass, C. DeCusatis, J. Enoch, V. Lakshminarayanan, G. Li, C. MacDonald, V. Mahajan, and E. V. Stryland, *Handbook of Optics: Volume 1* (OSA publishing, New York, 2010), 3rd ed.

[53] A.-C. Probst, M. Stollenwerk, M. Wen, L. Proserpio, and T. Dohring, "Iridium coatings for space based x-ray optics," in "International Conference on Space Optics," (SPIE, 2017), p. 177.

[54] A.-C. Probst, M. Stollenwerk, F. Emmerich, A. Büttner, S. Zeising, J. Stadtmüller, F. Riethmüller, V. Stehlíková, M. Wen, L. Proserpio, C. Damm, B. Rellinghaus, and T. Döhring, "Influence of sputtering pressure on the nanostructure and the X-ray reflectivity of iridium coatings," Surface and Coatings Technology (2017).

[55] D. M. Broadway, J. Weimer, D. Gurgew, T. Lis, B. D. Ramsey, S. L. O'Dell, M. Gubarev, A. Ames, and R. Bruni, "Achieving zero stress in iridium, chromium, and nickel thin films," in "EUV and X-ray Optics: Synergy between Laboratory and Space IV," , vol. 9510 of *Proc. SPIE* (2015), vol. 9510 of *Proc. SPIE*, p. 95100E.

[56] A. Ames, R. Bruni, V. Cotroneo, R. Johnson-Wilke, T. Kester, P. Reid, S. Romaine, S. Tolier-McKinstry, and R. H. T. Wilke, "Using iridium films to compensate for piezo-electric materials processing stresses in adjustable x-ray optics," in "Optics for EUV, X-Ray, and Gamma-Ray Astronomy VII," , vol. 9603 S. L. O'Dell and G. Pareschi, eds., International Society for Optics and Photonics (SPIE, 2015), vol. 9603, pp. 413 – 420.

[57] A. Büttner, A.-C. Probst, F. Emmerich, C. Damm, B. Rellinghaus, T. Döhring, and M. Stollenwerk, "Influence of sputtering pressure on microstructure and layer properties of iridium thin films," Thin Solid Films **662**, 41–46 (2018).

[58] A.-C. Probst, T. Dohring, M. Stollenwerk, L. Proserpio, and M. Wen, "Iridium coatings for space based X-ray optics," in "Space Optics," (Biarritz, 2016).

[59] T. Döhring, M. Stollenwerk, P. Schmitt, and A. Szeghalmi, "Environmentally stable iridium mirror coatings for the infrared spectral range," in "Ninth European Seminar on Precision Optics Manufacturing," , vol. 12298 A. Haberl, G. Fütterer, O. W. Fähnle, and C. Wünsche, eds., International Society for Optics and Photonics (SPIE, 2022), vol. 12298, p. 122980A.

[60] V. Stehlikova, M. Urban, O. Nentvich, A. Inneman, T. Döhring, and A.-C. Probst, "Study of lobster eye optics with iridium coated x-ray mirrors for a rocket experiment," in "EUV and X-ray Optics: Synergy between Laboratory and Space V," , vol. 10235 R. Hudec and L. Pina, eds., International Society for Optics and Photonics (SPIE, 2017), vol. 10235, p. 1023505.

[61] A.-C. Probst, T. Begou, T. Döhring, S. Zeising, M. Stollenwerk, J. Stadtmüller, F. Emmerich, and J. Lumeau, "Coating stress analysis and compensation for iridium-based x-ray mirrors," Appl. Opt. **57**, 8775–8779 (2018).

[62] F. Delmotte, J. Meyer-Ilse, F. Salmassi, R. Soufli, C. Burcklen, J. Rebellato, A. Jerome, I. Vickridge, E. Briand, and E. Gullikson, "Soft x-ray optical constants of sputtered chromium thin films with improved accuracy in the l and m absorption edge regions," Journal of Applied Physics **124**, 035107 (2018).

[63] D. B. Williams and C. B. Carter, *Transmission Electron Microscopy: A Textbook for Materials Science, 2nd Edition.* (Springer New York, NY, 2009).

[64] M. J. Freyberg, B. Budau, V. Burwitz, K. Dennerl, G. Hartner, A. von Kienlin, B. Menz, and B. Mican, "Calibration of the eROSITA calibration source: design and trade-off analysis ," in "Space Telescopes and Instrumentation 2012: Ultraviolet to Gamma Ray," , vol. 8443 T. Takahashi, S. S. Murray, and J.-W. A. den Herder, eds., International Society for Optics and Photonics (SPIE, 2012), vol. 8443, p. 844351.

[65] M. Freyberg, B. Budau, W. Burkert, P. Friedrich, G. Hartner, K. Misaki, and M. Mühlegger, "New technology and techniques for x-ray mirror calibration at panter," Proc SPIE **7011** (2008).

[66] A. Jafari, D. D. M. Ferreira, S. Kadkhodazadeh, T. Kasama, S. Massahi, S. Svendsen, L. M. Vu, P. L. Henriksen, Z. M. Balogh, M. Krumrey, L. Cibik, F. E. Christensen, and B. Shortt, "Long-term performance and durability of Ir/B4C multilayer x-ray mirrors: focusing on composition, structure, and reflectivity properties," Journal of Astronomical Telescopes, Instruments, and Systems **6**, 034005 (2020).

[67] M. Krumrey and G. Ulm, "High-accuracy detector calibration at the ptb four-crystal monochromator beamline," Nuclear Instruments and Methods in Physics

Research Section A: Accelerators, Spectrometers, Detectors and Associated Equipment **467-468**, 1175–1178 (2001). Proceedings of the 7th Int. Conf. on Synchrotron Radiation Instrumentation.

[68] D. Fuchs, M. Krumrey, P. Müller, F. Scholze, and G. Ulm, "High precision soft x-ray reflectometer," Review of Scientific Instruments **66**, 2248–2250 (1995).

[69] D. Lumb, F. Christensen, C. Jensen, and M. Krumrey, "Influence of a carbon over-coat on the x-ray reflectance of xeus mirrors," Optics Communications **279**, 101–105 (2007).

[70] T. Döhring, M. Stollenwerk, J. Stadtmüller, S. Zeising, D. Flachs, V. Stehlikova, V. Burwitz, M. K. Krumrey, V. Cotroneo, and M. Klementova, "Characterisation of x-ray mirrors based on chromium-iridium tri-layer coatings," in "Proceedings of SPIE," , vol. 2021 (2021), vol. 2021, pp. 1177607–1 – 11776076.

# A Appendix A

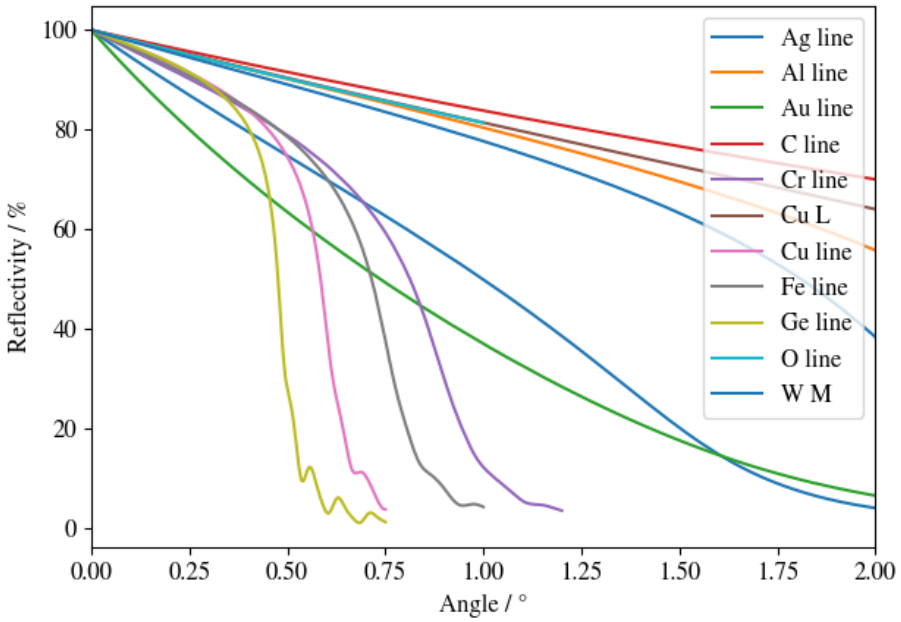


**Fig.** A.1: Reflectivity of Ir coated mirror without additive overcoatings, for the chosen scale of sources at PANTER test facility. Henke tables based simulation in 500 steps.

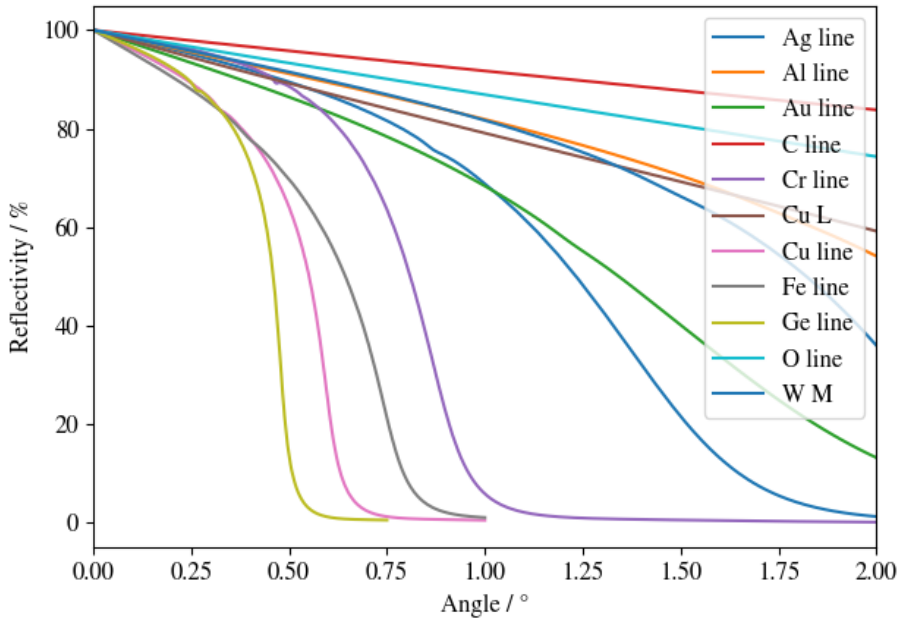


**Fig.** A.2: Reflectivity of Ir coated mirror with 4 nm Cr overcoating, for the chosen scale of sources at PANTER test facility. Henke tables based simulation in 500 steps.

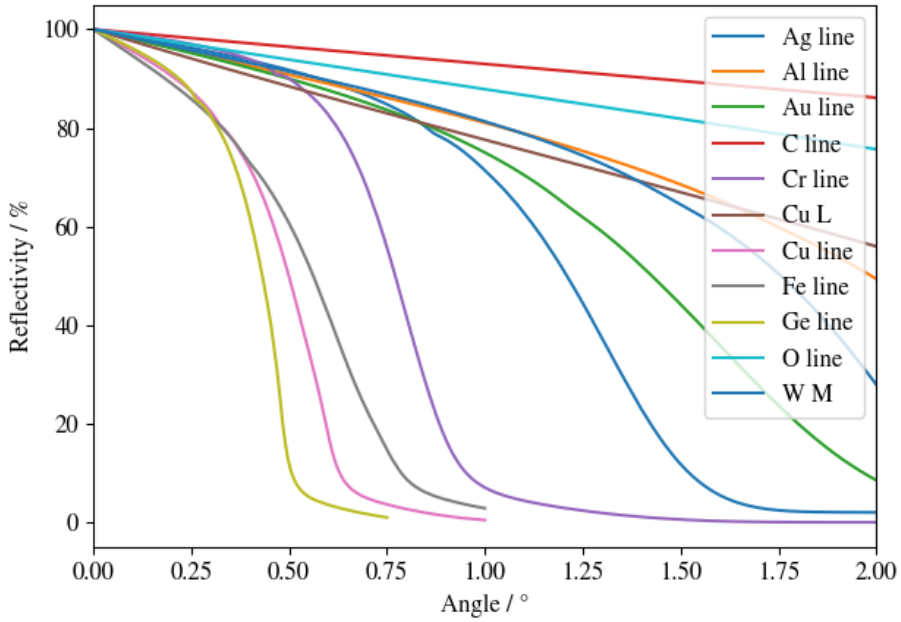


**Fig.** A.3: Reflectivity of Ir coated mirror with 6 nm Cr overcoating, for the chosen scale of sources at PANTER test facility. Henke tables based simulation in 500 steps.

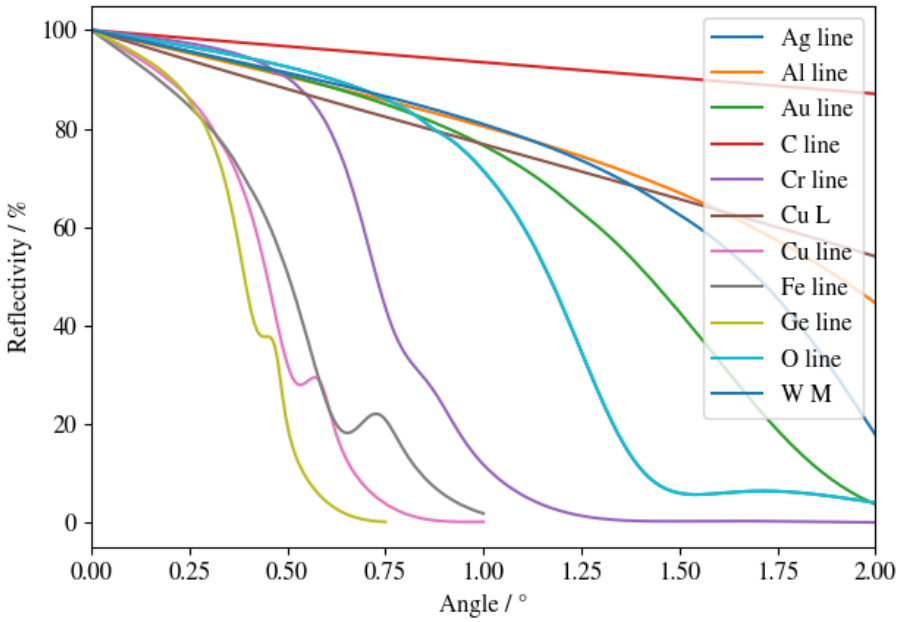


**Fig.** A.4: Reflectivity of Ir coated mirror with 8 nm Cr overcoating, for the chosen scale of sources at PANTER test facility. Henke tables based simulation in 500 steps.

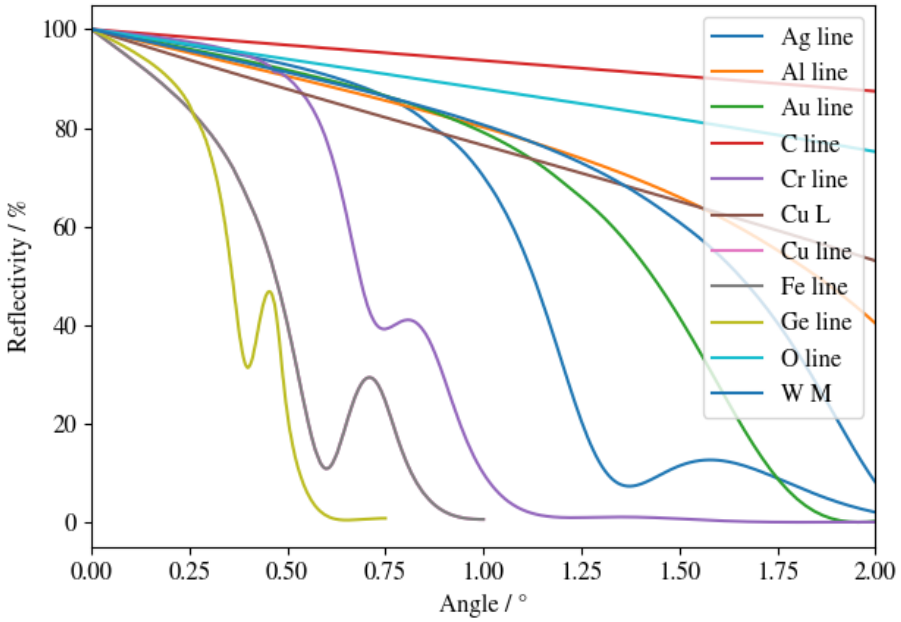


**Fig.** A.5: Reflectivity of Ir coated mirror with 10 nm Cr overcoating, for the chosen scale of sources at PANTER test facility. Henke tables based simulation in 500 steps.

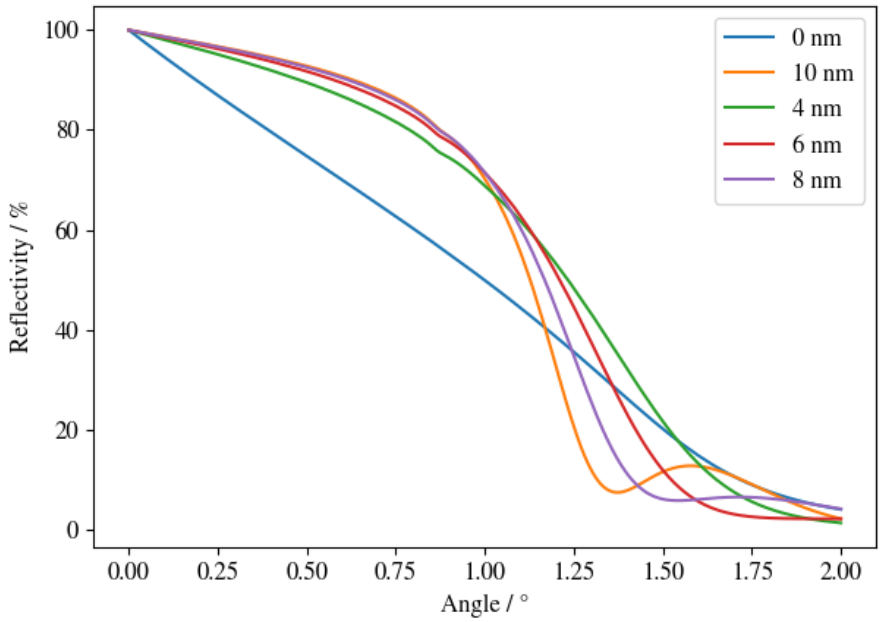


**Fig.** A.6: Comparison of Ir or Ir/Cr layers reflectivity, in case of incidence energy corresponding to Ag-K line. Henke tables based simulation in 500 steps.

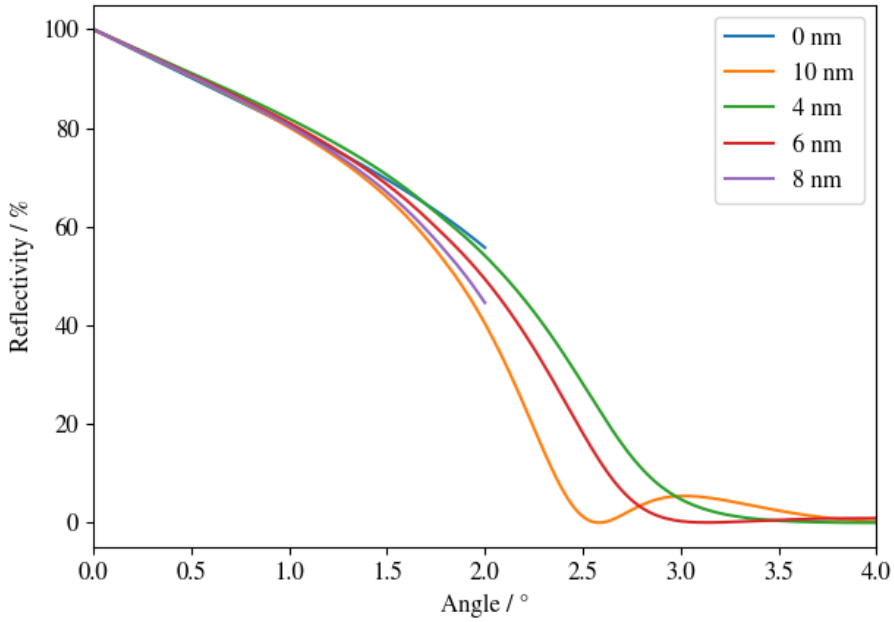


**Fig.** A.7: Comparison of Ir or Ir/Cr layers reflectivity, in case of incidence energy corresponding to Al-K line. Henke tables based simulation in 500 steps.

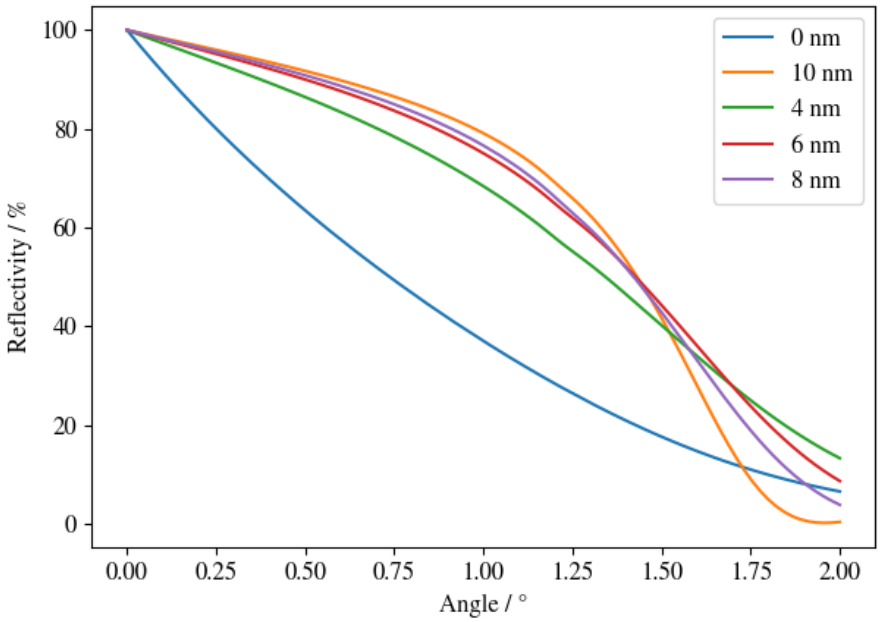


**Fig.** A.8: Comparison of Ir or Ir/Cr layers reflectivity, in case of incidence energy corresponding to Au-K line. Henke tables based simulation in 500 steps.

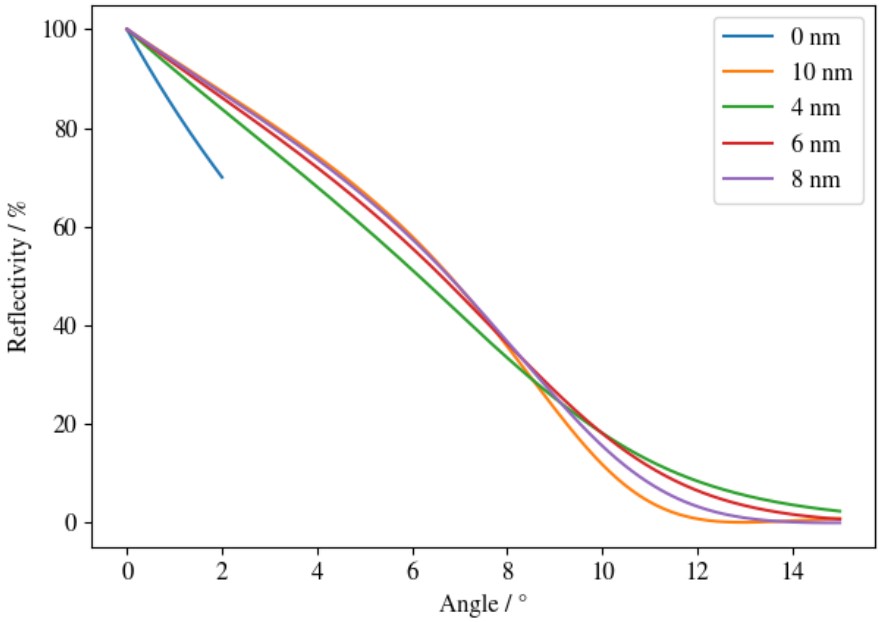


**Fig.** A.9: Comparison of Ir or Ir/Cr layers reflectivity, in case of incidence energy corresponding to C-K line. Henke tables based simulation in 500 steps.

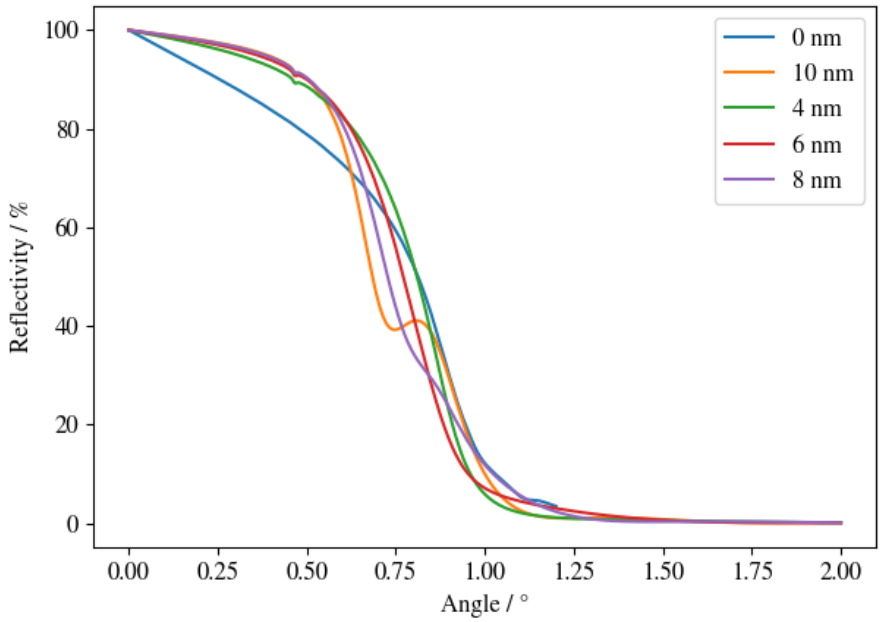


**Fig.** A.10: Comparison of Ir or Ir/Cr layers reflectivity, in case of incidence energy corresponding to Cr-K line. Henke tables based simulation in 500 steps.

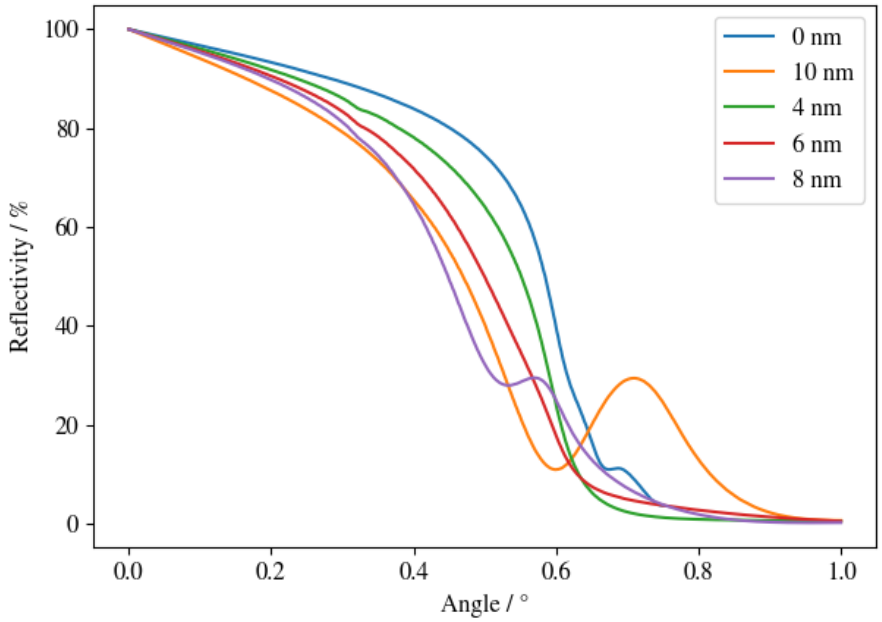


**Fig.** A.11: Comparison of Ir or Ir/Cr layers reflectivity, in case of incidence energy corresponding to Cu-K line. Henke tables based simulation in 500 steps.

# B Appendix B

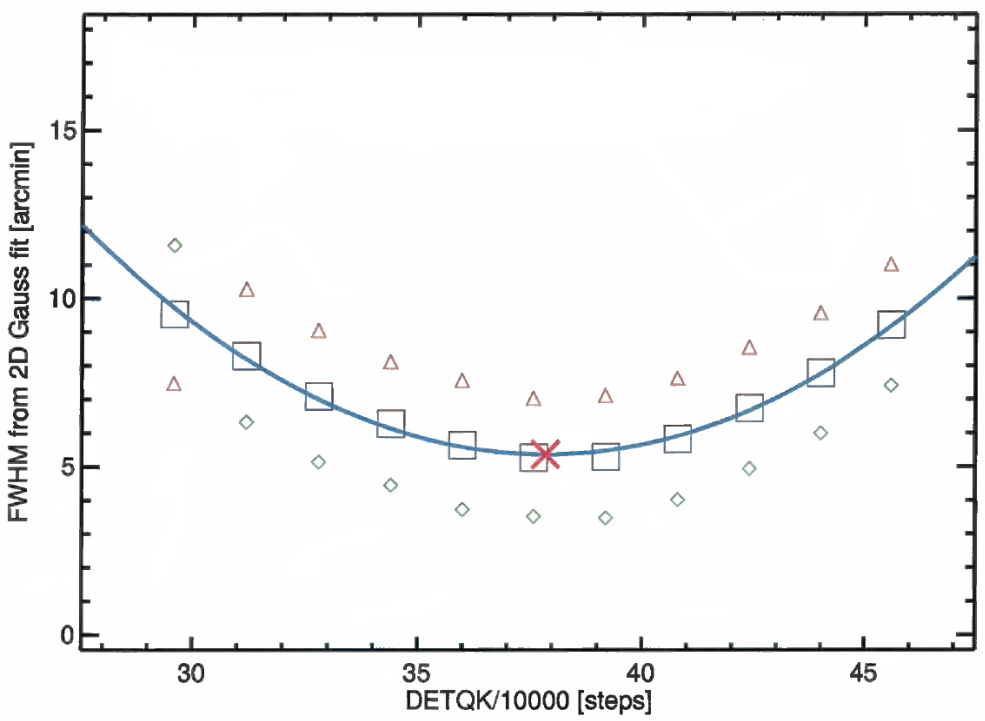


**Fig.** B.1: Focus search at Al-K for HORUS I, ICM set-up, showing the FWHM versus detector location. Fitted FWHM values from a 2D Gaussian fitted to the images along x-axis (green circle) and y-axis (red triangle), see B.2. Blue squares are the average FWHM values, to which a parabola is fitted (blue line), in which the minimum (red cross) is interpreted as ideal focal point.

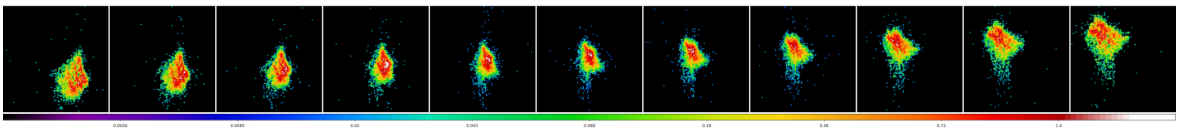

**Fig.** B.2: HORUS I - The double reflection images along the focus search at Al-K for ICM. Left to right: the scan from -100 mm to +100 mm in steps of 20 mm.

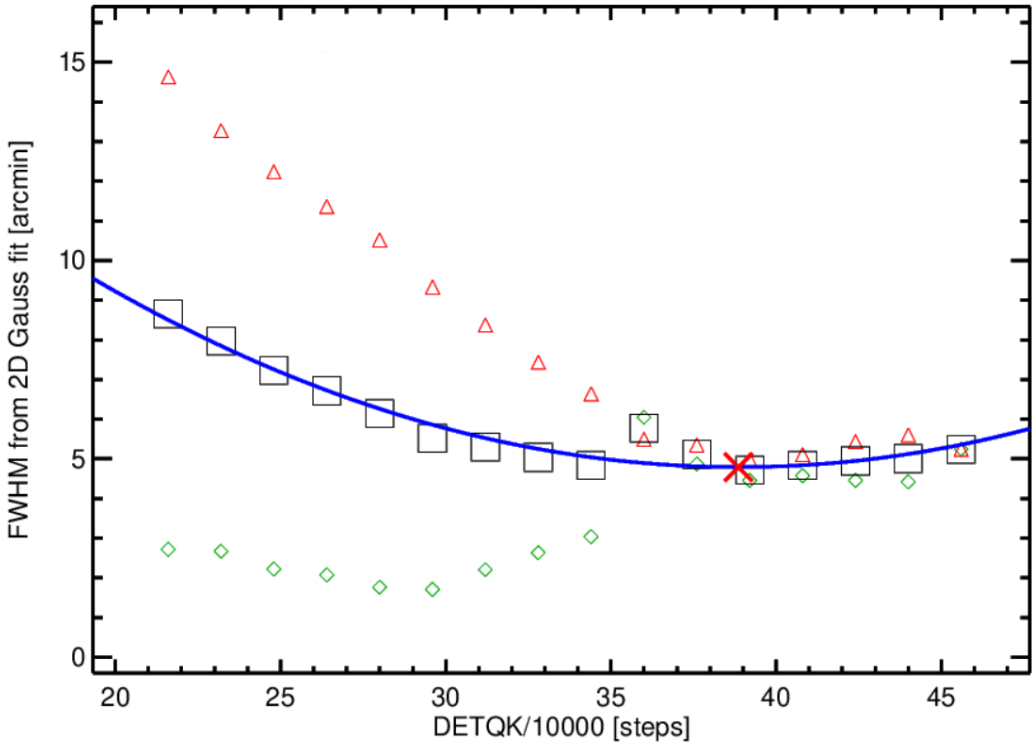


**Fig.** B.3: Focus search at Al-K for HORUS I, GCM set-up, showing the FWHM versus detector location. Fitted FWHM values from a 2D Gaussian fitted to the images along x-axis (green circle) and y-axis (red triangle), see B.4. Blue squares are the average FWHM values, to which a parabola is fitted (blue line), in which the minimum (red cross) is interpreted as ideal focal point.

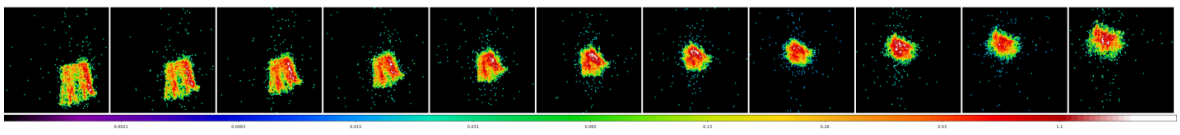

**Fig.** B.4: HORUS I - The double reflection images along the focus search at Al-K for GCM. Left to right: the scan from -200 mm to +100 mm in steps of 20 mm around the rough best focus position of the ICM.

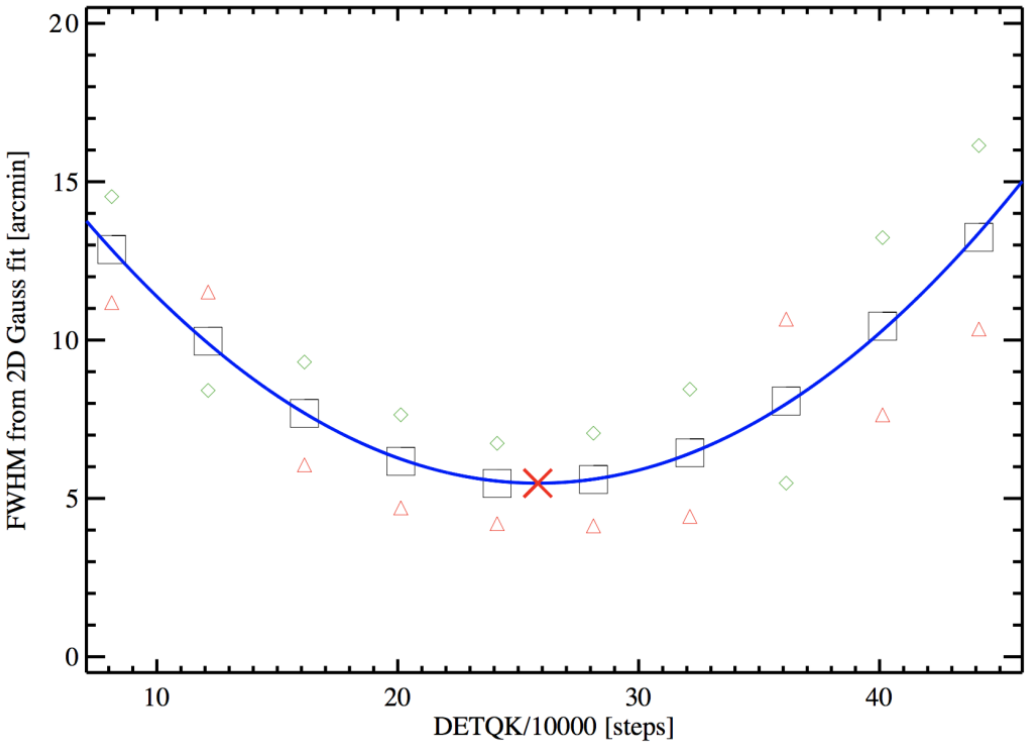


**Fig.** B.5: Rough focus search at Al-K for HORUS II set-up, showing the FWHM versus detector location. Fitted FWHM values from a 2D Gaussian fitted to the images along x-axis (green circle) and y-axis (red triangle), see B.6. Blue squares are the average FWHM values, to which a parabola is fitted (blue line), in which the minimum (red cross) is interpreted as ideal focal point.

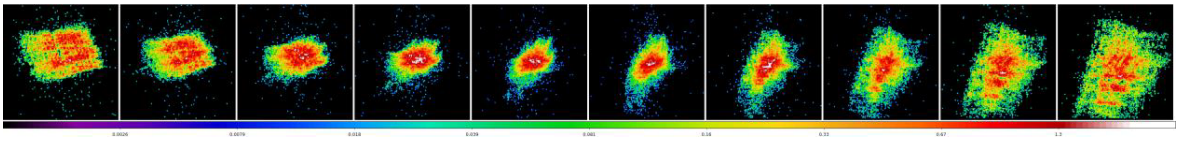

**Fig.** B.6: PSF at different positions of HORUS II set-up for rough focus search. Left to right: the scan from -200 mm to +250 mm in steps of 50 mm.

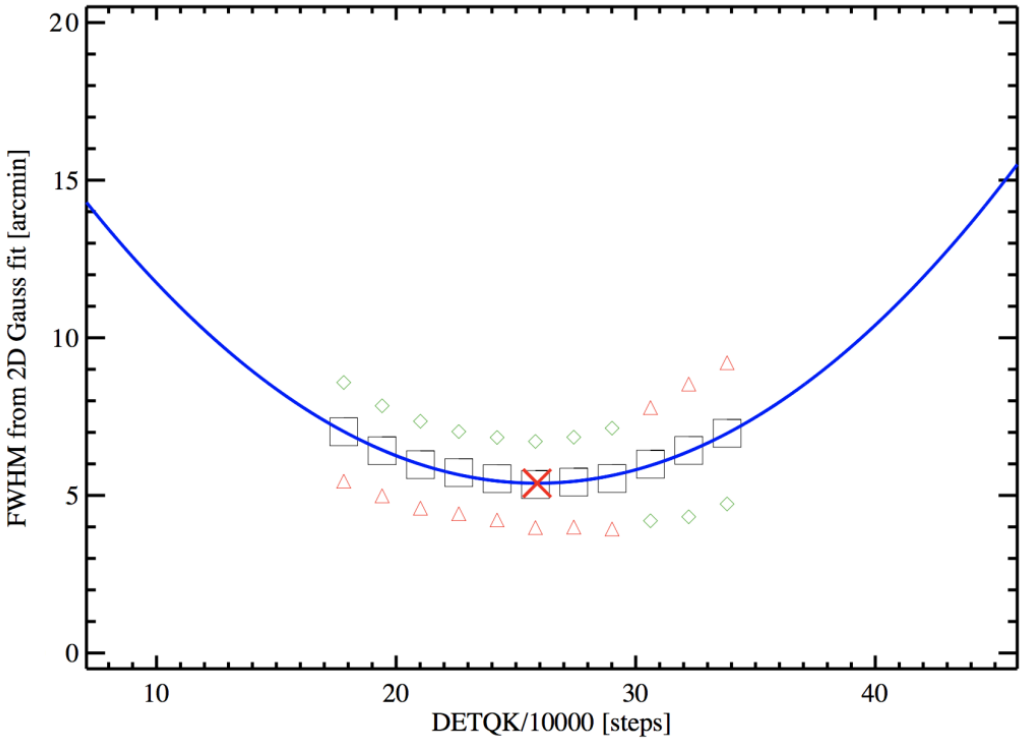


**Fig.** B.7: Rough focus search at Al-K for HORUS II set-up, showing the FWHM versus detector location. Fitted FWHM values from a 2D Gaussian fitted to the images along x-axis (green circle) and y-axis (red triangle), see B.8. Blue squares are the average FWHM values, to which a parabola is fitted (blue line), in which the minimum (red cross) is interpreted as ideal focal point.

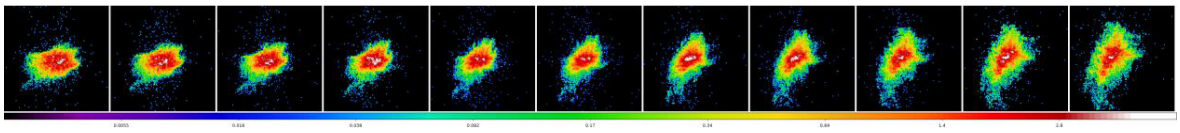

**Fig.** B.8: PSF at different positions along the fine focus search at Al-K for HORUS II set-up. Left to right: the scan from -100 mm to +100 mm in steps of 20 mm around the rough best focus position.

# C Appendix C

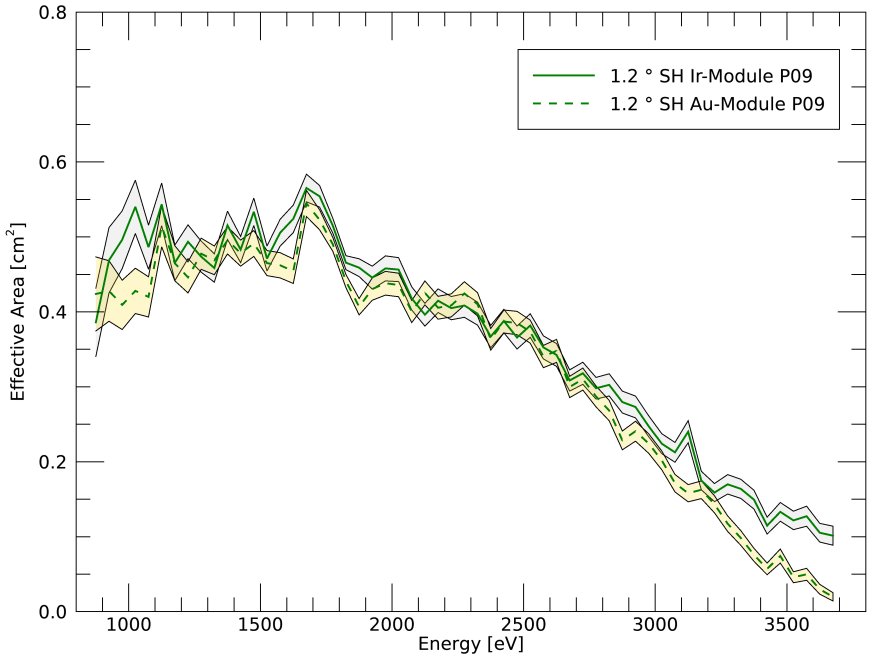


**Fig.** C.1: Comparison of effective area measurements of ICM and GCM plates no.09 at 1.2° in the lEBc. Shaded areas represent $1\sigma$ confidence intervals.

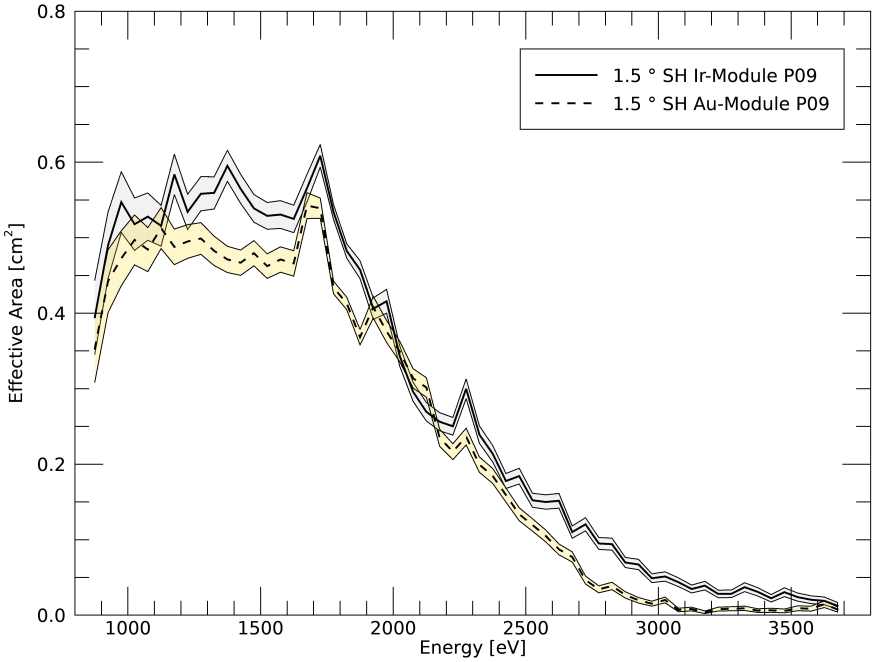


**Fig.** C.2: Comparison of effective area measurements of ICM and GCM plates no.09 at 1.5° in the lEBc. Shaded areas represent $1\sigma$ confidence intervals.

Publications of the author Veronika Stieglitz (born Stehlíková)

- Journal articles

Veronika Stehlikova, Anne-Catherine Probst, Ondrej Nentvich, Martin Urban, Ladislav Sieger, Thorsten Döhring, René Hudec, "Study of multiple layers coatings for X-ray mirrors", Contributions of the Astronomical Observatory Skalnate Pleso, 2018, volume 48, no 3, pg. 488-497

Stehlikova, V. Urban, M. Nentvich, O. Daniel, V. Sieger, L. and Tutt, J., "Hard X-ray Vela supernova observation on rocket experiment WRX-R", Contributions of the Astronomical Observatory Skalnate Pleso, 2017, volume 47, no 2, pg. 165-169, https://ui.adsabs.harvard.edu/abs/2017CoSka..47..165S

A.-C. Probst, M. Stollenwerk, F. Emmerich, A. Büttner, S. Zeising, J. Stadtmüller, F. Riethmüller, V. Stehlíková, M. Wen, L. Proserpio, C. Damm, B. Rellinghaus, T. Döhring, Influence of sputtering pressure on the nanostructure and the X-ray reflectivity of iridium coatings, Surface and Coatings Technology, Volume 343, 2018, Pages 101-107, ISSN 0257-8972, https://doi.org/10.1016/j.surfcoat.2017.10.062

Baca, T., Platkevic, M., Jakubek, J., Inneman, A., Stehlikova, V., Urban, M. Nentvich, O. Blazek, M. McEntaffer, R. and Daniel, V., "Miniaturized X-ray telescope for VZLUSAT-1 nanosatellite with Timepix detector", Journal of Instrumentation, 2016, vol. 11, no. 10, pages C10007, doi 10.1088/1748-0221/11/10/C10007

Martin Urban, Ondrej Nentvich, Veronika Stehlikova, Tomas Baca, Vladimir Daniel, Rene Hudec, VZLUSAT-1: Nanosatellite with miniature lobster eye X-ray telescope and qualification of the radiation shielding composite for space application, Acta Astronautica, Volume 140, 2017, Pages 96-104, ISSN 0094-5765, https://doi.org/10.1016/j.actaastro.2017.08.004

Vladimír Dániel, Adolf Inneman, I Vertat, T Baca, Ondřej Nentvich, Martin Urban, Veronika Stehlíková, Ladislav Sieger, Petr Skala, Robert Filgas, V Zadrazil, Richard Linhart, Jiří Masopust, Tomáš Jamroz, Ladislav Pína, V Marsikova, L Mikulickova, Eduard Belas, S Pospisil, Zdeněk Vykydal, Yesid Mora, Richard Pavlica, In-Orbit Commissioning of Czech Nanosatellite VZLUSAT-1 for the QB50 Mission with a Demonstrator of a Miniaturised Lobster-Eye X-Ray Telescope and Radiation Shielding Composite Materials. Space Sci Rev 215, 40 (2019). https://doi.org/10.1007/s11214-019-0589-7

L Pina, R Hudec, A Inneman, O Nentvich, M Urban, V Marsikova, V Stehlikova, D Doubravova, V Burwitz, C Pelliciari, G Hartner, V Daniel, "Multi-Foil X-ray optics tests at PANTER: Preliminary results", Contributions of the Astronomical Observatory Skalnate Pleso, 2018, volume 48, no 3, pg. 466-475, DOI: 10.1155/2010/139148

Stehlikova, V., Urban, M., Nentvich, O. and Sieger, L.. "Radiation resistance monitor on VZLUSAT-1: Preliminary results", Astron. Nachr.. 2018; 339: 382– 385. https://doi.org/10.1002/asna.201813510

Urban, M., Nentvich, O., Stehlikova, V., Sieger, L. and Mikulickova, L.. “Outgassing monitor on VZLUSAT-1: Preliminary results”, Astron. Nachr.. 2018; 339: 367– 370. https://doi.org/10.1002/asna.201813507

Nentvich, O., Urban, M., Stehlikova, V., Sieger, L. and Inneman, A.. “VZLUSAT-1: Health monitoring system, preliminary results”, Astron. Nachr.. 2018; 339: 397–402. https://doi.org/10.1002/asna.201813513

Chattopadhyay, Tanmoy and Falcone, Abraham and Burrows, David N. and Bray, Evan and McQuaide, Maria and Kern, Matthew and Wages, Mitchell and Hull, Samuel and Inneman, Adolf and Hudec, Rene and Stehlikova, Veronika, "Characterization of X-ray Lobster Optics with a Hybrid CMOS sensor", American Astronomical Society Meeting Abstracts #231, 2018,American Astronomical Society Meeting Abstracts, volume = 231, pages = 355.35, https://ui.adsabs.harvard.edu/abs/2018AAS...23135535C

O Nentvich, M Urban, V Stehlikova, L Sieger, R Hudec, "Lobster eye X-ray optics: Data processing from two 1D modules", Contributions of the Astronomical Observatory Skalnate Pleso, 2017, volume 47, no 2, pg. 178-183 M Urban, O Nentvich, V Stehlikova,

L Sieger, "Detection of X-ray spectra and images by Timepix", Contributions of the Astronomical Observatory Skalnate Pleso, 2017, volume 47, no 2, pg. 151-156

- SPIE conferences

Matthias Kroedel, Veronika Stehlíková, Stefan Menzel, "Ceramic mould development for precision bending of thin glass," Proc. SPIE 11101, Material Technologies and Applications to Optics, Structures, Components, and Sub-Systems IV, 1110105 (30 August 2019); https://doi.org/10.1117/12.2526952

Stanislav Vítek, Maria Nasyrova, Veronika Stehlíková, "Radiometric calibration of wide-field camera system with an application in astronomy," Proc. SPIE 10396, Applications of Digital Image Processing XL, 1039634 (19 September 2017); https://doi.org/10.1117/12.2274719

Thorsten Döhring, Anne-Catherine Probst, Manfred Stollenwerk, Florian Emmerich, Veronika Stehlíková, Adolf Inneman, "Prototyping iridium coated mirrors for x-ray astronomy," Proc. SPIE 10235, EUV and X-ray Optics: Synergy between Laboratory and Space V, 1023504 (31 May 2017); https://doi.org/10.1117/12.2265931

Veronika Stehlikova, Thorsten Döhring, Manfred Stollenwerk, Johannes Stadtmüller, Veronika Marsikova, Rene Hudec, Dennis Flachs, Vadim Burwitz, Gisela Hartner, Surangkhana Rukdee, Thomas Müller, Adolf Inneman, Thomas Schmidt, Mariana Klementova, Sebastian Zeising, Andreas Langmeier, "Lobster eye type X-ray telescope with chromium-iridium coated tri-layer mirrors," Proc. SPIE 11776, EUV and X-ray Optics, Sources, and Instrumentation, 1177605 (18 April 2021); https://doi.org/10.1117/12.2589266

Veronika Stehlikova, Martin Urban, Ondrej Nentvich, Adolf Inneman, Thorsten Döhring, Anne-Catherine Probst, "Study of lobster eye optics with iridium coated x-ray mirrors for a rocket experiment," Proc. SPIE 10235, EUV and X-ray Optics: Synergy between Laboratory and Space V, 1023505 (31 May 2017); https://doi.org/10.1117/12.2265769

Martin Urban, Ondrej Nentvich, Veronika Stehlikova, Ladislav Sieger, "Uncooled spectrometer for x-ray astrophysics," Proc. SPIE 10235, EUV and X-ray Optics: Synergy between Laboratory and Space V, 102350O (31 May 2017); https://doi.org/10.1117/12.2265744

Ondrej Nentvich, Veronika Stehlikova, Martin Urban, Rene Hudec, Ladislav Sieger, "Data processing from lobster eye type optics," Proc. SPIE 10235, EUV and X-ray Optics: Synergy between Laboratory and Space V, 102350N (31 May 2017); https://doi.org/10.1117/12.2265724

Thorsten Döhring, Manfred Stollenwerk, Johannes Stadtmüller, Sebastian Zeising, Dennis Flachs, Veronika Stehlikova, Vadim Burwitz, Michael Krumrey, Vincenzo Cotroneo, Mariana Klementova, "Characterisation of X-ray mirrors based on chromium-iridium tri-layer coatings," Proc. SPIE 11776, EUV and X-ray Optics, Sources, and Instrumentation, 1177607 (18 April 2021); https://doi.org/10.1117/12.2592551

Vladimir Daniel, Martin Urban, Ondrej Nentvich, Veronika Stehlikova, "VZLUSAT-1: verification of new materials and technologies for space," Proc. SPIE 9978, CubeSats and NanoSats for Remote Sensing, 99780N (19 September 2016);

https://doi.org/10.1117/12.2244035

Tanmoy Chattopadhyay, Mitchell Wages, David Burrows, Evan Bray, Adolf Inneman, Rene Hudec, Veronika Stehlikova, David Schendt, Sam Hull, Abe Falcone, Maria Mcquaide, "Characterization of x-ray lobster optics with a hybrid CMOS sensor (Conference Presentation)," Proc. SPIE 10399, Optics for EUV, X-Ray, and Gamma-Ray Astronomy VIII, 103991P (19 September 2017); https://doi.org/10.1117/12.2274647

Lenka Mikulickova, Ladislav Pina, Adolf Inneman, Daniela Doubravova, Veronika Marsikova, Ladislav Sieger, Martin Urban, Veronika Stehliková, Ondrej Nentvich, Jaromir Mirovsky, "Optimization of microroughness of replicated x-ray optics," Proc. SPIE 10235, EUV and X-ray Optics: Synergy between Laboratory and Space V, 102350A (31 May 2017); https://doi.org/10.1117/12.2265810